Universität Augsburg
Mathematisch-Naturwissenschaftliche
Fakultät

Reconstruction of Negative Hydrogen Ion Beam Properties from Beamline Diagnostics

Dissertation zur Erlangung des Doktorgrads
an der Mathematisch-Naturwissenschaftlichen Fakultät
der Universität Augsburg

vorgelegt von
Benjamin Ruf
am 04. Juni 2014

Erstgutachten: Prof. Dr.–Ing Ursel Fantz

Zweitgutachten: Prof. Dr. Wolfgang Brütting

Vorgelegt am 04. Juni 2014

Tag der Prüfung: 25. September 2014

Contents

1 Introduction

An international collaboration is currently constructing the experimental fusion reactor ITER[1] (lat. iter = way), in Cadarache, France. In this reactor deuterium and tritium will fuse to helium while generating energy. Since the two educts have to overcome the Coulomb barrier, this reaction can efficiently take place at high temperatures ($> 10^8$ K). The hot plasma is confined by a combination of toroidal and poloidal magnetic fields leading to the typical ring shape of fusion reactors. One main goal of ITER is the demonstration of a positive energy balance.

Future power plants based on a fusion reactor will have several advantages compared to current power plants:

- The fusion reaction has to be maintained and cannot become uncontrollable like it could happen in fission devices.

- The amount of fuel (this means deuterium and lithium. The latter will be converted into tritium by a breeding reaction [1]) for a fusion power plant which has an comparable electric power output to present fission plants (in the order of 1 GW) is 100 kg deuterium and 3 tons of lithium per year. The resource reservoir available on earth for the reactants is almost unlimited [2].

- The power plant material will be activated by neutrons [3]. However the radioactivity returns to a harmless dose within around 100 years or less until the material is reusable again [2, 4]. This is a small number compared to the decay time of the exhaust of fission devices ($> 10^8$ a). A final storage of the nuclear waste is unnecessary.

- Additionally, fusion reactors do not generate greenhouse gases but only small amounts of Helium, which has a neutral effect on the climate.

For the experimental reactor ITER, which should show the feasibility of sustaining

---

[1] https://www.iter.org/

a fusion plasma with a positive power balance, some technology still has to be developed, amongst others also the plasma heating system.

One heating technique is the neutral beam injection (NBI). A beam of fast deuterium atoms is injected into the fusion plasma. By heavy particle collisions the beam particles give their energy to the plasma.

A NBI system consists of three major components. First, deuterium ions are generated in a low temperature, low pressure plasma of an ion source. At ITER, the requirements on the beam energy of 1 MeV cause the necessity of negative charged deuterium ions.

Secondly, the ions are accelerated within an acceleration system with several grids, where the plasma grid is the first grid. The grids are on different descending high voltage potentials. The source itself is on the highest negative potential.

Thirdly, the fast deuterium ions have to be neutralised. The neutralisation efficiency of positive hydrogen ions at 1 MeV tends to be 0% while it still remains 60% for negative ions. Remaining ions after the neutralisation are filtered out on a beam dump by an electrostatic field. This is necessary since charged particles are not able to enter the fusion plasma, due to the deflection caused by the magnetic confinement.

The most effective way to create negative deuterium ions in a plasma is the so called surface conversion. On a surface with a low work function deuterium atoms or positive ions are converted into negative ions. This converter surface is close to the extraction area since the negative ions have a small survival length due to the low binding energy of the additional electron (0.75 eV). In order to reduce the work function on the relevant surfaces in the ion source for ITER NBI, caesium is evaporated into the vessel, covering the walls.

Due to the possible maximum current densities (in range between 300 $\mathrm{A/m^2}$ and 400 $\mathrm{A/m^2}$) the extraction area is quite large (0.2 $\mathrm{m^2}$ for ITER NBI) which leads to a large source (width × height × depth: 0.87 m × 1.77 m × 0.22 m). Thereby the plasma grid consists of several hundred small apertures (radius in the order of millimeters). The extracted ions from one aperture form a so-called beamlet. The reason for the large number of apertures is to avoid abberation effects.

This thesis deals with the second step in the mentioned beam system, the ion acceleration and beam formation. The underlying experiments and measurements were carried out at the testbeds BATMAN (**BA**varian **T**est **MA**chine for **N**egative ions) and ELISE (**E**xtraction from a **L**arge **I**on **S**ource **E**xperiment) at the Max-Planck-Institut für Plasmaphysik Garching (IPP Garching). While the ion source at BATMAN is comparatively small (1/8 ITER size; extraction area: 63 cm^2, apertures: 126, width × height × depth: 0.32 m × 0.56 m × 0.19 m) the large source at ELISE has half ITER-source size (extraction area: 1000 cm^2, apertures: 640, width × height × depth: 0.86 m × 1 m × 0.24 m). The maximum energy of the accelerated particles at BATMAN is around 25 keV, while at ELISE it can be up to 60 keV.

In order to obtain low beam power losses for ITER NBI a beam transmission as high as possible is required. This is necessary to achieve the maximum beam power (16.7 MW) and to avoid damages of beam line components by the power input from the beam losses. On the one side the negative ion destruction during the acceleration phase (so-called stripping) due to heavy particles collision of beam particles with the background gas has to be reduced.

On the other side the beam power losses by beam particle interaction with the beam line structure can be decreased by a small beamlet broadening, i.e. a small beamlet divergence, of all beamlets, which increases the beam transmission and quality. The broadening itself depends mainly on the space charge distribution at the aperture, the extraction voltage and the extracted current density. Therefore a homogenous production and generation of a sufficient amount of negative ions is necessary, i.e. a homogenous current density distribution in front of the plasma grid.

However the region of negative ion production and extraction (close to the plasma grid) cannot be diagnosed directly due to technical reasons. The plasma diagnostic tools at the IPP testbeds are measuring plasma parameters (i.e. negative ion density) at a distance of roughly 1 cm to the plasma grid. This is far away from the relevant region which is directly at the plasma grid apertures. Therefore, the only way to determine the current density distribution, i.e. the beam inhomogeneity, is to obtain a spatial divergence profile of the beam followed by a reconstruction of the density distribution from this measurement.

The main goal of this thesis is to provide a tool which allows the determination of the beam properties. These are beam divergence, stripping losses and beam inhomogeneity. For this purpose a particle trajectory code has been developed from scratch, namely BBC-NI (**B**avarian **B**eam **C**ode for **N**egative **I**ons). The code is able to simulate the whole beam and the outcome of several beam diagnostic tools. The data obtained from the code together with the measurements of the beam diagnostic tools should allow the reconstruction of the beam properties.

The major beam diagnostic tool, which is used in this thesis, is the beam emission spectroscopy (BES). BES measures the beam divergence and beam power losses from heavy particles collisions by evaluating the spectrum of the H_α light of the beam. The light is emitted since beam particles are excited by collisions with the H_2 background gas. For ITER, BES will be the main beam diagnostic tool for beam quality measurements.

This thesis will show how BES spectra in ITER relevant negative ion sources have to be evaluated and interpreted in order to determine the beam divergence and stripping losses, by simulating a BES spectrum and comparing it with measurements. A reliable BES spectrum evaluation is necessary to go one step further and to check whether a line-of-sight array allows the determination of a vertical divergence profile. With this profile the beam inhomogeneity is determined and the current density distribution of negative ions at the extraction is reconstructed. The thesis will also discuss whether, how and under which conditions this reconstruction is possible.

2 Hydrogen ion sources for neutral beam injection

Experimental fusion reactors, which are operated to develop a fusion power plant, are working with hot deuterium-tritium plasmas, reaching temperatures in the range of up to 10 keV ($\approx 10^8$ K) [5]. The confinement of such plasmas is possible with a toroidal magnetic field generated by several coils. Because of the bending of the magnetic field lines, radially magnetic field gradients appear. They lead to a radially outwards directed drift, which reduces the confinement time drastically. In order to compensate this effect, an additional poloidal magnetic field is applied which twists the toroidal magnetic field lines and prevents the outwards drift. The additional field can be generated by two ways. With the “Stellarator” configuration, the poloidal magnetic field is generated by the external coils, leading to an complex shape of the single coils. In the “Tokamak” configuration the poloidal field is generated by inducing a toroidal plasma current by ramping a current in a center solenoid. This solenoid acts as a first winding in a transformer, with the fusion plasma as the second winding.

To achieve the plasma temperatures needed for fusion, several various heating systems can come into operation. Beside ohmic heating and electromagnetic wave heating (ECRH, ICRF[2]), neutral beam injection (NBI), which is a reliable system, is used in many current devices [5]. The following chapter will describe the NBI system in detail and the ongoing development issues which are tackled at the moment.

2.1 NBI system

Figure 2.1 shows the schematic view of a NBI system. It can be divided into three basic sections:

---

[2] **E**lectron **C**yclotron **R**esonance **H**eating/**I**on **C**yclotron **F**requency **R**ange: Irradiation of electromagnetic waves with the gyration frequency of the electrons/ions in the fusion plasma.

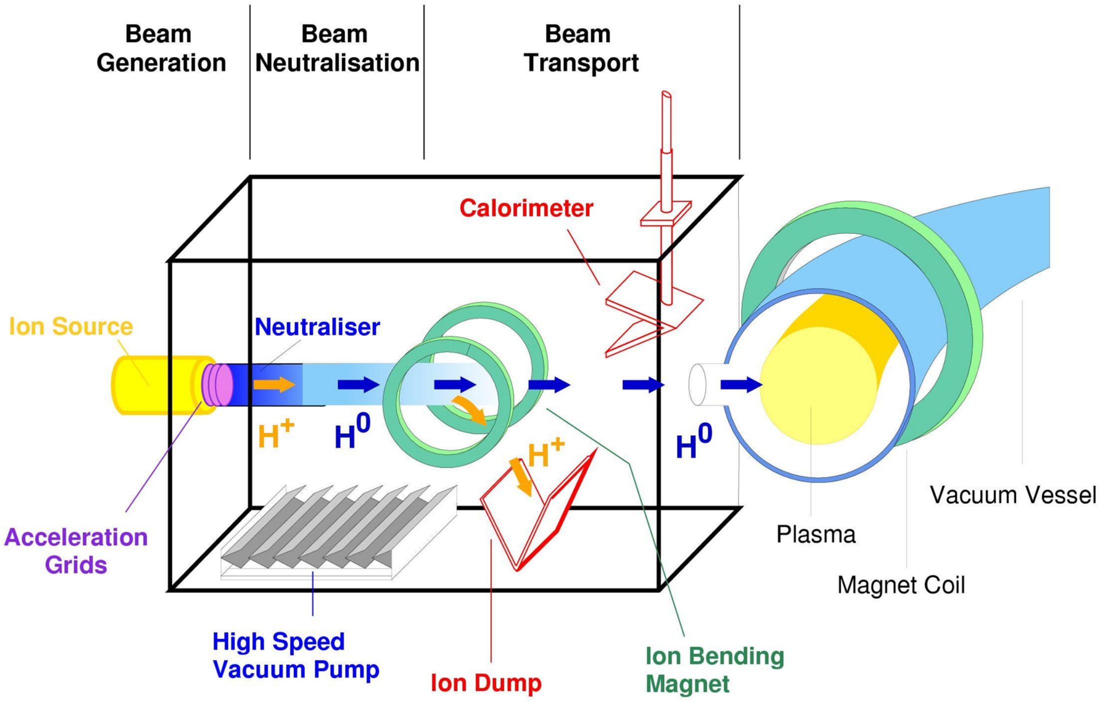

Figure 2.1: *Scheme of an NBI system with the major components*[3].

1. Generation of an ion beam.
2. Neutralisation of the beam.
3. Transport of the neutral beam particles to the fusion plasma.

NBI systems usually work in hydrogen or deuterium, since these are the preferred kinds of gases used in fusion devices [6]. In the following the physical correlations and results are referred to hydrogen and deuterium, while only hydrogen will be mentioned in the text. However, if there is an isotope effect it will be mentioned explicitly.

Ion beam generation: The beam power typically requested is in the range of some megawatt. This means that an ion beam current of several tens of amperes, an ion acceleration with high voltage in the range of tens of kilovolt and a large beam diameter are required. These requirements lead to the necessity of large sources (0.1–1 m^2) for the ion generation compared to present NBI sources at fusion devices. For this reason two concepts for the plasma generation are common [7, 8]:

---

[3] Image is property of the Max-Planck-Institut für Plasmaphysik Garching

Arc sources: in arc sources, electrons are emitted from hot cathodes (2000–3000 K) which are usually tungsten filaments. Because of the high temperature, the filaments erode very quickly and have to be substituted regularly (for ITER NBI every six months [9]). The electrons are accelerated (typically around 100 V) into the source volume where they ionise a filling gas and create a plasma [10]. The arc current is up to several thousand amperes.

RF sources: In RF sources an oscillating electric field is induced via a RF coil. The field accelerates free electrons in the vessel volume. These electrons then create a plasma. The field frequency is typically around 1 MHz while the induced power is in the order up to 100 kW [8]. RF sources are basically maintenance-free, which is a major advantage compared to arc sources. Therefore ITER will have RF sources (see chapter 2.4.1)

In the ion source, hydrogen ions are generated. They are subsequently extracted and accelerated by means of a multiple aperture grid system consisting of several hundred apertures. The typical aperture radius is in the order of several millimeters. This means the beam consists of up to several hundred small ion beams called beamlets. The division into many beamlets is done in order to minimise aberration effects in the ion optics. They can occur with large beamlet diameters. In contrast to accelerator sources (with one beamlet only) the beam optics have to be done from the start of the extraction by the geometry of the grid system. This because of the large beam size, which leads to deflections of externally applied magnetic and electric fields.

Neutralisation: Since the plasma of fusion device is confined by a strong toroidal and poloidal magnetic field, charged particles streaming towards the fusion plasma are diverted and cannot reach the plasma. The diverted beam particles can lead to damages of surrounding components. Therefore, the fast ion beam has to be neutralised, which is done by collisions with a gas target. The beam passes through a large gas cell (in the range of several cubic meter). The neutralisation efficiency depends on the ion beam energy and is an important factor for the choice of the polarity of the ions (see chapter 2.2). The gas pressure inside the neutraliser ($> 0.1\,\mathrm{Pa}$) is higher than in the vessel of the fusion plasma, to which the NBI system is connected. In order to minimise the gas filling in the duct to the fusion vessel and subsequently reduce the re-ionisation of the fast neutral particles, large vacuum pumps (Ti-getter pumps or cryopumps (pumping speed > $100\,\text{m}^3/\text{s}$)) come into operation in this part of the NBI.

Transport: Downstream the neutraliser the remaining ions are filtered out of the beam by strong deflection magnets or, at ITER, with an electrostatic field. The ions are guided on a cooled ion dump. The high energetic neutral beam is led through the beam duct into the fusion reactor. The neutral beam particles can then transfer their energy to the fusion plasma by collisions.

Due to the neutraliser, the large vacuum pumps and the system to filter out the remaining ions after the neutralisation, a NBI device is very large. For ITER the length of the NBI system will be 15 m between the ion source and the duct into the reactor vessel [11]. The width will be 4.7 m and the height will be 5.3 m [11].

2.2 ITER requirements for NBI

After introducing the basic principle of NBI systems, this chapter will now focus on crucial parameters of such a system. An important parameter is the neutralisation efficiency for the fast ions passing a gas target. The neutralisation efficiency, which is linked to the cross sections of the collisions between beam particles and background gas, is dependent on the ion energy and on the ion polarity. Figure 2.2 shows the neutralisation efficiency dependence on the ion energy of positive and negative hydrogen and deuterium ions. For positive ions with energies above 200 keV, the neutralisation efficiency is below 20%. However, for negative ions this value stays above 60% even for energies in the range of MeV. This is due to the low binding energy (0.75 eV [12]) of the additional electron of the negative hydrogen ion.

The choice of the ion energy is an important parameter for plasma heating and current drive:

Plasma heating: The heating efficiency depends on the penetration depth of the accelerated neutral particles. These fast particles enter the fusion plasma and are ionised either by collisional ionisation by electrons, collisional ionisation or charge exchange by plasma ions. The penetration depth correlates with the mean free path of the fast neutral particles. This means the fusion plasma density and the cross sections of the ionisation and charge

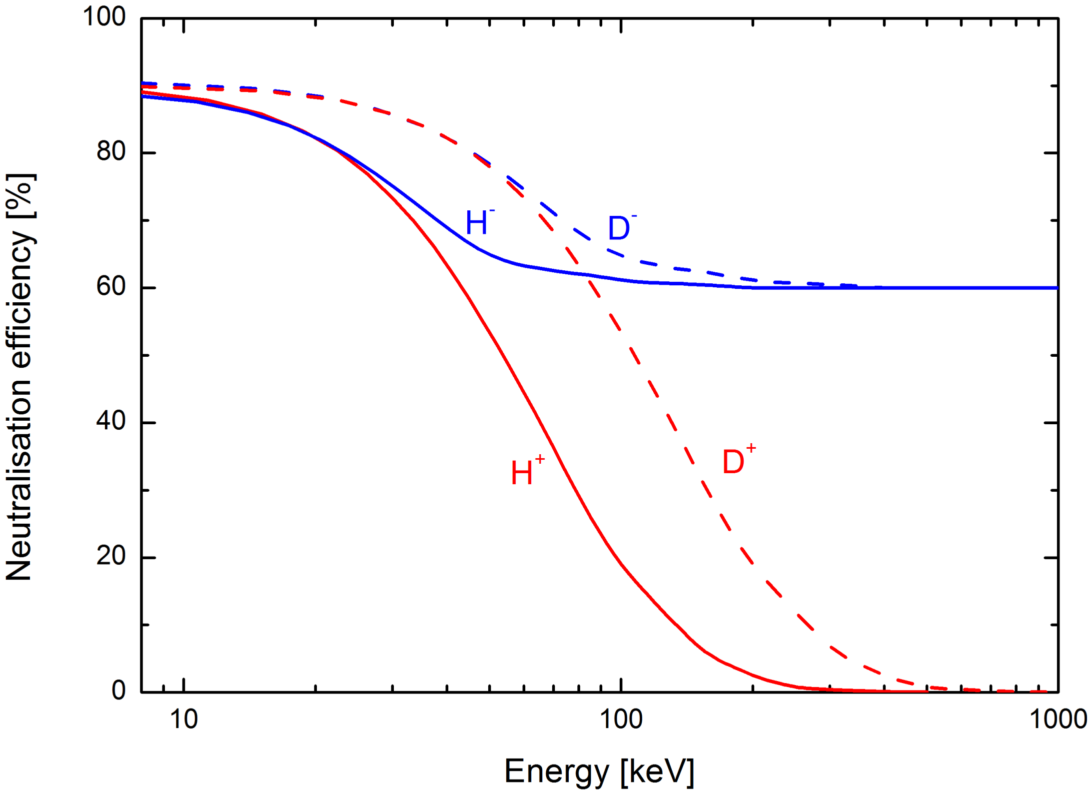

Figure 2.2: *Neutralisation efficiency for positive and negative hydrogen/deuterium ions [13].*

exchange reactions are crucial parameters [15]. For medium size fusion reactor devices like ASDEX[4] Upgrade (minor radius ≈ 0.5 m) [16] energies up to 100 keV are still sufficient. However ITER with a four times larger minor radius [17] and a similar radial temperature and density profile will need neutral particles with higher energies (see chapter 2.3) in order to have an acceptable heating efficiency with NBI.

Current drive: ITER will perform long pulses of up to one hour. In order to keep the magnetic confinement in this Tokamak it is necessary to drive a toroidal plasma current. However, by inducing the current, this method has a time limitation which is the ramp up time of the central solenoid. ITER will have a induced plasma current of 15 MA for up to 400 s [17]. Heating systems like ECRH and NBI can be used for additional current drive, extending the pulse length up to one hour. This will be tested at ITER. The current drive efficiency η_{CD} of the NBI system mainly depends on the energy of the

---

[4] **A**xial**S**ymmetrisches **D**ivertor **EX**periment

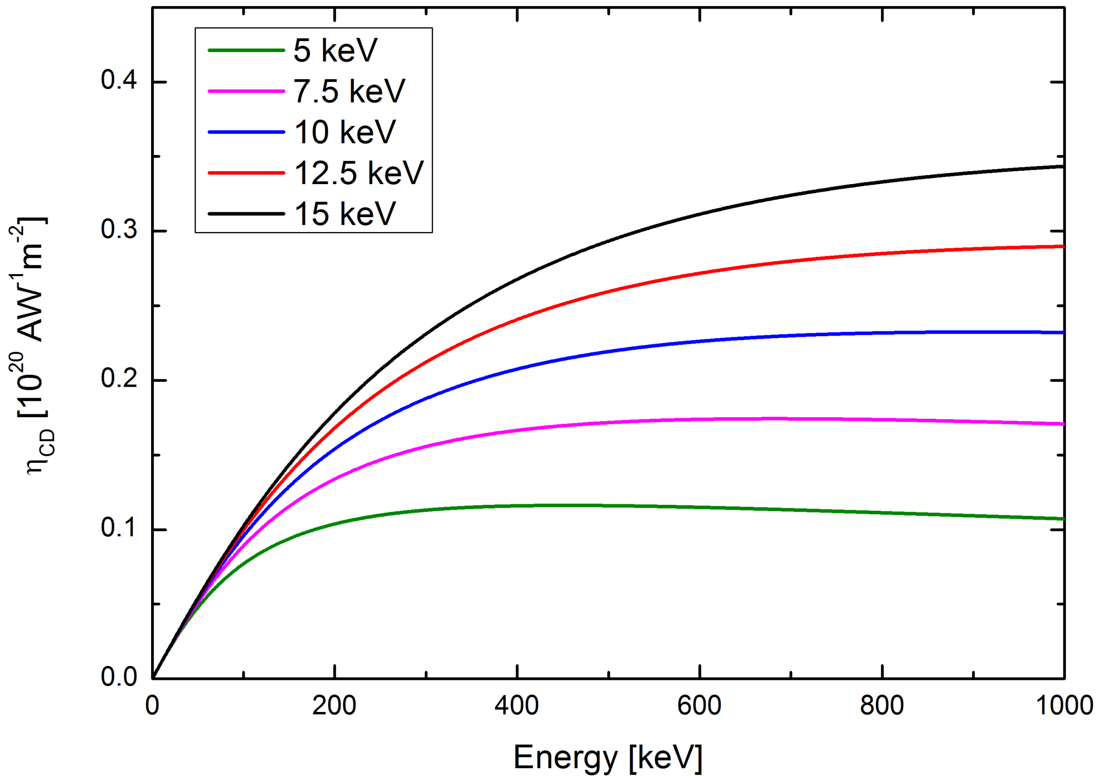

Figure 2.3: *Current drive efficiency for various electron temperatures in the core of the fusion plasma [14].*

fast neutral particles. Figure 2.3 shows this dependency for various electron core temperatures of the fusion plasma. For a electron temperature of 5 keV, which is a representative value for ASDEX Upgrade [18], a relatively high current drive efficiency can already be achieved between 100–200 keV. The two installed NBI systems can inject fast deuterium particles with an energy up to 93 keV and hydrogen particles with 72 keV [19].

ITER envisages an electron temperature of 15 keV and needs a higher current drive efficiency from the NBI system than in recent fusion devices. This can be only achieved with energies above 850 keV [20].

Up to now, most fusion devices have been operating with NBI systems based on positive ions. This is due to the size and the plasma parameters which were accomplished in these fusion machines. For ITER, with larger size and higher core temperatures, NBI systems with energies of several 100 keV, based on negative ions, have to be used. ITER will have two NBI systems for heating and current drive each providing a heating power of 16.7 MW. Because of the presently achieved current density in negative ion sources (see chapter 2.3), the acceleration

Table 2.1: *ITER requirements on the heating and current drive beams [11, 23].*

Parameter	**Isotope**	
	Hydrogen	**Deuterium**
Power	16.7 MW	16.7 MW
Source pressure	≤ 0.3 Pa	≤ 0.3 Pa
Extraction area	0.2 m^2	0.2 m^2
Extracted current	≥ 66 A	≥ 56 A
Extracted current density	≥ 330 A/m^2	≥ 280 A/m^2
Accelerated current	≥ 46 A	≥ 40 A
Ratio of co-extracted electrons to ions	< 1	< 1
Acceleration voltage	0.87 MV	1 MV
Pulse length	400 s	3600 s
Beam core divergence	$\leq 0.4°$	$\leq 0.4°$
Beam inhomogeneity	$< 10\%$	$< 10\%$

voltage has to be 1 MV for deuterium.

2.3 ITER source

Several requirements have to be fulfilled by the ITER NBI negative hydrogen ion source. Table 2.1 lists the specifications of the main parameters. The heating power of one beam line has to be 16.7 MW. The extracted current density for deuterium and hydrogen is in the parameter range close to the achievements with the so-called KAMABOKO source (300 A/m^2 with H^- and 200 A/m^2 with D^-) (see also section 2.4.1) [21]. This consequently determines the extraction area and the beam energy.

The pressure in the acceleration part has to be as low as possible in order to minimise the destruction of negative ions by collisions with the background gas before they are fully accelerated (stripping). However, the pressure in the source has to be high enough to generate a sufficient amount of negative ions. Therefore the source will be operated at a pressure of 0.3 Pa which is a compromise between the two requirements. The predicted relative electron detachment (stripping) from negative ions by heavy particle collisions is still high and at around 30% [22].

Because of the applied positive extraction voltage, also electrons are extracted from an ion source for negative ions. These co-extracted electrons have to be filtered out of the beam right after the extraction in order to prevent damages of beamline components by high energetic co-extracted electrons. They are guided onto dedicated surfaces, which leads still to a power density input that can be around 40 MW/m^2 [24] on local spots. The cooling capabilities of these surfaces are a technological challenge and limit the maximum acceptable power input. The ratio between co-extracted electrons and extracted negative ions has to be kept below 1 in order to minimise the power input of the co-extracted electrons as far as possible. As already shown in chapter 2.2, the ion plasma heating and current drive efficiency are dependent on the ion energy. Due to the required heating power, the ITER size and the experimental scenarios, the acceleration voltage for the ions has to be 0.87 MV for hydrogen and 1 MV for deuterium, as already mentioned.

ITER needs a NBI system which is able to operate up to one hour [11] in order to provide a current drive.

The beam core divergence, i.e. the broadening of the beam, has to be $\leq 0.4°$, which means beam particles in this divergence range will carry 85% of the beam power. The rest can have a higher divergence around 0.9° - 1.7° [11].

Finally, the beam inhomogeneity is a crucial parameter since it is directly connected to power losses during the beam transmission to the fusion plasma. The spatial beam inhomogeneity has to be less than 10%. The beam physics and the definition of the beam inhomogeneity can be found in chapter 2.5. The determination of the beam inhomogeneity in large sources will be one topic of this thesis.

Due to radioactive contamination, the maintenance of the NBI system at ITER has to be done remotely. Therefore the requirement on the NBI components is a widely maintenance free operation in order to keep the remote handling as simple as possible.

2.4 Negative hydrogen ion sources

This chapter will first introduce negative ion sources that are in operation at present. A comparison with the ITER requirements from the last chapter will show the need of the development of a new source, which will be presented in chapter 2.4.3 and 2.4.4.

Table 2.2: *Parameters achieved with present arc-driven negative ion sources [30, 31]. In the case of JT-60U the source performance parameters for two different beam pulse lengths are shown.*

	JT-60U (one source)		**LHD (one source)**
Parameter	**Deuterium**		**Hydrogen**
Power	2.9 MW	$\leq$ 2 MW	7 MW
Source pressure	$<$ 0.27 Pa	$<$ 0.27 Pa	$<$ 0.33Pa
Extraction area	$\leq 0.166\,\mathrm{m}^2$	$\leq 0.166\,\mathrm{m}^2$	$0.115\,\mathrm{m}^2$
Extracted current	17.4 A	10 A	37 A
Extracted current density	$130\,\mathrm{A/m}^2$	$100\,\mathrm{A/m}^2$	$340\,\mathrm{A/m}^2$
Acceleration voltage	400 kV	345 kV	190 kV
Pulse length	0.73 s	25 s	1.6 s

2.4.1 State of the art

Negative hydrogen ion sources have been developed for the fusion experiments JT60-U and LHD in Japan and started to operate in the mid 1990s [7]. The basic principle of plasma generation is an arc discharge (see section 2.1) utilising the so-called KAMABOKO source [25, 26]. Table 2.2 shows the achieved parameters of these ion sources. In the case of JT-60U the source performance parameters for two different beam pulse lengths are shown.

Relating to the extracted current, present day NBI devices working with negative ions are able to deliver the required ITER parameters. Increasing the acceleration voltage to 1 MV is a technical problem [27], which is already tackled [28, 29]. Also the pulse length can be increased with a suited pumping system, power supply and cooling system.

Problematic for ITER is the fact that the tungsten filaments in arc sources have to be replaced regularly, which means the source requires intensive maintenance at least every six months [9]. That is the reason why for the ITER NBI systems arc sources are not preferred. Since 2007 the IPP RF source is the reference source for the ITER NBI system [32], because with this maintenance free source type, similar performance values compared to arc sources have been achieved.

The experimental research and development programm in Europe for the ITER NBI source is carried out at several research facilities. The development of the prototype RF source has been done and is still in progress at IPP Garching. Special physical issues are tackled at small experiments at University of Augsburg, supporting the source development at IPP [33]. At Consorzio RFX in Padua, Italy, the full size ITER source will be set up at the testbed SPIDER (**S**ource for the **P**roduction of **I**ons of **D**euterium **E**xtracted from an **R**F plasma), while at the testbed MITICA (**M**egavolt **IT**ER **I**njector and **C**oncept **A**dvancement) the full beam line will be installed [34].

2.4.2 Negative hydrogen ion production and destruction

The generation of negative hydrogen ions in the plasma in RF ion sources for ITER NBI can be achieved by two processes:

Volume production: The production of negative ions in the plasma volume consists of two reactions:

$$\mathrm{H}_2 + \mathrm{e}^- \quad \rightarrow \quad \mathrm{H}_2(\nu) + \mathrm{e}^- \,, \tag{2.1}$$

$$\mathrm{H}_2(\nu) + \mathrm{e}^- \quad \rightarrow \quad \mathrm{H} + \mathrm{H}^- \,. \tag{2.2}$$

ν specifies the vibrational excitation level of a molecule. In a first reaction in the plasma, hydrogen molecules in the electronic ground state are excited to higher vibrational states by electron collisions (equation (2.1)). Secondly, an electron can be attached to this vibrational excited molecule, leading to the formation of H_2^- and then to its dissociation (equation (2.2)). This reaction has its highest cross section for vibrational levels $\nu \geq 5$ in hydrogen and $\nu \geq 8$ in deuterium [35]. In order to get this high vibrational excited molecules, hot electrons ($T_\mathrm{e} \approx 5\,\mathrm{eV}$) are necessary for reaction (2.1). On the other side a high rate coefficient for the dissociations process is at $T_\mathrm{e} \approx 1\,\mathrm{eV}$ [36].

Surface production: Negative ions are created by an electron tunneling transfer from a surface to hydrogen atoms or positive hydrogen ions coming from the plasma:

$$\mathrm{H}, \mathrm{H}^+ + \mathrm{e}^-_{\mathrm{surface}} \rightarrow \mathrm{H}^- \,. \tag{2.3}$$

The effectiveness increases by decreasing the work function of the surface. This can be achieved by caesium coverage of the respective surface. The dominant production channel in negative ions sources for the ITER NBI is the conversion of negative hydrogen ions from the neutral atoms [37].

The destruction of negative ions has three main processes:

- **Mutual neutralisation:** Negative ions can be neutralised by a charge exchange reaction with positive hydrogen ions [38, 39] from the plasma.:

$$H^- + H_x^+ \rightarrow H_x + H\,, \tag{2.4}$$

- **Electron detachment by electron collisions:** Collisions of negative ions with electrons from the plasma can lead to electron detachment:

$$H^- + e^- \rightarrow H + 2e^-\,. \tag{2.5}$$

  The effectiveness of the reaction strongly increases with electron temperature [40].

- **Electron detachment by heavy neutral particle reactions:** This detachment can happen by three reactions which are associative detachment (reaction (2.6)) and non-associative detachment by heavy particle collisions (reactions (2.7) and (2.8)):

$$\begin{aligned} H^- + H &\rightarrow H_2 + e^-\,, & (2.6)\\ H^- + H &\rightarrow 2H + e^-\,, & (2.7)\\ H^- + H_2 &\rightarrow H + H_2 + e^-\,. & (2.8)\end{aligned}$$

  The probability of these reactions depends on the temperature of the ions and neutrals as well as on the heavy particle density.

Figure 2.4 shows the rate coefficients for reactions (2.4) - (2.8). Although the coefficients for the heavy particle reactions are in general one order of magnitude below the other processes, they cannot be neglected in hydrogen plasma sources for NBI. This is caused by a high neutral hydrogen molecule density (around $3 \cdot 10^{19}\,\mathrm{m}^{-3}$) due to the low dissociation degree of about 10% [43] while the electron and ion densities in the negative ion production region are at around $10^{17}\,\mathrm{m}^{-3}$ [44].

The rate coefficient for heavy particle collisions are more or less constant. Therefore the only way to minimise the destruction of negative ions in the source is to decrease the electron temperature to about or below 1 eV. The technical solution used for obtaining such electron temperatures will be presented in the next chapter.

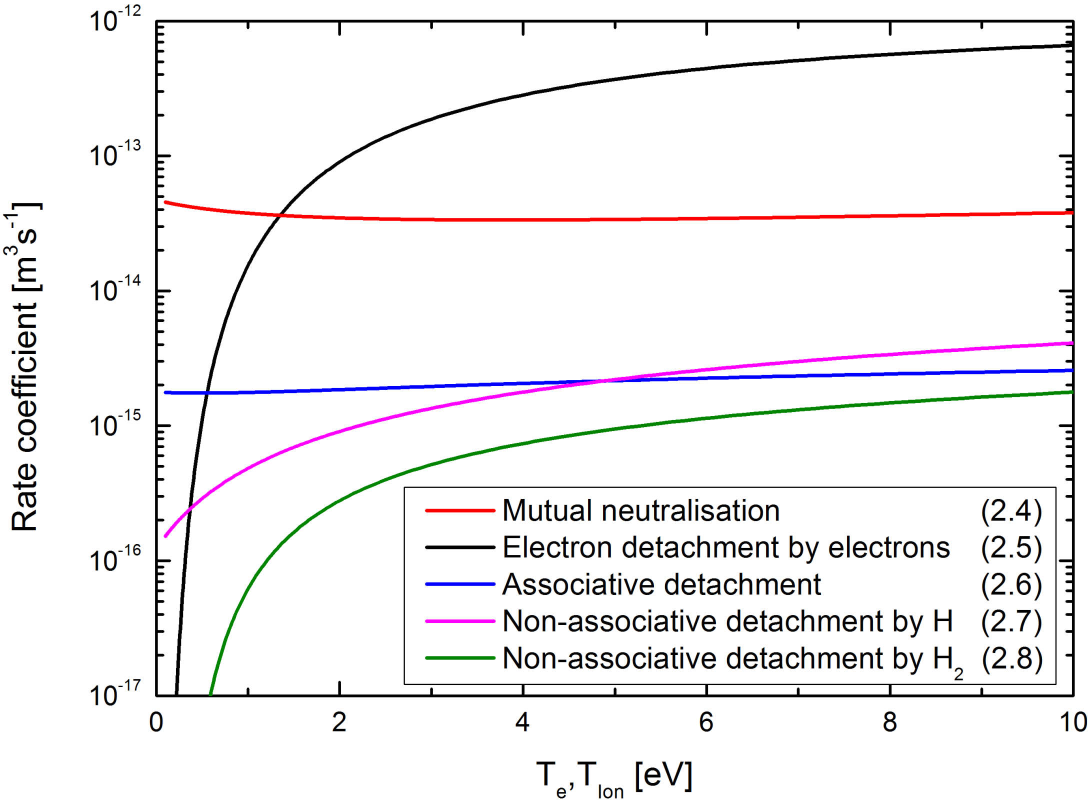

Figure 2.4: *Rate coefficients for negative ion destruction reactions [41, 42].*

2.4.3 IPP prototype source for ITER

Figure 2.5 shows a CAD model of the IPP prototype source. The size of the rectangular chamber is 0.56 m in height, 0.32 m in width and 0.19 m in depth. It had been operated at two testbeds and is still in operation at one testbed:

BATMAN: The **BA**varian **T**est **MA**chine for **N**egative ions is operating with short pulses because of the limitation of the pumping system and power supply. The duty cycle is typically 180 seconds in vacuum phase and 10 seconds in plasma phase (with 5 seconds of beam). The goal of the experiments is to optimise the source performance, i.e. the current densities at ITER relevant pressure and low ratio of co-electron to ions, in short pulses [23]. The extraction area ($< 0.01\,\mathrm{m}^2$) is determined by the pumping speed of the pumping system. Furthermore, the testbed is used for the development of new diagnostic tools and thus to get a better understanding of the physical behaviour of the plasma.

MANITU: The **M**ulti **A**perture **N**egative **I**on **T**est **U**nit had the capability for

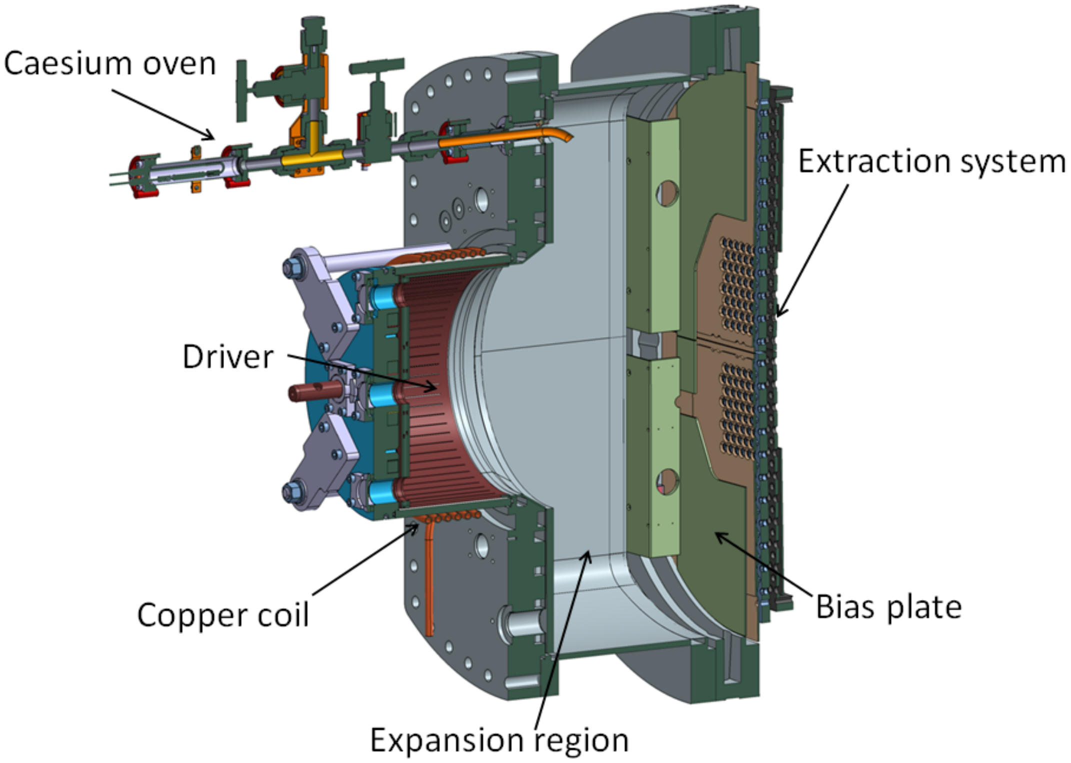

Figure 2.5: *CAD model of the IPP protoype source*[5]*. Its dimensions are 0.56 m in height, 0.32 m in width and 0.19 m in depth. The plasma is generated in the driver and expands to the extraction system.*

> pulses up to one hour due to its cw RF power supply, pumping system [45, 46] and cooling. The extraction system is equal to the one at BATMAN. Stable long ITER relevant pluses were demonstrated at a reduced extracted negative ion current with an enlarged (compared to BATMAN) extraction area of $0.02\,\mathrm{m}^2$ [47].

The source is operated in hydrogen and deuterium. However, the amount of co-extracted electrons in deuterium is higher than in hydrogen [48]. At the testbed BATMAN the ion currents required for ITER were achieved for both hydrogen isotopes at the relevant pressure and with the demanded ratio for the electron content [23]. At MANITU the long pulse operation was successfully shown. In hydrogen current densities of 200–250 $\mathrm{A/m^2}$ have been achieved for pulses of several hundred seconds [49]. In deuterium finally a one-hour pulse was performed, but not at a relevant extraction current density ($j_{\mathrm{D}^-} = 100\,\mathrm{A/m^2}$ and $j_{\mathrm{e}^-}/j_{\mathrm{D}^-} \approx 1$) [49].

---

[5] Image is property of the Max-Planck-Institut für Plasmaphysik Garching

The plasma in the IPP prototype RF source is generated in the so-called driver by inductive coupling of a RF field with a frequency of 1 MHz [8]. The field is generated by a water cooled copper coil with four to six windings bend around a ceramic (Al_2O_3) cylinder. For the protection of the ceramic cylinder from the plasma, a cylindrical Faraday screen is mounted inside the driver. The screen has slits in order to allow the RF field to penetrate into the driver. The power is between 20 and 90 kW depending on the operation scenario. The typical plasma parameters in the driver are $T_\mathrm{e} \approx 10\,\mathrm{eV}$ and $n_\mathrm{e} \approx 1 \cdot 10^{18}\mathrm{m}^{-3}$ [43].

After its generation, the plasma expands into the expansion volume of the source. This leads to a first cooling effect on the electron temperature. It is reduced to $T_\mathrm{e} \approx 1\,\mathrm{eV}$ at the extraction in order to minimise the negative ion destruction (see chapter 2.4.2). The expansion volume ends at the plasma grid, which is the first grid of the three grids multi-aperture extraction system. Here, negative ions from the source are extracted and formed to an ion beam. This part of the source will be explained in more detail in chapter 2.5.

The plasma grid is biased positively with respect to the source walls which increases the electron flux onto the plasma grid. By using this "bias effect" the current density of co-extracted electrons can be decreased [48], since the electron density in front of the plasma grid might be reduced [50]. The effect of decreasing the co-extracted electron current can be increased further by adding a so-called bias plate in front of the plasma grid which has the same potential as the source body [50]. The plate, as it can be seen in figure 2.5, excludes only the apertures of the plasma grid, increasing the non-biased source surface. The bias voltage also slightly affects the negative ions, leading to a lower extracted current, but not to the same extent as for the electrons [51]. In source operation, the adjusted value for the bias voltage is a trade-off between the co-extracted electron current, which should be as low as possible, and the extracted negative ion current remaining at an acceptable high value.

Hydrogen ion sources for NBI, operating in volume production at low pressure ($< 1\,\mathrm{Pa}$), have shown a ten times smaller extracted ion current density compared to sources with negative ion production by the surface effect [23]. Additionally the co-extracted electron current density in volume production sources is ten times higher [23]. Co-extracted electrons in negative hydrogen ion sources are guided onto an electron dump. High co-extracted electron currents on their part lead to a high power density input on the electron dump, which has to be diverted.

Therefore the generation of the negative ions is done mainly by the surface effect (see equation (2.4.2)) due to the achievable high current density. For that reason the work function of the plasma grid surface, where the negative ions are generated and also extracted, has to be decreased. For this purpose, caesium, which is a low work function material, is evaporated into the source via a caesium oven. The oven in the prototype source is installed at the top of the source backplate with a nozzle extended into the source vessel. Caesium is introduced into the source and distributed during the vacuum phases and the plasma pulses. The caesium in the source can build up reservoirs on the walls.

In vacuum phases (i.e. between plasma pulses) the sticking of the caesium to the side wall is the dominant parameter for re-distribution of caesium coming from the walls. In order to minimise accumulation at the source surfaces, the temperature of the walls is kept at typically 35° C [52] while the melting point of caesium is at 28° C. The plasma grid is heated up to temperatures above 120° C which reduces the sticking to the plasma grid surface and enhances the desorption of caesium [53]. Experiments showed that plasma grid temperatures above 120° C also lead to an increase of the extracted negative ion current compared to lower temperatures [23].

During plasma pulses, the caesium is re-distributed by the influence of the plasma which heats up the source walls. In this phase different caesium reservoirs might be present than in the vacuum phase. Furthermore the caesium in the plasma is mainly ionised. Therefore the transport is different from the one in the vacuum phase as the caesium ions are affected by the electric fields of the plasma [54].

In summary, this means that the caesium fluxes in the source, or in other words the caesium dynamics are very complex and rely on the caesium amount, the surface temperatures in the source and the caesium sticking to the walls. Additionally the temporal buildup and depletion of caesium reservoirs increases the complexity, especially in a source designed for long pulses (up to one hour) [55].

Part of the caesium, distributed in the source, covers the plasma grid and reduces the work function. Pure caesium has a work function of 2.14 eV [56], while for the formation of a dipole layer on a metal surface in high vacuum conditions ($p < 10^{-6}\,\mathrm{Pa}$) the work function can reach a value of 1.4–1.7 eV [57, 58] for sub-monolayers of caesium. In the IPP RF source the minimum work function which can be accomplished is around $2.2 \pm 0.3\,\mathrm{eV}$ [58]. This is because of the gas filling pressure of 0.3 Pa, a caesium bulk layer on the plasma grid and a background gas pressure between pulses of 10^{-4}–10^{-3} Pa. The relatively high density of the background gas during vacuum pulses leads to impurities of the caesium layer on the plasma grid. This may come from caesium chemistry with oxygen or oxygen compounds which are very reactive with caesium [54]. But also copper can be embedded into the caesium layer. Since many source components are out of copper due to its very good heat conductivity, copper sputtering by hydrogen and self-sputtering has to be avoided. Therefore the plasma grid is coated with molybdenum because of the low yield for sputtering by hydrogen and self-sputtering. In order to minimise the work function, a constant caesium flux on the plasma grid and frequent plasma pulses are necessary which have a regeneration and cleaning effect.

The extracted negative ion current depends on the work function of the plasma grid surface. The work function is related to the caesium amount in the source, the caesium flux to the plasma grid and the quality of the caesium layer [54, 59, 60]. A inhomogeneous work function on the plasma grid surface may lead to a spatially non-uniform production of negative ions. This would lead to a spatially inhomogeneous beam. Determining the beam inhomogeneity can give the possibility to reconstruct the distribution of negative ions in front of the plasma grid and therefore also the spatial production distribution.

As already mentioned in 2.4.2, the electron temperature in front of the plasma grid has to be kept around 1 eV. Therefore a horizontal magnetic filter field generated by permanent magnets with a strength of several mT is set up in the expansion region. In the prototype source hot electrons coming from the driver are magnetised and gyrate around the field lines with the Lamor radius $r_{\mathrm{g,e}}$ defined by

$$r_{\mathrm{g,e}} = \frac{m_{\mathrm{e}} v_{\perp}}{\mid e \mid B} . \tag{2.9}$$

$v_{\perp}$ is the electron velocity perpendicular to the magnetic field B, m_{e} is the electron mass, e the elementary charge. The field strength is so, that the ions are not magnetised.

The electrons can pass the magnetic filter field in axial direction by Coulomb collisions. The cross section σ for this process correlates with the electron velocity v by $\sigma \propto v^{-3}$ [61]. This means that cold electrons pass the filter field much more efficiently leading to a lower electron temperature of the plasma in front of the plasma grid. Additionally, the electrons are cooled down due to an energy transfer by inelastic collisions with hydrogen atoms or molecules.

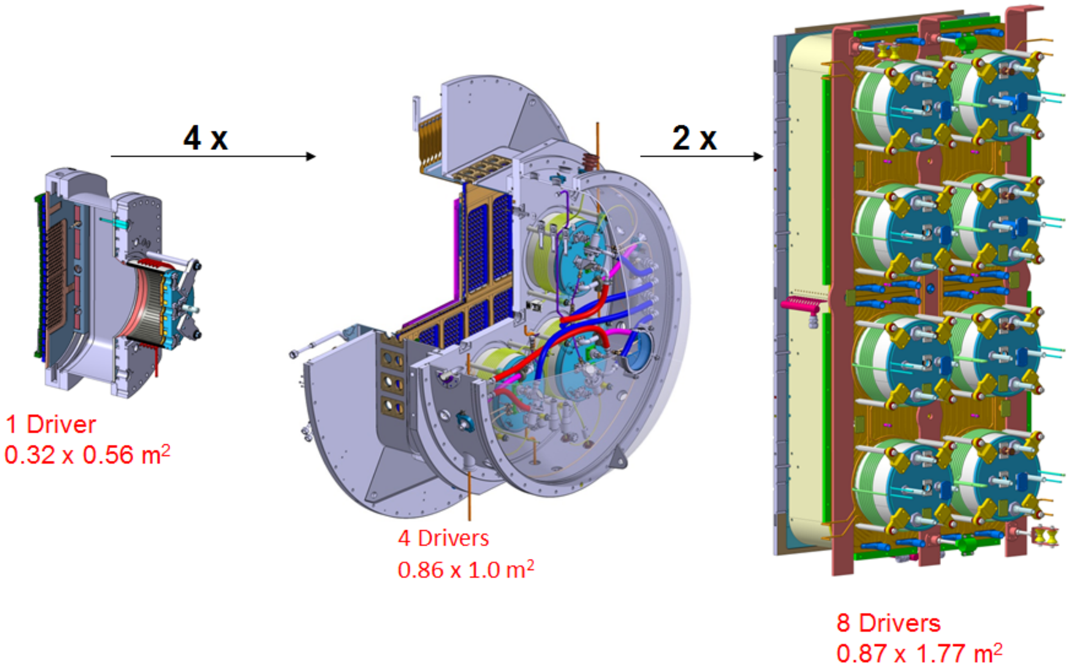

Figure 2.6: *Source development: on the left side the IPP prototype source. On the right side the source which is envisaged for ITER NBI. In the middle as intermediate step the half ITER size source at the testbed ELISE developed at IPP Garching*[6]*.*

However, the filter field has an effect on the plasma homogeneity. A vertical plasma drift has been observed and the plasma can become vertically inhomogeneous [62]. A probable explanation is a $E \times B$-drift which could come from the magnetic filter field and the electrical fields being present in the plasma coming from the variation of the plasma potential along the axial axis [63].

2.4.4 Size scaling

As already mentioned in the previous chapter, with the IPP prototype source the ITER requirements regarding the extracted current densities were already achieved. However, the size of the source at IPP is roughly 1/8 of the planned ITER source. Therefore an intermediate step in the source development is done. In figure 2.6 this development is shown. On the left side is a CAD model of the prototype source with one driver, while on the very right side is a sketch of the ITER source having eight drivers which is build at Consorzio RFX [34]. As

---

[6] Image is property of the Max-Planck-Institut für Plasmaphysik Garching

Table 2.3: *Source parameters at the testbed ELISE [67].*

Parameter	**Value**
Isotope	Hydrogen, Deuterium
Extraction area	$0.1\,\mathrm{m}^2$
Apertures	640
Source size	$1.0\,\mathrm{m} \times 0.86\,\mathrm{m}$
Total voltage	$< 60\,\mathrm{kV}$
Extraction voltage	$< 12\,\mathrm{kV}$
Pulse Length	3600 s plasma, 10 s beam extraction every 160 s

an intermediate step, in order to perform experiments of extrapolation in size scalability, the ion source at the ELISE (**E**xtraction from a **L**arge **I**on **S**ource **E**xperiment) testbed with four drivers was built at IPP [64]. The goal is to show stable operation at ITER relevant parameters having half the size of the ITER NBI source. One main focus is thereby the beam and plasma homogeneity, since there exists no experience with such a large source for NBI applications. The way to determine the beam inhomogeneity at this large source is part of this thesis and will be discussed in chapter 5.2

Table 2.3 shows the ion source parameters at ELISE. A photo of the test facility can be seen in figure 2.7. Due to the size of the source, a magnetic filter field in front of the plasma grid cannot be provided by permanent magnets anymore as the field in the center would be rather small. Therefore, the filter field in the large ELISE source and in the even larger ITER NBI source is generated by a current (up to 5.3 kA at ELISE) through the plasma grid [65, 66], the so-called plasma grid current I_{PG}. Due to the different generation, the 3D topology of the magnetic field in the source of ELISE is different from the one at BATMAN. It is also an experimental goal to study the effect of the different 3D structure of the magnetic field on the source performance and the beam inhomogeneity.

2.5 Extraction system

The extraction system of the negative ion source test facilities at IPP consists of three grids. The beam formation divides up into the extraction phase in the first gap and into the acceleration phase which takes place in the second gap. However, the acceleration phase can also be divided in several high voltage steps, which is not the case at the ion sources at IPP. In contrast to positive ion sources,

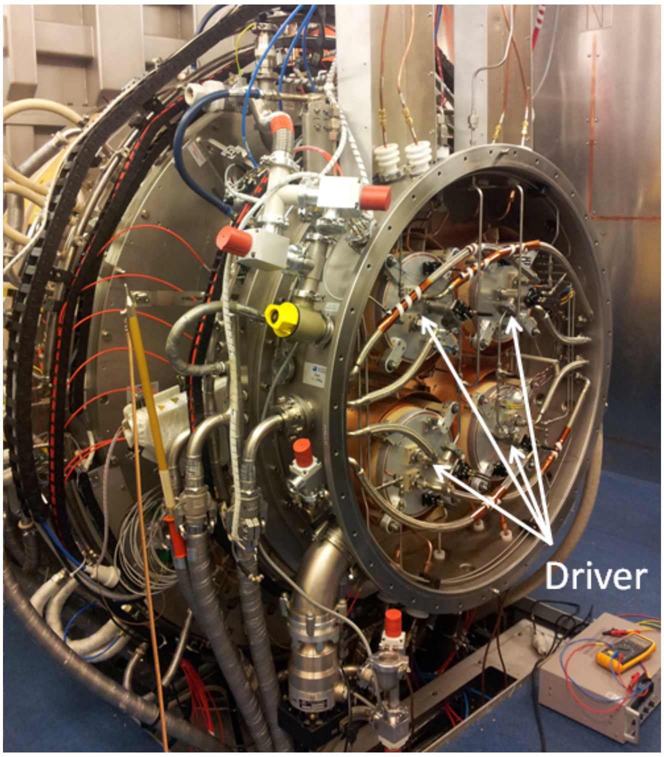

Figure 2.7: *Ion source at the testbed ELISE. The four drivers of the source, which has the half size of the ITER source, can be seen.*

in negative ion sources an extraction phase at low energies (up to 10 keV) is necessary before accelerating the negative ions to their full energy. The reason is to minimise the power input of the co-extracted electrons which are filtered out. The grids are manufactured out of copper because of the necessary heat conductivity. The first grid, the plasma grid, was already mentioned in chapter 2.4.3. The second grid is called extraction grid and the third grid is the grounded grid, since it is on ground potential while the ion source is at high potential.

For the ion acceleration up to 1 MeV, two concepts have been investigated for ITER. The SINGAP (**SING**le Aperture - **SIN**gle **GAP**) has a small pre-acceleration of about 30 keV before accelerating the beam particles in one step to the final energy while the MAMuG (**M**ulti **A**perture **Mu**lti **G**rid) concept divides the acceleration phase into five 200 kV acceleration phases [68]. This improves the voltage holding compared to a single 1 MV acceleration step. Furthermore, electrons generated in the accelerator by collisions between the negative ions and the background gas and which are guided onto the acceleration grids can only gain a maximum energy of 200 keV. This reduces the power density input on the grids. The underlying physical processes are explained in chapter 2.5.2. The

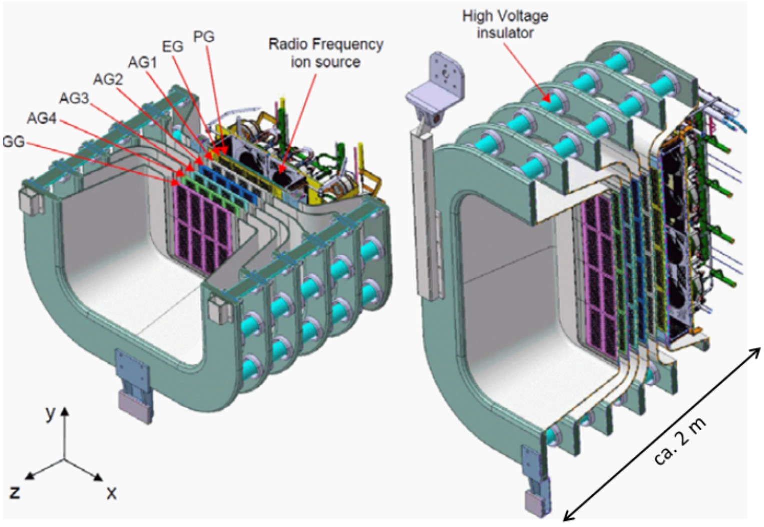

Figure 2.8: *CAD model of the ITER source with extraction system, i.e. the MAMuG accelerator (**Mu**lti **A**perture **Mu**lti **G**rid) [28]. PG is the plasma grid, EG the extraction grid,* AG_x *are the acceleration grids 1–4 and GG the grounded grid* [7]

reference design for the ITER source will be the MAMuG design [11, 69]. In sum the ITER extraction system consists of seven grids which are shown in figure 2.8 in a CAD model.

The geometry of the grid system at the IPP prototype source at BATMAN (the so-called LAG (**L**arge **A**rea **G**rid) system) [23] is different from the one at ELISE. The IPP prototype source operates with the LAG due to historical reasons while the ELISE grid system is based on the ITER SINGAP design [67]. The difference between the LAG and the ELISE grid is in the shape of the drilled apertures, their diameters and the grid distances. Figure 2.9 shows schematically the cut through a single aperture of the LAG system at BATMAN and the ELISE-grid. Table 2.4 summarises the most important geometric parameters of the grids concerning beam optics and aperture number. The aspect ratio between the diameter of the apertures in the plasma grid and the length of the first gap are important parameters for the beam optics. These parameters determine the optimum beam optics and have to be adapted for the expected extraction voltage and the corresponding extracted ion current. The apertures of the plasma grid have a chamfered edge at the front and the back side. Upstream, this shape increases the extraction probability of the negative ions [70]. In the extraction grid,

---

[7] Reproduced with permission from [28]. Copyright 2013, AIP Publishing LLC.

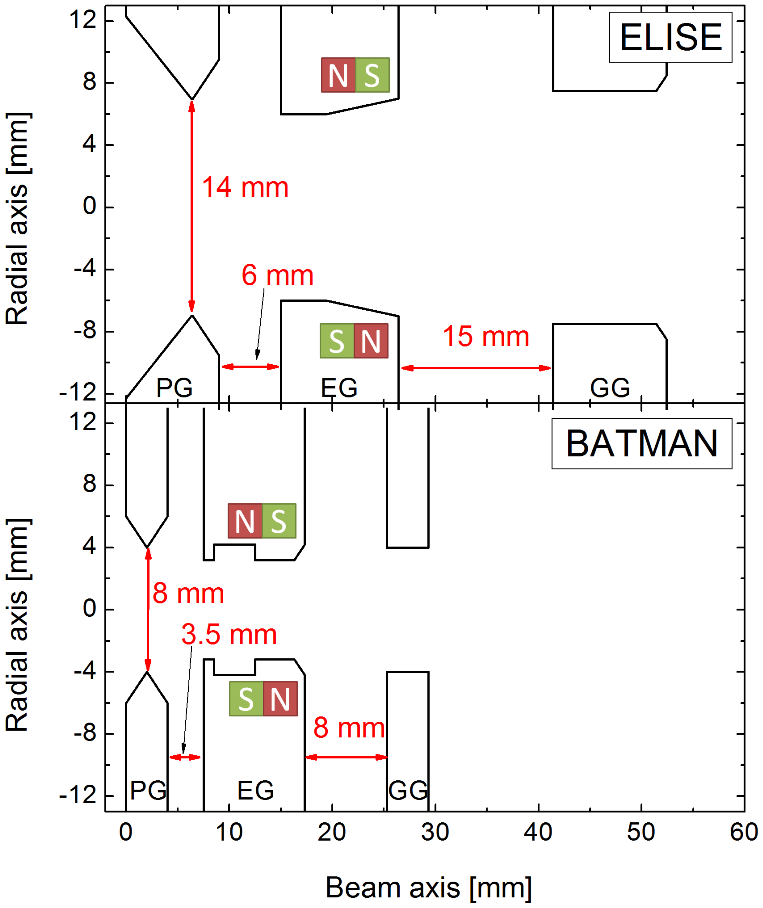

Figure 2.9: *The top part shows the grid shapes of one aperture of the plasma grid (PG), the extraction grid (EG) and the grounded grid (GG) at ELISE. On the bottom part the respective grid shapes for one aperture of the LAG at BATMAN are shown. Permanent magnets are embedded in the extraction grid, generating the electron deflection field.*

horizontal rods of permanent magnets generate the magnetic electron deflection field. It is alternating between the aperture rows. Its orientation is perpendicular to the filter field. The purpose of the electron deflection field is to filter out electrons which are co-extracted. The apertures of the extraction grid at BATMAN have a small pocket. Due to historical reasons, a first magnetic electron deflection field configuration led to a guidance of the co-extracted electrons into this pocket. With the actual magnetic deflection field configuration the co-extracted electrons hit the front surface of the extraction grid [71], therefore the pocket was not implemented in the ELISE extraction grid design. Furthermore, the cooling of the extraction grid at ELISE was improved, which increases the maximum power density input to 40 MW/m^2 on local spots [24].

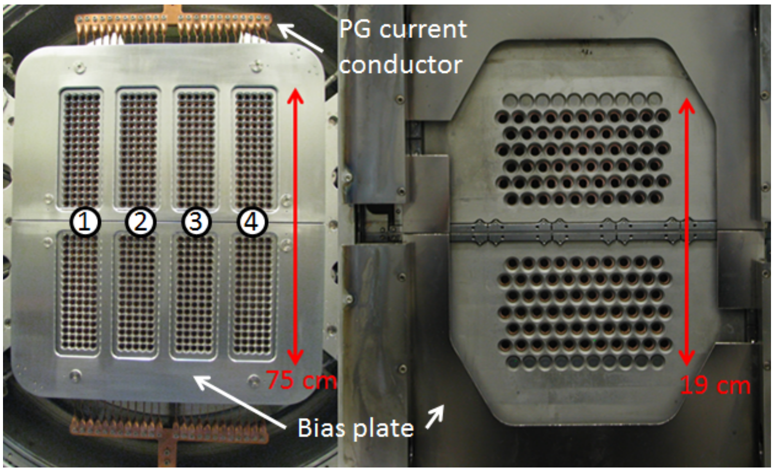

Figure 2.10: *On the left side the plasma grid at the ion source of ELISE with the beamlet groups 1 to 4, each for the upper and lower grid half. On the right side the smaller plasma grid at BATMAN.*

Table 2.4: *Selection of important grid parameters for beam optics.*

Parameter	**LAG at BATMAN**	**ELISE grid**
Apertures	126	640
Diameter apertures plasma grid	8 mm	14 mm
Distance first gap	3.5 mm	6 mm

Figure 2.10 shows a source-side view of the plasma grid from the ion sources at ELISE and BATMAN. Both are molybdenum coated in order to avoid copper release by sputtering, since the copper could affect the work function of the plasma grid (see section 2.4.3). The LAG at BATMAN has 126 apertures which are arranged in a top and bottom grid half. Surrounding the apertures the bias plate can be seen. At ELISE the plasma grid also consists of an upper and lower grid half. The 640 apertures are divided up into eight beamlet groups (beamlet group 1 to 4 for each segment) for technical reasons. Each grid half has four beamlet groups. The bias plate covers the whole plasma grid except for the beamlet groups. On the photo of the ELISE plasma grid additionally the top and bottom connection for power supply of the plasma grid current (PG current), used for generating the magnetic filter field, can be seen.

2.5.1 Negative ion transport in the plasma

On the surface of the plasma grid atoms and positive hydrogen ions coming from the plasma are converted into negative ions via the surface effect according to equation (2.3). Particle-in-cell calculations show the formation of a virtual cathode close to the plasma grid surface when the amount of negative ions is large [72, 73, 74, 75, 76]. The formation of this space charge accumulation comes from the flux of negative ions, which is determined by the fluxes of positive hydrogen ions and hydrogen atoms. For typical plasma parameters in the extraction region of the IPP ion sources (H temperature: 1 eV, H density: $5 \cdot 10^{18}\,\mathrm{m}^{-3}$ [43]) the depth of the virtual cathode is between a tenth and several volts [72, 76]. The negative ions have to overcome this Coulomb barrier with their starting energy. The starting energy is determined by the energy of the impinging particle which is convoluted to a negative ion, the energy reflection coefficient and the energy from the negative ion formation. The depth of the virtual cathode can be decreased by a lower influx of hydrogen atoms or positive ions (which would also decrease the generation of negative ions) as well as by the space charge of positive hydrogen ions or molecules.

The negative ions coming from the plasma grid surface are either directly extracted through the nearest aperture [70] or reach the plasma volume. Two effects however lead to a significant negative ion flux to the plasma grid apertures from the surface-produced negative ions in the plasma bulk. On the one hand the trajectories of a part of the negative ions are bend by the magnetic field towards the extraction. On the other hand negative ions from the surface moving towards the bulk plasma can collide with hydrogen atoms coming from the driver leading to a charge exchange reaction. The resulting negative ion is then directed to the plasma grid [77].

Negative ions which arrive at the plasma grid are extracted through its apertures due to the application of high voltage (in the range of kilovolts) between the grids in the extraction system. In every aperture a small beamlet is formed leading in sum to the whole beam.

Calculations with the transport code TrajAn (see chapter 4.3) have shown that the illumination of a plasma grid aperture with negative ions might not be homogenous due to the involved transport mechanisms (charge exchange and trajectory bending because of the magnetic field) [70, 77]. Figure 2.11 shows the relative ion density of the extracted ions at the meniscus (see section 2.5.2.1) for an extraction voltage of 9 kV calculated by TrajAn. In the center less ions are

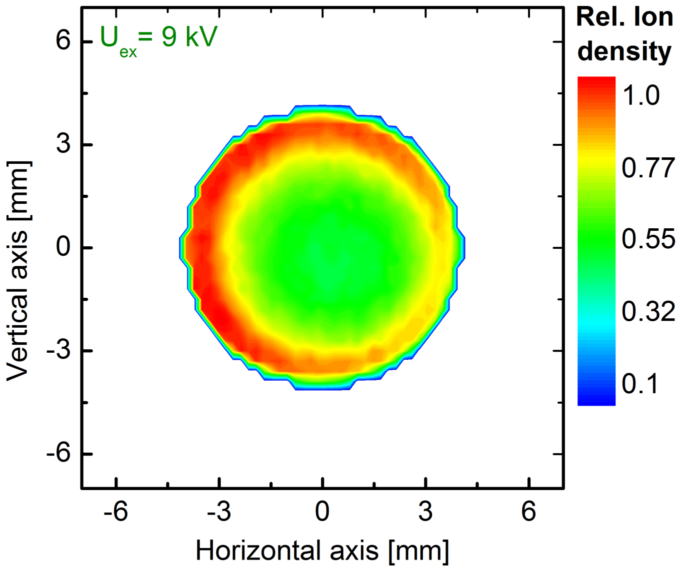

Figure 2.11: *Illumination of a plasma grid aperture by H^- at LAG at BATMAN. The relative ion density of extracted ions is larger at the aperture edge [42].*

extracted than at the aperture edge. Actually the maximum ion density has a crescent shape. These starting conditions can already affect the formation of a beamlet of an individual aperture due to the space charge.

2.5.2 Transport in the extraction system

2.5.2.1 Beam optics

Beam optics are determined by the space charge distribution and the electric and magnetic fields in the extraction system. A meaningful parameter is the perveance.

The extracted negative ions that pass one plasma grid aperture form a beamlet. The development of an ion beamlet along its beam axis in time can be described by the use of the following equations for the radial electric and the poloidal magnetic field E_r and B_φ, and the Lorentz equation describing the forces by the space charge:

$$\begin{aligned} \mathrm{E_r} &= \frac{1}{R\epsilon_0}\int\limits_0^R r\rho(r)\mathrm{d}r\,, && (2.10)\\ \mathrm{B}_\varphi &= \frac{\mu_0}{R}\int\limits_0^R rj(r)\mathrm{d}r\,, && (2.11)\\ m\frac{\mathrm{d}^2R}{\mathrm{d}t^2} &= q(\overrightarrow{\mathrm{E_r}} + \overrightarrow{\mathrm{v}} \times \overrightarrow{\mathrm{B}_\varphi})\,. && (2.12) \end{aligned}$$

$\rho(r)$ is the radial charge density, R the beamlet radius, m the particle mass and $j(r)$ the radial current density. μ_0 is the magnetic permeability and ϵ_0 is the permittivity.

Equation (2.12) can be rewritten with the two equations for the charge density and the time derivative,

$$\begin{aligned} \rho(r)\mathrm{d}r &= \frac{j(r)}{v}\,, && (2.13)\\ \frac{\mathrm{d}}{\mathrm{d}t} &= v\frac{\mathrm{d}}{\mathrm{d}x}\,, && (2.14) \end{aligned}$$

and assuming a particle velocity v only in beam-(x-)direction:

$$m\frac{\mathrm{d}^2R}{\mathrm{d}x^2} = \frac{q}{Rv^3\epsilon_0}(1-\frac{v^2}{\mathrm{c}^2})\int\limits_0^R rj(r)\mathrm{d}r\,. \quad (2.15)$$

c is the speed of light. Since in the ion sources for ITER NBI $v^2 << \mathrm{c}^2$ due to the applied voltages, the term v^2/c^2 becomes zero. The velocity can be substituted by the acceleration voltage in a planar diode:

$$U = \frac{mv^2}{2q}\,. \quad (2.16)$$

Assuming a constant radial current density j_0 within the beam, $j(r) = 0$ for $r > R$ and the substitution for the current density with the beam current $I = R^2\pi j_0$, equation (2.15) can be simplified with the help of equation (2.16):

$$m\frac{\mathrm{d}^2R}{\mathrm{d}x^2} = \frac{I}{U^{3/2}}\left(\frac{m}{8\pi\epsilon_0 q}\right)^{1/2}\frac{1}{R}\,. \quad (2.17)$$

Solving this equation delivers the relation between beamlet radius and propagation length along the beamlet axis which depends on the ion current I and the applied voltage U. For beam optics characterisation the perveance Π is introduced [78]:

$$\Pi = \frac{I}{U^{3/2}} \,. \tag{2.18}$$

The maximum possible extracted current I_{max} for a radial symmetric laminar hydrogen ion beamlet is limited by the Child-Langmuir-Law due to the space charge of the beamlet [79, 80]:

$$I_{\text{max}} = \frac{4}{9}\pi\epsilon_0\sqrt{\frac{2e}{m}}\frac{R^2}{d^2}U^{3/2} \,. \tag{2.19}$$

This equation is valid for an ion beamlet with a radius R in a planar diode of distance d and with a potential drop U. The variable e stands for the elementary charge. The equation shows a characteristic grid parameter for beams, the maximum perveance Π_0, which determines the beam divergence, i.e. the broadening of the beam:

$$\Pi_0 = \frac{4}{9}\pi\epsilon_0\sqrt{\frac{2e}{\mathrm{m}}}\frac{R^2}{d^2} \,. \tag{2.20}$$

For the definition of the divergence ϵ a Gaussian distribution of the angles between the beam axis and the velocity vector of the beam particles after the extraction system (when the space charge compensation fully sets in; see next section) is assumed. The divergence angle is defined as the square root of two times the standard deviation of the Gaussian distribution.

As already mentioned the extraction system of the negative ion source test facilities at IPP consists of three grids (electrodes) which have two different voltages applied. The voltage between plasma grid and extraction grid is called the extraction voltage U_{ex} and between extraction grid and grounded grid the voltage is called the acceleration voltage U_{acc}.

The electric field of the extraction system reaches into the plasma volume where it is compensated by the plasma. A so-called plasma meniscus is formed, which is the boundary of the plasma, i.e. at the potential line $U = 0\,\mathrm{V}$. The shape of this meniscus, which extends into the plasma, depends on the geometry of the extraction aperture, the extraction voltage and the plasma parameters (electron density, electron temperature, plasma potential,...). Because of the electrical conductance of the plasma, the electric field lines from the extraction field are perpendicular to the meniscus at the plasma boundary. The extracted particles are predominantly moving along these field lines, leading to a converging beamlet from the start of the extraction. In positive hydrogen ion sources and negative hydrogen ion sources based on the volume effect where the ions are coming from the plasma bulk, the extracted particles have a small transverse velocity component to the extraction field due to their thermal motion in the plasma [81]. This leads to a small broadening of the beam, which increases the divergence.

In negative ion sources with surface production the particle flux at the meniscus is not fully parallel to the electric field. The reason is the particle generation on the plasma grid surface and the guidance towards the plasma grid by charge exchange reaction or the bending due to the magnetic field. The negative ions can have higher transverse velocities than it would be the case for a laminar flow from the bulk plasma. The origin of negative ion generation and the ion temperature leads to more complex beam particle trajectories to the meniscus than estimated in the simple model of a laminar flow of the ions to the extraction aperture.

The extraction system of the IPP ion sources can be described as a system of electrostatic lenses [82, 83, 84]. The focus points depend on the normalized perveances Π/Π_0. The normalised perveance is used in order to compare grid systems with different geometry. Since two voltages are present in the extraction system, also two normalised perveances can be defined. The reference parameter which is taken for describing the beam optics condition is the normalised perveance obtained from the extracted current density and the extraction voltage. The optimum normalised perveance, where the divergence is at a minimum, is between 0.1 and 0.2 for the IPP negative ion sources. This was shown in experiments at MANITU and with simulations [33].

Figure 2.12 describes three cases for the perveance for a three grid system by means of the LAG. The black doted line indicates the shape of the plasma meniscus. In the three rows of figure 2.12 the shape of the beamlet for the perveance at an optimum value as well as below and above this optimum value is shown. For the optimum perveance in case 1, the beamlet extends radially downstream the focus point of the converging beamlet due to the transverse velocity components of the particles, the space charge and the electric field. However, the electrostatic field of the second gap can compensate this de-focusing to a minimum.

For a perveance below the optimum value (case 2) the focusing point is shifted closer towards the plasma meniscus. The following divergence broadening cannot be compensated anymore by the electric field between extraction grid and

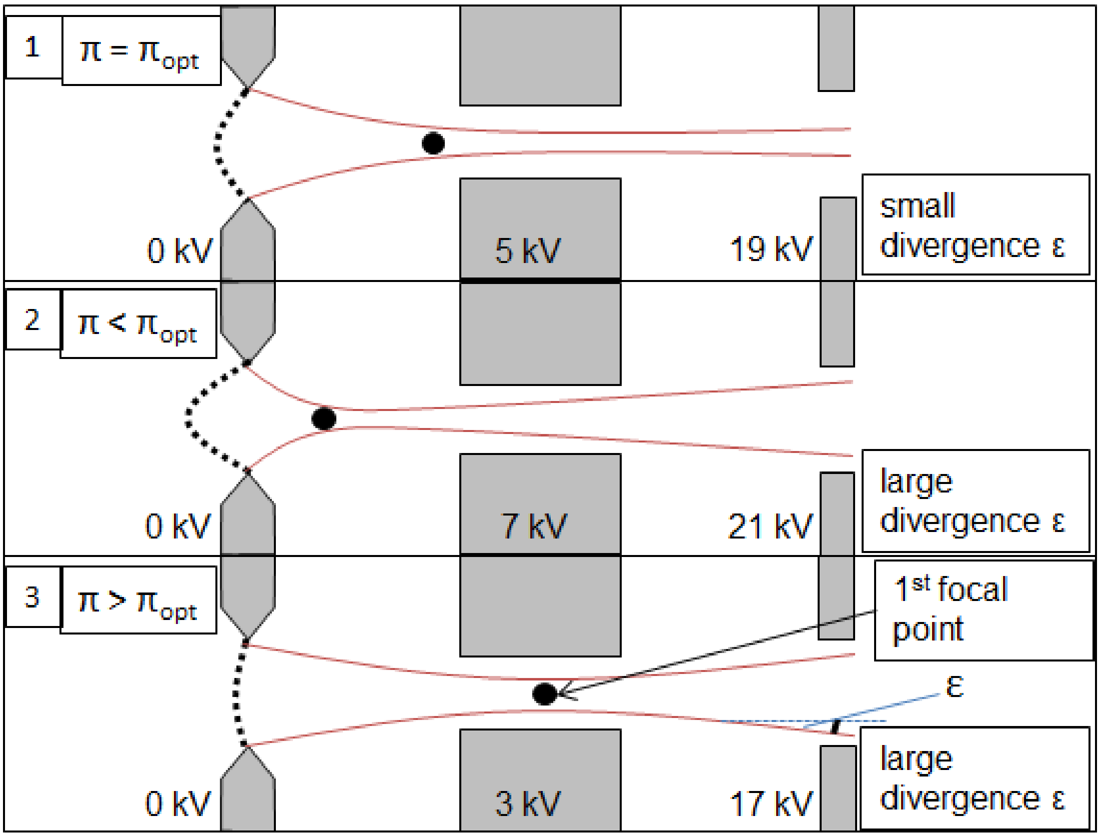

Figure 2.12: *Schematic drawing of the beamlet shape for three perveance cases. On the top illustration, the perveance is at the optimum. In the middle the case for a perveance below and on the bottom the perveance above the optimum perveance is shown.*

grounded grid. The divergence is larger than for the optimum perveance.

In contrast to a perveance case below the optimum case, a high perveance as in case 3 leads to a focusing point downstream the optimum. The divergence angle of the individual particles is comparable to the individual particle angles in case 2 but with a different sign. The electric field of the second gap again is not strong enough to minimise the divergence angle, as in case 2.

The normalised perveance can be parameterised by the divergence of the beamlet. The divergence is minimised at the optimum normalised perveance. In- or decreasing the normalised perveance leads to an increase of the divergence. This behaviour is mainly due to a shift of the focus point of the converging extracted beamlet as shown in figure 2.12.

The behaviour of the divergence with normalised perveance can be seen in

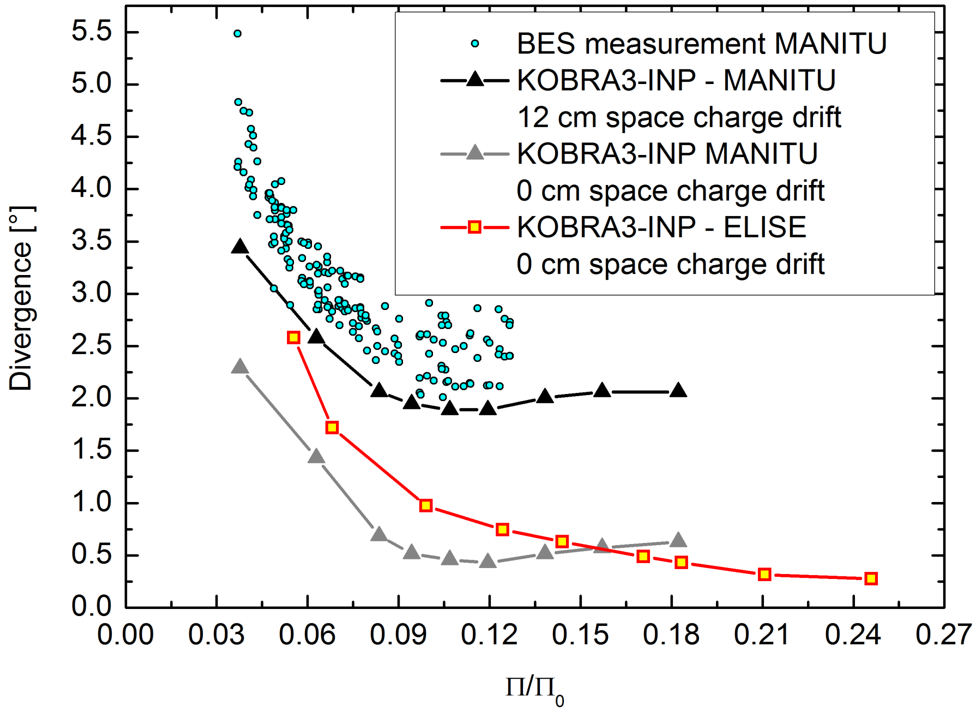

Figure 2.13: *Correlation of the divergence with the normalised perveance [33]. The measurements with beam emission spectroscopy were obtained at MANITU. Furthermore, the results from calculation series with KOBRA3-INP are shown. Two cases are for MANITU, with a different onset of space charge compensation and one case for ELISE with an onset of space charge compensation at the end of the extraction system (0 cm downstream the grounded grid).*

figure 2.13 [33]. It shows measurements of the divergence obtained with beam emission spectroscopy (see section 3.2) at the testbed MANITU. Furthermore the expected divergence for a certain normalised perveance can be calculated with the beam optic codes, e.g. KOBRA3-INP (see chapter 4.3). In the graph three series of calculations are shown. The first two refer to MANITU LAG and differ in the onset of the space charge compensation, which will be discussed more in detail in section 2.5.2.2 and which was set at 0 cm and 12 cm downstream the grounded grid. The third calculation series refers to ELISE with an onset of space charge compensation 0 cm downstream the grounded grid.

As a common behavior, starting from a low normalised perveance (under perveant condition) of ≈ 0.03, the divergence decreases with increasing Π/Π_0. The divergence reaches a minimum at the normalised perveance optimum. With a further increase of the normalised perveance, the divergence would increase again. However, this parameter range is not achievable with the LAG grid due to technical reasons. For this reason also the calculations stop at a normalised perveance of 0.18 respectively 0.24. The calculations show a very flat divergence profile in the perveance optimum which is around 0.1 for MANITU and between 0.15 and 0.25 for ELISE.

In the case of MANITU, it can be seen that an onset of the space charge compensation right at the end of the extraction system (0 cm downstream the grounded grid) leads to very low absolute divergence values, which are below the measurement. Increasing the distance for the onset of the space charge compensation shifts the curve to higher values while keeping the same trend. The reason is due to a longer impact of the repulsive forces from the beam particle charge leading to a larger beamlet broadening.

Experiments at BATMAN showed, that besides the optimum perveance, also the ratio between extraction and acceleration voltage is important for a low beam divergence. In this case the best results were obtained for a ratio larger than 3–4 [85]. The beamlet is rectified by the second electric field. This rectification depends on the electric field strength and is large enough to compensate mainly the ion-ion repulsion with increasing field strength.

2.5.2.2 Beam transport

For negative ions the form of the beamlet (shape, formation, beam physics) becomes even more complex due to heavy particles reactions within the extraction system, co-extracted electrons and plasma grid aperture illumination in sources with surface generated H^-. Figure 2.14 shows a vertical cut of an aperture with an ion beamlet. The scheme can be divided into three regions: The plasma, the accelerator and the drift region. In the first region upstream the plasma grid hydrogen atoms and ions from the plasma are reaching the plasma grid where negative ions are generated. They are guided to the extraction aperture as explained in chapter 2.5.1. Since a significant ($\approx$ 90% [23]) part of the negative ions is not coming from the plasma volume but from the surfaces, as shown in section 2.4.3, the model of a laminar flow of negative ions to the extraction has disadvantages as already explained. An inhomogeneous aperture illumination as mentioned in section 2.5.1 would increase the complexity of the beamlet formation.

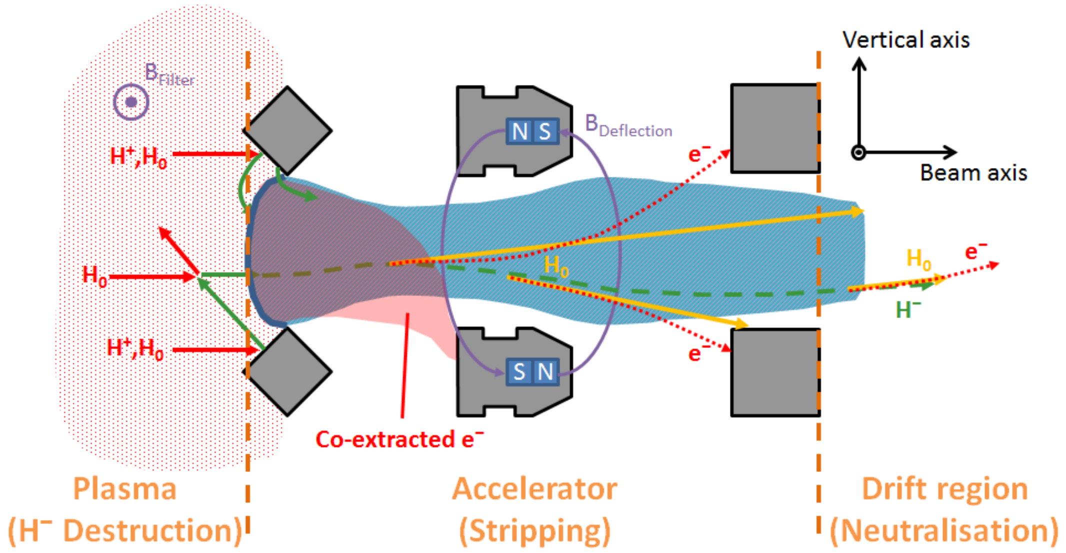

Figure 2.14: *Illustration of the transport and losses of negative ions and electrons in the extraction system.*

Magnetic field deflection

Also present in this first area is the magnetic filter field B_{Filter} which also extends into the second region between plasma meniscus and end of grounded grid. Here, in addition to the electric field, the ion beamlet is affected by the magnetic fields, which leads to a beamlet deflection. Besides the filter field, the electron deflection filter is present. The horizontal and vertical field components of both fields along the beamlet axis are shown in figure 2.15 exemplified for the ELISE grid system. The deflection field is alternating from aperture row to aperture row. In sum, the two magnetic fields lead to a complex 3D topology.

The electron deflection field mainly affects the co-extracted electrons and only slightly the extracted negative ions. The electrons must not be fully accelerated, since they would be able to destroy beamline components by their high power density input. Because of the deflection field $B_{Deflection}$ the co-extracted electrons are guided onto the extraction grid. The cooling ability of the extraction grid and therefore the maximum sustainable power density is the limiting factor for the power input of the co-extracted electrons. Increasing the extraction voltage leads to a higher negative ion current but also to a much higher co-extracted electron current. With the current extraction system the maximum extraction voltage is limited to 10 kV for relevant ITER parameters.

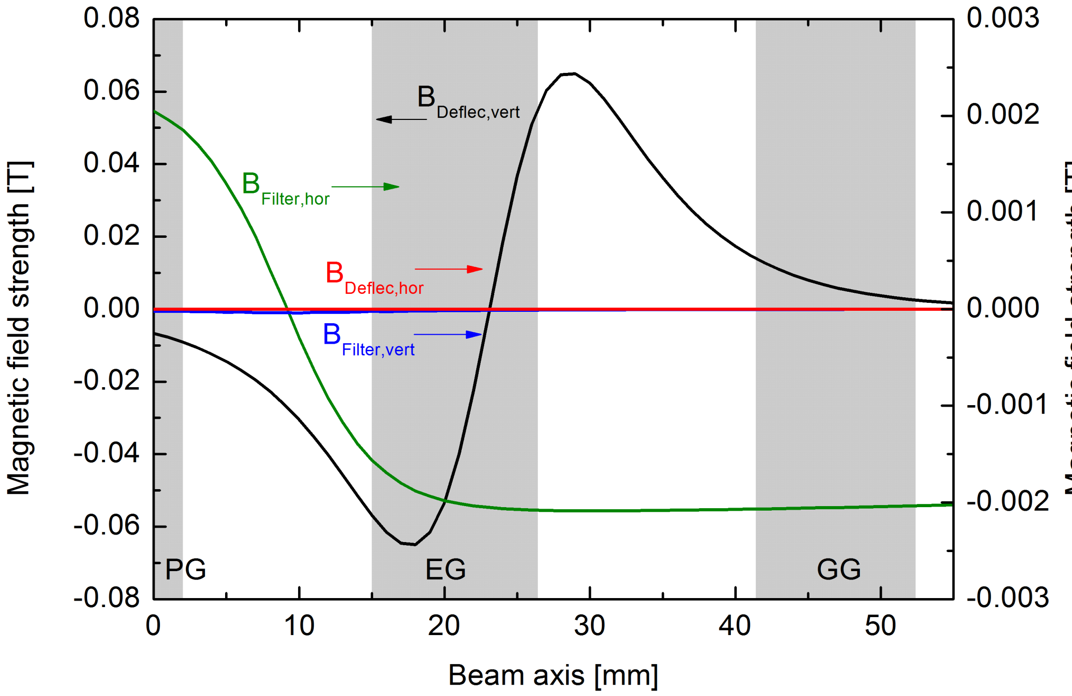

Figure 2.15: *Vertical and horizontal magnetic field components of the filter and deflection field in the extraction system along the beamlet axis.*

The deflection of the ion beam due to the magnetic fields in the grid system can either be in horizontal or vertical direction. In the small source at BATMAN a vertical beamlet deflection of a few centimeters after 1.5 m of beam transmission was observed [85]. If the deflection angle is too large, the beamlets can partially hit beamline components and the beamlet transmission is decreased. There are many ways to counteract to this effect. One possibility is beamlet steering. This means a small horizontally and/or vertically misalignment of the extraction or grounded grid with respect to the beam axis. This leads to a steering angle which can compensate the deflection angle. However, steering is mainly used for beam focussing. For ITER the deflection angle will be compensated by additional magnets (which have the same remanence of 1.1 T as the permanent magnets in the extraction grid) in the acceleration grids [86]. For ELISE, no compensation of the beamlet deflection is present.

Stripping losses

The particles of the beamlet can collide with the background gas in and after the extraction system. For the electron detachment of the negative hydrogen ions in the NBI sources a different nomenclature is used. In the plasma, the detachment (see chapter 2.4.2) is called H^- destruction, which can decrease the extracted current density. In the accelerator the detachment by H_2 is called stripping which leads to a decrease of the maximum possible beam energy, since the created neutral beam particles are not further accelerated. In the drift region the electron detachment by H_2 is called neutralisation, which is then necessary for the upcoming injection into the fusion plasma. The main particle collisions in the extraction system and drift region are the following (the index f marks the fast beam particles, while the other particles are background gas particles which are comparatively slow):

$$\text{H}^- \text{ stripping} \qquad \mathrm{H_f^- + H_2 \;\rightarrow\; H_{0,f} + e^- + H_2}\,, \tag{2.21}$$

$$\text{H}_0 \text{ ionisation} \qquad \mathrm{H_{0,f} + H_2 \;\rightarrow\; H_f^+ + e^- + H_2}\,, \tag{2.22}$$

$$\text{H}^- \text{ double stripping} \qquad \mathrm{H_f^- + H_2 \;\rightarrow\; H_f^+ + 2e^- + H_2}\,, \tag{2.23}$$

$$\text{H}_2 \text{ ionisation} \qquad \mathrm{H_{0,f} + H_2 \;\rightarrow\; H_{0,f} + e^- + H_2^+}\,, \tag{2.24}$$

$$\text{H}^- \text{ excitation} \qquad \mathrm{H_f^- + H_2 \;\rightarrow\; H_{0,f}}(n=3) + \mathrm{e^- + H_2}\,, \tag{2.25}$$

$$\text{H}_0 \text{ excitation} \qquad \mathrm{H_{0,f} + H_2 \;\rightarrow\; H_{0,f}}(n=3) + \mathrm{H_2}\,, \tag{2.26}$$

$$\text{Dissociative excitation} \qquad \mathrm{H_{0,f} + H_2 \;\rightarrow\; H_0 + H_0}(n=3) + \mathrm{H_{0,f}}\,. \tag{2.27}$$

The cross sections for the relevant energy range at BATMAN and ELISE are shown in figure 2.16 [87, 88, 89]. The cross sections for the excitation reactions are all in the same order of magnitude. In terms of the other collision reactions, reaction (2.21) is the most dominant one, followed by (2.22). Within the presented energy range, the cross sections are almost constant for energies above 5 keV/amu.

The reactions (2.25) - (2.27) generate excited hydrogen atoms. The de-excitation leads to H_α Balmer line radiation. This light can be used for beam diagnostics (see chapter 3.2).

Beside stripping, the accompanied formation of positive ions in the extraction system is critical. These ions are accelerated back into the source. Experimental results show a flux of these backstreaming ions between 1.4% and 2.1% of the flux of extracted negative ions [90]. For ITER it is estimated that the power transported back into the source, which can be deposited on the backplate of the source, is at 880 kW with a maximum power density of 25 MW/m^2 [91] on local spots with a diameter in the range of mm. This means that backstreaming ions

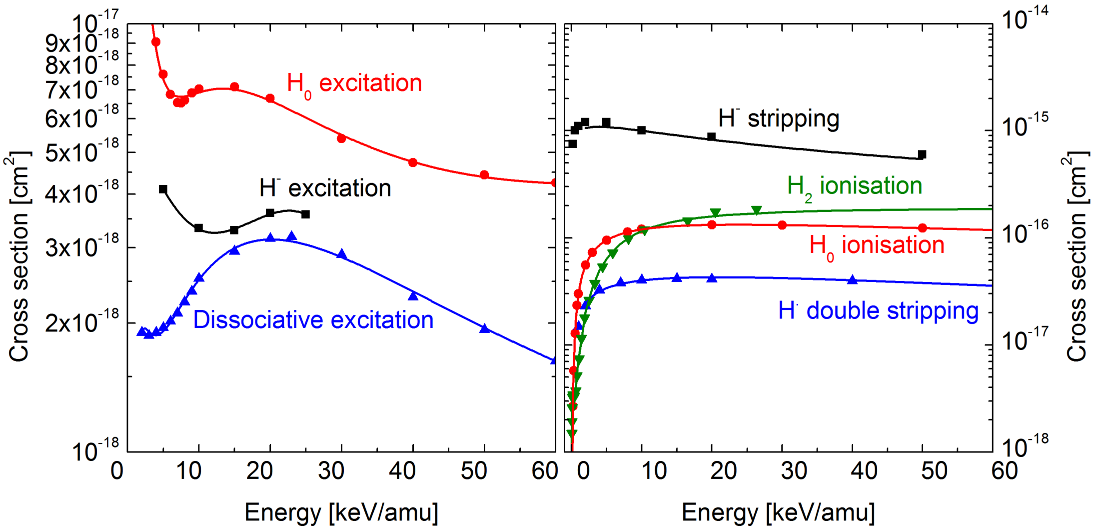

Figure 2.16: *Cross sections for the reactions (2.21) - (2.27). The left graph shows the excitation reactions while the right graph shows the other reactions [87, 88, 89].*

could lead to severe damages of the ion source. Therefore it is a necessity to reduce their production rate.

The loss on stripped particles f_S depends on the accumulated cross section σ_{strip} for the reactions (2.21), which is the dominating reaction, (2.25) and on the density profile of the background gas $n(x)$ along the beamlet axis. In a 1D model the loss from the extraction (defined as zero on the beam axis) to the end of the extraction system (coordinate ξ on the beam axis) can be described by the formula [90]

$$f_S = 1 - \exp\left(-\int_0^{\xi} n(x)\sigma_{\text{strip}}(x)\mathrm{d}x\right) . \tag{2.28}$$

The H_2 density profile in the extraction system cannot be measured directly since this part of the source is difficult to be accessed by diagnostics. Pressure measurements in the source and the tank as well as the gas temperature determination in the source can only give an indication on the gradient of the density profile. Without knowing the density profile modeling of the stripping losses, which could deliver design improvements that could reduce the losses, is difficult. The model, predicting 30% stripping losses at ITER [22], forecasts stripping losses in the three grid system at BATMAN/MANITU of about 8% at an ITER relevant pressure while measurements show about 3% stripping losses only [92]. The reason for the deviation might come from the evaluation of the stripping losses from BES spectra and also from an obtained H_2 density profile, which is not realistic enough.

Additionally, an increase in the stripping losses has been observed at MANITU with increasing normalised perveance [93]. Calculations with EAMCC (see section 4.1) or Excelstrip (see section 4.3.3) were not able to reproduce this behaviour.

It is a task of the thesis to improve the evaluation of the stripping losses from BES spectra. However, the validation of the density profile is still an open point. Nevertheless it is important for the calculation of backstreaming ions. Because of this, one part of this thesis will also deal with a rough reconstruction of the density profile (see chapter 5.4).

Grid losses

In figure 2.14 two stripping reactions are shown referring to equation (2.21). The products, namely electrons and hydrogen atoms, can either leave the extraction system or impinge on the grids, where the electrons together with negative ions, which are not well focused by beam optics, lead to a grid current, which can be measured in the IPP ion sources for the respective grid. An additional source for a current through the grid can also come from negative ions. This is due to poor normalised perveance conditions, aberration effects, a non-Gaussian beamlet shape (i.e. no Gaussian angular distribution of the accelerated particles) or maybe from a so-called halo, which could be present because of the complex beamlet formation which is not fully understood yet. For ITER, this halo is defined by assuming a double Gaussian divergence profile of the beamlet [1]. According to this definition, the core beamlet consisting of 85% of the beamlet particles has a Gaussian divergence profile with a divergence between 0.17° and 0.40°. The halo consists of 15% of the beamlet particles with a divergence of 0.86°. This means that the divergence of a halo is $2-5$ times larger than the core beamlet. The halo definition is important for beam calculations on the transmission for the ITER NBI.

Space charge compensation

Additionally the reactions (2.22) and (2.24) shown in figure 2.16 create positive ions in the ion beamlet. The positive ions lead to space charge compensation

(SCC) since they introduce an attractive force to the negative ions, which reduces the beamlet broadening by the space charge of the negative ions [94]. Due to the mean free path length of the negative ions in the beam, the space charge compensation fully sets in a certain distance after the extraction system. However determining the onset and degree of SCC along the beamlet axis is complex. Common theories assume slow positive ions within the whole beam from the extraction [95]. But in the ion sources for ITER NBI the positive ions created within the extraction system are accelerated back into the ion source. Therefore the positive ion density along the beamlet axis determining the SCC has to be calculated with self-consistent models. Such models are not available so far. At MANITU a comparison between experimental measurements and a simple simulation show a full onset of the space charge compensation 12 cm downstream the grounded grid (see figure 2.13)[33].

Beam inhomogeneity

As already explained in chapter 2.5.1, the beam consists of several hundred beamlets. Each beamlet carries a certain current density of negative ions determined by the negative ion generation on the surface of the plasma grid, mainly at the chamfered area and the flat area around a specific aperture. Deviations of the extracted current density between two beamlets already lead to a development of an inhomogeneous beam. The beam inhomogeneity Υ is defined as follows: "The current density at a certain aperture should not exceed 10% of the mean value of all others"[8].

$$\Upsilon = \frac{\max(|j_i - \frac{1}{N}\sum_{i=1}^{N} j_i|)}{\frac{1}{N}\sum_{i=1}^{N} j_i}\,, \tag{2.29}$$

j_i is the current density of the ith beamlet from all beamlets N. As already mentioned in chapter 2.3, Υ should not exceed 10 %. Assuming a relative error for Υ which is $\Delta\Upsilon$, which should be below 10%, this means for the measurement of j_i that the relative error Δj_i should be less than 5% (see chapter A). Since the current density of a single or several beamlets cannot be measured directly, a local beam divergence is determined by obtaining a vertical divergence profile of the beam. As explained in 2.5.2.1 the beamlet current density is proportional to the beamlet divergence at a fixed extraction voltage. The determination of the beam inhomogeneity is a key topic of this thesis and will be discussed in 5.2.

---

[8] The definition is commonly agreed by the ITER NBI community.

3 Diagnostic tools and methods

At the testbeds BATMAN and ELISE several diagnostic tools for determining the beam parameters are in operation. The major beam diagnostic applied in this thesis is the **B**eam **E**mission **S**pectroscopy (BES). However, there are also additional diagnostic devices, which will be shortly explained. Their position in the beamline are shown in figure 3.1 in a CAD model of the testbed ELISE. The figure presents the part of the beamline between grounded grid and the calorimeter which is installed in a large tank (several m^3).

3.1 Basic diagnostic tools

Grid currents: The currents deposited onto the grids as well as the current back to the HV supply are measured. Figure 3.2 shows exemplarily the high voltage circuit at BATMAN. At this testbed it was shown that in optimum normalised perveance conditions over 95% of the current flowing on the extraction grid comes from co-extracted electrons [23]. The current on the grounded grid, as well as on all other grounded surfaces in the tank, has its origin in the extracted negative ions. The grounded grid current shows the grid losses of negative ions due to several reasons (see chapter 2.5.2).

Wire calorimeter: At ELISE, downstream the grounded grid, the ion beam passes a so-called wire calorimeter. It consists of 50 vertical and 50 horizontal arranged tungsten wires (⌀ 0.2 mm) with a spacing of 20 mm [96]. They are heated up by the beam and the emitted light is detected via an optical camera. A rough estimation of the beam conditions (i.e. a beam inhomogeneity) can already be recognized during the pulse with this calorimeter. Additionally it allows to study the vertical and horizontal centre of mass position of the beam. This is of interest in order to determine the averaged deflection angles of the beam. Figure 3.3 shows a photo of the heated wire calorimeter during a beam pulse at ELISE. Due to the grid geometry with eight beamlet groups and the good normalised perveance conditions close to

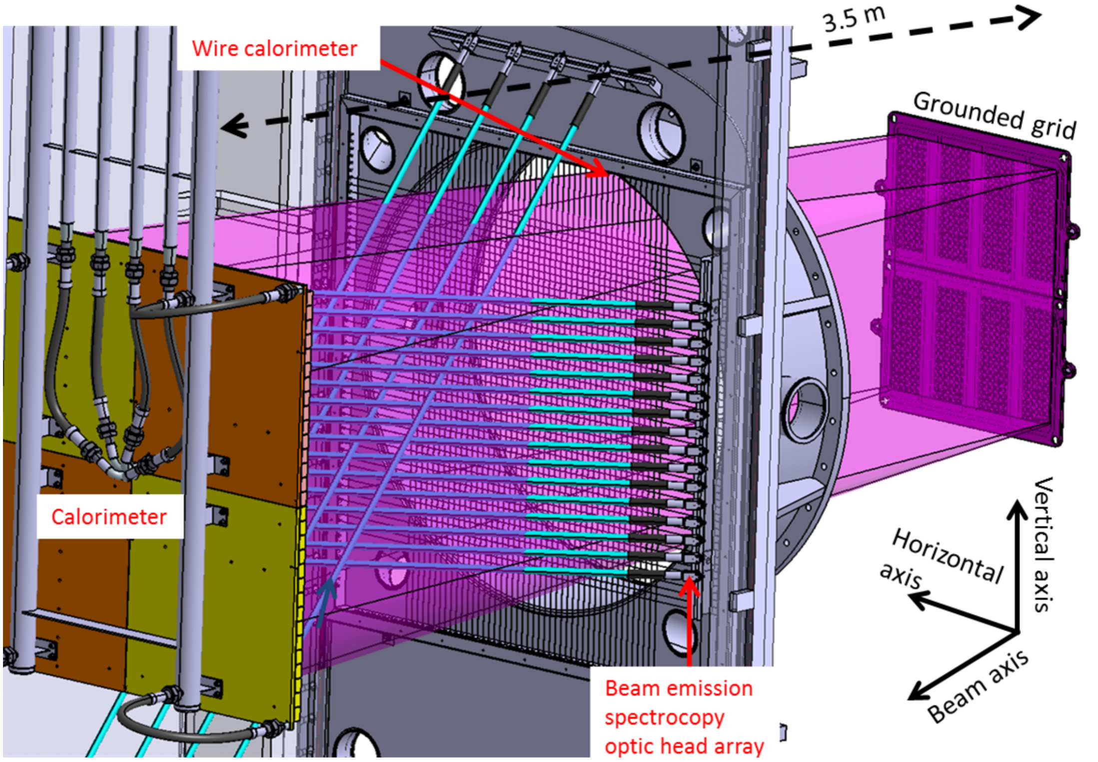

Figure 3.1: *Beamline with the diagnostic tools beam emission spectroscopy, wire calorimeter and calorimeter at the ELISE testbed.*

the optimum (divergence $\epsilon \leq 2°$), the thermal heat distribution represents the aperture composition.

Beam emission spectroscopy: Downstream the wire calorimeter, the beam is diagnosed by the BES. This tool will be explained in detail in the next chapter 3.2

Calorimeter: Finally, the beam hits a water-cooled copper calorimeter. Figure 3.4 shows the two calorimeters for the two IPP testbeds. On the left side the BATMAN calorimeter is shown. It is a single copper plate with a width of 600 mm, a height of 600 mm and a depth of 5 mm. 29 thermocouples aligned as a cross are brazed inside the copper. The thermocouples give the possibility to provide a 2D power density profile of the beam.

On the right side of figure 3.4 the diagnostic calorimeter at ELISE is shown. It consists of four plates with a width of 600 mm, a height of 600 mm and a depth of 41 mm. Together they cover an area of 1200 mm × 1200 mm. Every copper plate is divided up into 15 x 15 copper blocks of 40 mm × 40 mm

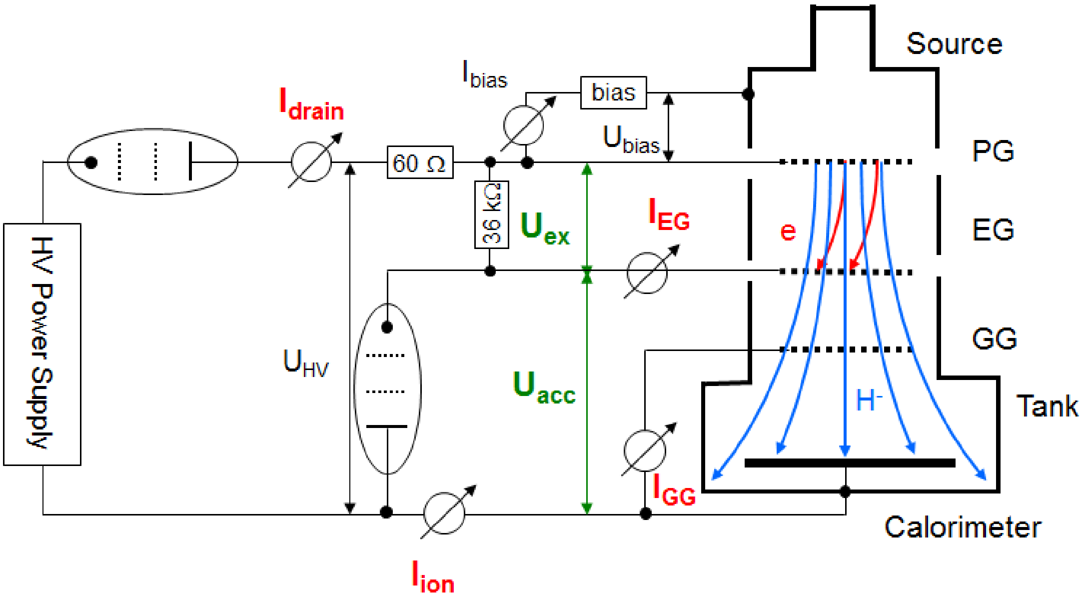

Figure 3.2: *High voltage circuit used for the negative hydrogen ion sources for NBI, exemplarily shown from BATMAN [23].*

[96]. The temperature evolution due to the beam power input is mainly independent for every block, since there is a small spacing between the blocks. By blackening the surface and observing the diagnostic calorimeter with an infrared camera, the temperature evolution of each block can be measured. Thus, a full map of the power density profile can be determined. Additionally, 48 blocks (12 per plate) have thermocouples embedded. With this measurement and a subsequent 2D fit it is also possible to provide a power density profile. The diagnostic calorimeter started its operation in 2014.

3.2 Beam emission spectroscopy

With the beam emission spectroscopy (BES), the H_α light coming from the beam, as described in chapter 2.5.2, is analysed inside one line-of-sight. The choice for the H_α line comes from its emissivity, which is the largest one compared to the other spectroscopic hydrogen radiation lines. BES will be the major beam diagnostic tool for SPIDER, MITICA and ITER NBI due to its simple setup and capability to measure the important beam parameters [97, 98]. The diagnostic technique has been routinely used in NBI ion source for positive ions [99, 100, 101].

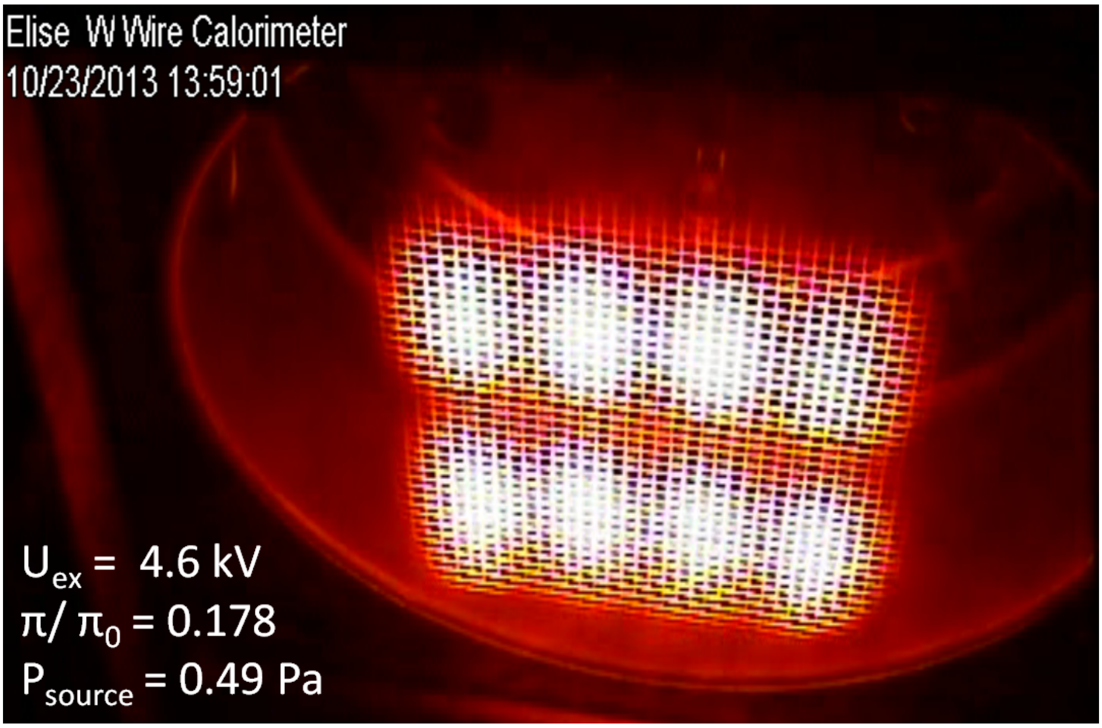

Figure 3.3: *ELISE tungsten wire calorimeter heated up by the beam.*

In these relatively small sources (comparable to the size of the ion source at BATMAN or smaller) the error of the beam property evaluation which comes from the size of the source and accompanied geometry effects (which will be explained in this chapter) is negligible. However the adaption to negative ion sources for NBI which are large compared to positive ion sources is not straight forward and a major topic in this thesis. At BATMAN and ELISE several lines-of-sight are present in order to obtain some spatial resolution.

Since the main production channel of the negative ions is the conversion of hydrogen atoms (see chapter 2.5.1), which come mainly directly from the driver, a homogeneous beam is expected. However, if a inhomogeneous beam appears, it is more likely to be in vertical direction due to the vertical plasma drift in front of the plasma grid. Therefore the lines-of-sight are predominantly in a vertical arrangement.

The position of the BES optic heads in the beamline (downstream the extraction grid system) was already presented in figure 3.1. A BES optic head consists of a lens, with a diameter of about 20 mm, which focuses the collected light to an optic fibre. The fibre is connected to a spectrometer. In order to protect the lens from the coverage of impurities, it is installed inside a pipe with a length of

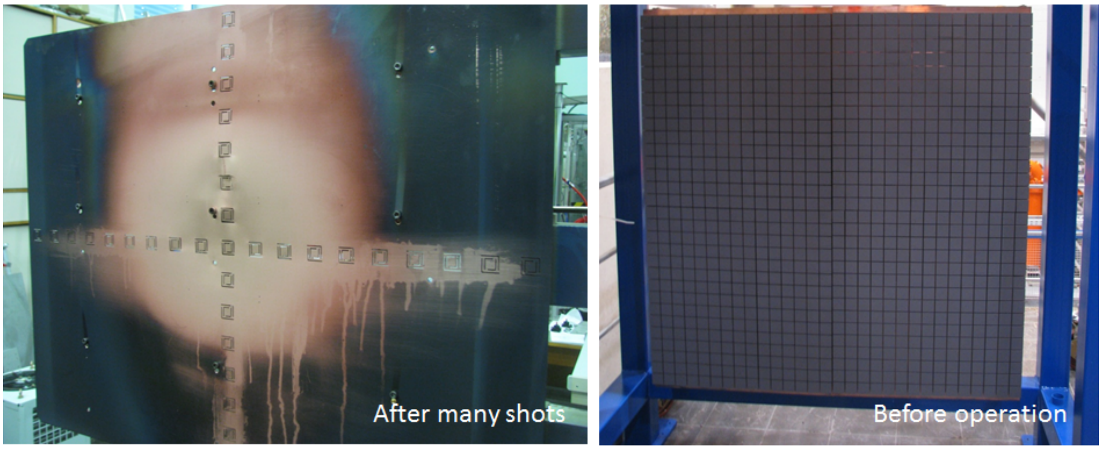

Figure 3.4: *On the left side the calorimeter at BATMAN (600 mm× 600 mm). Thermocouples are arranged as a cross and thermally separated as good as possible by special cuttings. On the right side the ELISE diagnostic calorimeter (1200 mm× 1200 mm) with blackened surface for infrared measurement.*

175 mm. A sketch of a line-of-sight can be seen in figure 3.5. Due to the non-perfect optic of the lens the line-of-sight has a broadening which was measured to be approximately 0.6°. The focus point of the optic head was set to infinity. θ is the observation angle between the beam axis and the line-of-sight axis in the plane of the line-of-sight axis and the beam axis. Since the beam particles are at high velocity, the wavelength of the emitted photons is shifted from the normal wavelength λ_0. The wavelength shift depends on the particle velocity and the observation angle. The wavelength $\lambda_{\mathrm{Doppler}}$ of the Doppler shifted peak for the 2D case (plane of the line-of-sight) refers to the fully accelerated negative ions merged into excited hydrogen atoms by collision reactions and is described by the following formula [101]:

$$\lambda_{\mathrm{Doppler}} = \lambda_0 \left(1 + \frac{v_0}{c} \cos\theta\right) . \tag{3.1}$$

λ_0 is the wavelength of the unshifted H_α peak (H_α: 656.28 nm, D_α: 656.10 nm), v_0 is the velocity of the radiating particle. An observation angle above 90° leads to a blue shift, while an angle below 90° leads to a red shift. The choice of the observation angle is determined by two reasons. First, the overlap of the Doppler shifted and the unshifted peak should be minimised as much as possible. Second, both peaks should be in the wavelength range within one exposure of the utilised spectrometer.

Figure 3.6 shows a photo of the BES optic heads at ELISE while figure 3.7

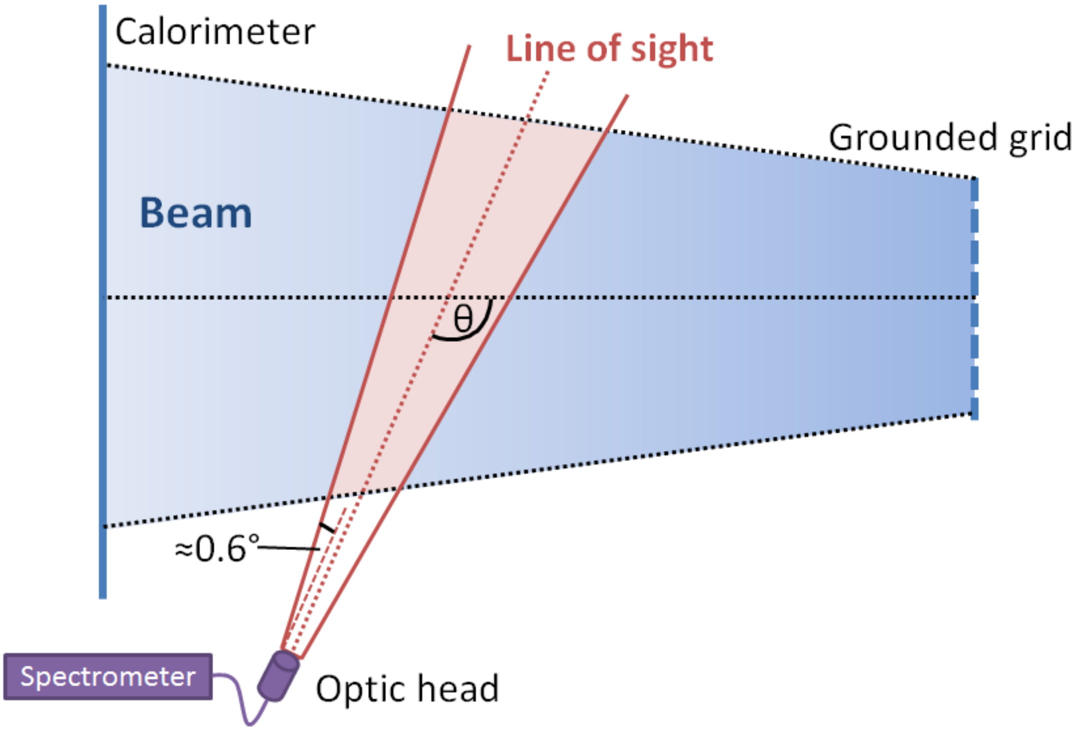

Figure 3.5: *Scheme of a BES line-of-sight. θ is the observation angle between beam axis and line-of-sight axis. The broadening angle of the line-of-sight cone is approximately 0.6°.*

illustrates the setup at BATMAN. At ELISE, a vertical array of 16 horizontal and a horizontal array of 4 vertical lines-of-sight (LOS) is installed symmetrical to the vertical respectively horizontal center of the beam. The lines-of-sight are named by numbers, whereupon LOS # 1 ist the lowermost and LOS # 16 is the topmost horizontal line-of-sight. This means the first eight lines-of sight are in the vertical region of the lower grid segment and the second eight lines-of sight are in the vertical region of the upper grid segment. LOS # 17 is on the very right and LOS # 20 is on the very left side. The observation angle θ for all LOS with respect to the beam axis is 50°. The spectrometer properties will be explained on the next page. The vertical distance between the horizontal LOS (vertical aligned optic heads) is 50 mm. The vertical LOS (horizontal aligned optic heads) are installed in the horizontal center of the beamlet groups. The horizontal distance between them is 160 mm. The optic heads are positioned approximately 2 m downstream the grounded grid.

At BATMAN, five optic heads are arranged in a vertical array. The centered optic head is vertically located in the center of the beam. The observation angle θ

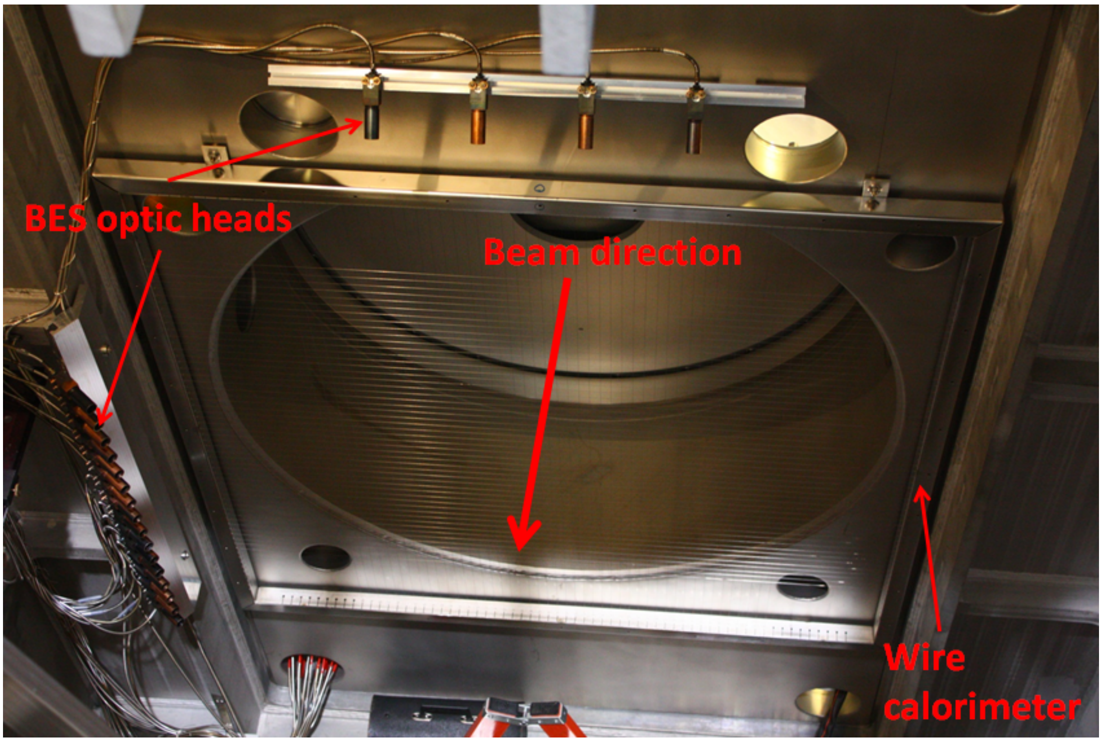

Figure 3.6: *Setup of the optical heads of the BES and of the wire calorimeter at ELISE.*

is 123° leading to a blue shift of the Doppler shifted peak. There are two reasons for choosing this angle. Firstly the line-of-sight should observe in counter beam direction, since at BATMAN a special calorimeter is planned to be operated in 2014 at a position closer to the grounded grid than the optic heads of the BES system. Secondly, the lines-of-sight should end on a surface, where expected reflections are as low as possible (This is important for every BES system). The position of the optic heads is roughly 1.2 m downstream the grounded grid.

In 2012 at BATMAN, in a first preliminary setup, only two lines-of-sight were installed with optic heads outside the tank observing through a window. Their distance from the grounded grid in beam direction was at approximately 1.5 m. Their vertical position with respect to the center of the plasma grid was 50 mm below the center with an observation angle of the first line-of-sight of 117° and 15 mm above the center and with an observation angle of the second line-of-sight of 119°. The BES spectra obtained at BATMAN which will be shown in this thesis were obtained with the first line-of-sight of the preliminary BES setup.

The optic heads are connected via 400 μm optic fibres to a multi channel spectrometer. Two high resolution spectrometers are in operation. At ELISE it is

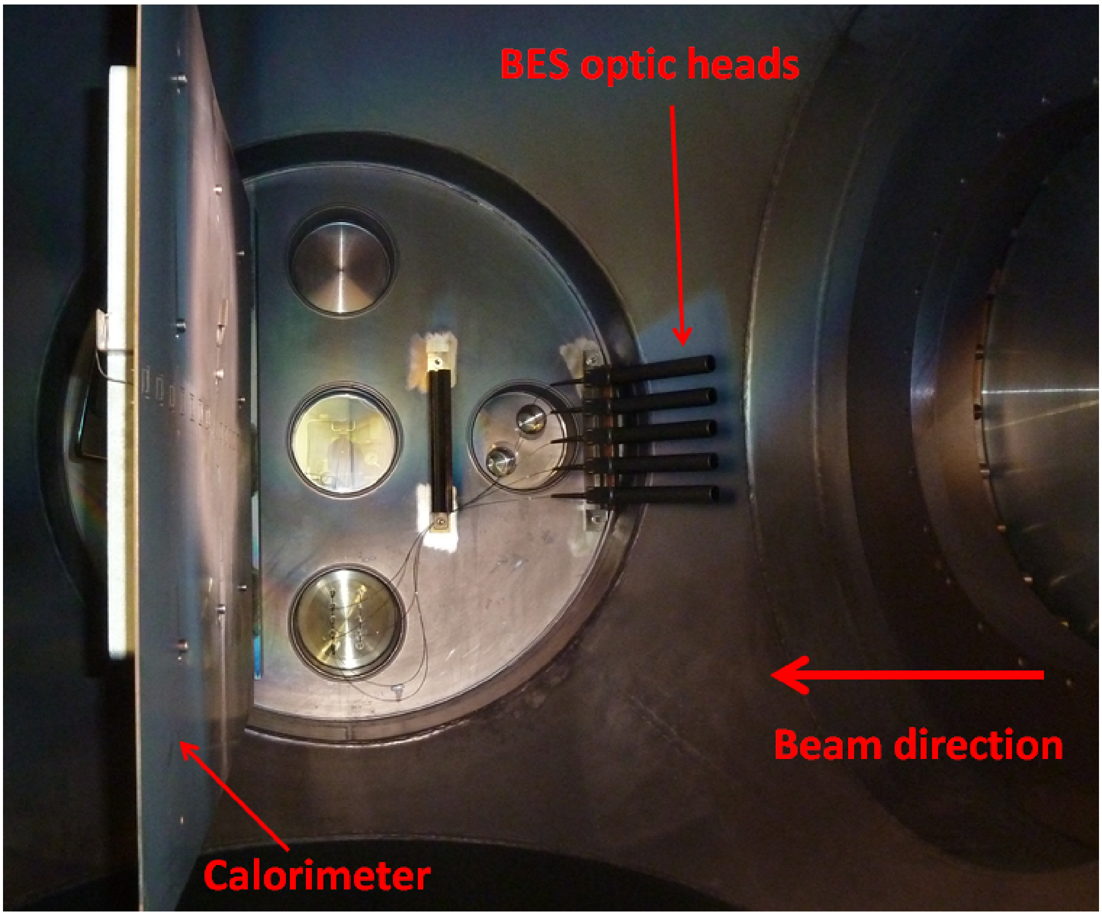

Figure 3.7: *Setup of the BES optic heads and calorimeter at BATMAN.*

an Acton[9] spectrometer equipped with a CCD, at BATMAN an Andor[10] spectrometer, also equipped with a CCD, is used. The high wavelength resolution of the spectrometer CCDs is necessary since peaks from line radiation with a standard deviation of $< 0.5\,\mathrm{nm}$ have to be recorded by the BES system for a subsequently evaluation in order to obtain the beam parameters, i.e. divergence and stripping losses. Still, the peak has to consist of a sufficient amount of data points (> 30) in order to perform fit procedures for the BES evaluation (see section 3.2.2). Table 3.1 shows the properties of the spectrometer. With a high wavelength resolution of $7\,\mathrm{pm/pixel}$ and a low apparatus profile of $0.042\,\mathrm{nm}$, the Acton spectrometer at ELISE is more powerful than the Andor spectrometer with a wavelength resolution of $12 - 15\,\mathrm{pm/pixel}$ and a low apparatus profile of $0.106\,\mathrm{nm}$. These spectrometer specifications are sufficient for the BES measure-

---

[9] Princeton Instruments (Roper Industries, Inc.)

[10] Andor Technology Ltd. (Oxford Instruments)

Table 3.1: *Properties of the BES spectrometers at ELISE and BATMAN.*

Parameter	**ELISE** (Acton)	**BATMAN** (Andor)
Channels	20	5
Apparatus profile	0.042 nm	0.106 nm
Wavelength range	8 nm	30 nm
Wavelength resolution	7 pm/pixel	12 − 15 pm/pixel
Grating	1800 lines/mm	2400 lines/mm

ment. The resolution of the Acton spectrometer results into a small wavelength range of 8 nm which can be obtained during one exposure. This is still sufficient for measurements at ELISE. At the designed parameter of 60 kV total voltage, the wavelength range is exploited almost completely including some safety margin.

Figure 3.8 shows again a schematic drawing of one BES line-of-sight but here with all the angles being important. The beam propagates from the grounded grid to the calorimeter while broadening up due to its divergence. The trajectory angle τ of a beam particle is defined as the angle between particle trajectory and beam axis in the plane of the line-of-sight axis and the beam axis. The two trajectory angles τ_i and τ_j are exemplarily for two beam particles i and j. The light detected from the beam particles is blue shifted; the extent of this shift depends on the detection angle with respect to the beam axis of the radiating particle.

Due to the geometry the light collected from the beam has a different emissivity for individual volume elements. Two different reasons can be separated:

Area-effect: As illustrated in figure 3.8, two areas A_i and A_j of the line-of-sight can be defined in the beam. The areas are separated by the beam axis, with $A_\mathrm{j} > A_\mathrm{i}$. This means by the different area size, in A_j more radiating particles are detected. These particles (due to θ) lead to a higher amount of less blue shifted photons.

Angle-effect: The emissivity measured in one line-of-sight coming from two different volume elements also depends on the distance of the volume element to the optical head. For each volume element a solid angle can be specified. The solid angles define the part of the emitted photon field, which can be seen by the detector. Assuming the same emissivity for two elements V_i and V_j, the part of the detected light from V_i is larger than from V_j because the solid angle of the optics ω_i is larger than ω_j.

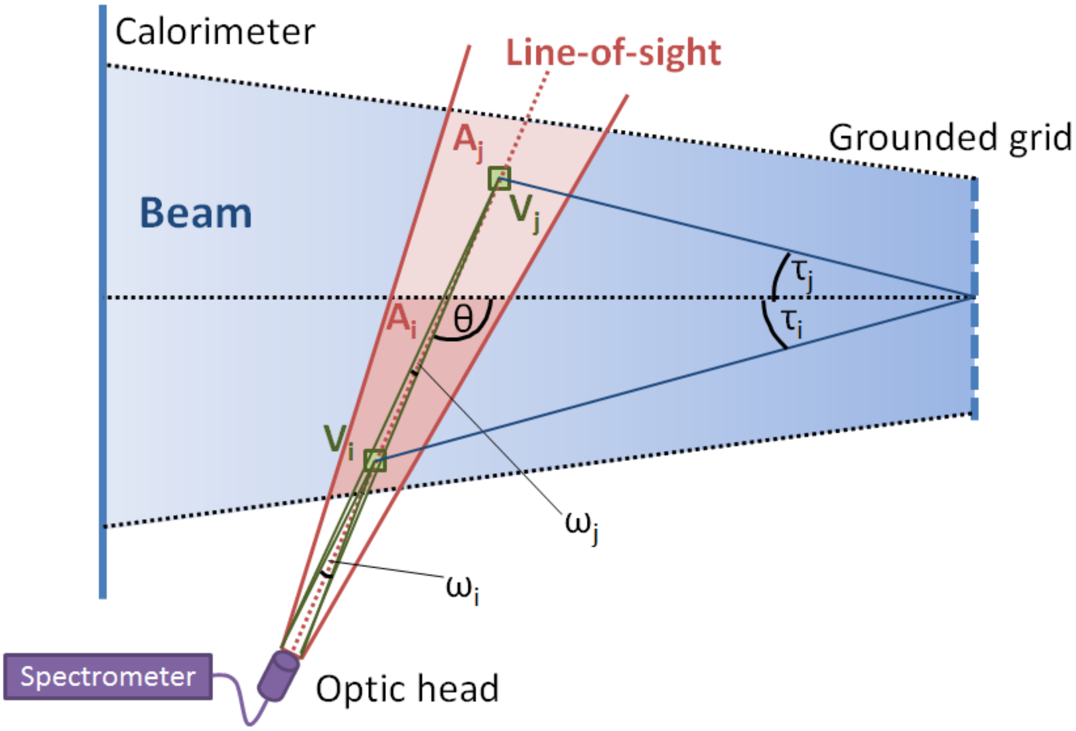

Figure 3.8: *Scheme of a BES line-of-sight. τ_i and τ_j are the trajectory angles for two randomly taken beam particles. In this case, τ_i is positive and τ_j is negative. A_j is the overlap area between the line-of-sight and the part of the beam containing particles with a negative trajectory angles; A_i is the area for positive trajectory angles. V_i and V_j are small volume elements for positive and negative trajectory angles.*

It is part of this thesis, to determine the influence of these two effects on the BES spectrum.

3.2.1 Typical BES spectrum

Figure 3.9 shows a typical hydrogen BES spectrum recorded at BATMAN. The unshifted H_α peak can be seen on the right side at 656.28 nm. The light origin from the beam was described in reaction (2.27)(dissociative excitation). In the case of BATMAN with its preliminary BES setup the unshifted H_α peak also originates from reflections of the plasma light in the source. Measurements, which where done in the scope of this thesis, showed that the amount of the reflected part of the plasma light is usually around 10%. It can go up to 50% for low extracted current densities, which are directly related to the particle flux and the accompanied radiation. Additionally, a small D_α is visible which comes from

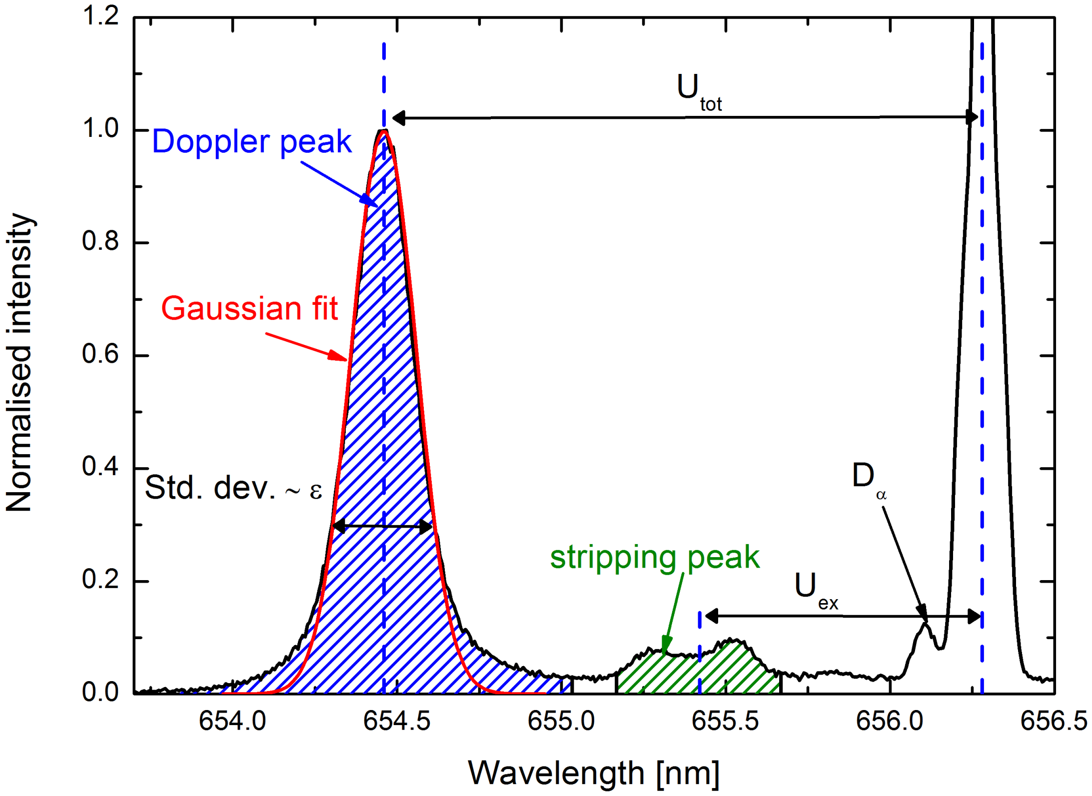

Figure 3.9: *Example of a BES spectrum obtained at BATMAN for hydrogen with* $U_{\mathrm{tot}} = 21.9\,kV$*,* $U_{\mathrm{ex}} = 4.7\,kV$ *and* $p_{\mathrm{source}} = 0.9\,Pa$*. The divergence* ϵ *is proportional to the standard deviation of the Gaussian fit.*

remaining deuterium gas in the tank from former deuterium operation.

On the left side at around 654.5 nm the main Doppler peak is located. Fully accelerated radiating hydrogen atoms lead to the formation of this peak. The peak shape and width is determined by the angular distribution of the fast beam particles.

Between the unshifted H_α and the Doppler shifted peak, the stripping peak appears at around 655.4 nm. As mentioned previously, stripping comes from collisional destruction of negative ions in the extraction system. Thus stripped particles are not fully accelerated, which affects the Doppler shift. This means the wavelength of the radiated photons is closer to the unshifted H_α peak than the fully Doppler shifted peak. The wavelength of the photons from stripped particles can be between the H_α wavelength and the wavelength at the maximum of the main Doppler shifted peak. The integral of the stripping peak is linked to the H_2 density in the extraction system. In the spectrum, the maximum of the stripping peak is always located around the wavelength which refers to the particle energy gained due to the extraction voltage. This indicates that the majority of stripped particles have their origin at the end of the first gap in the extraction system. Here, the H_2 density (which decreases from the source to the tank) is still high while the cross sections for the reactions (2.21) and (2.25) are around their maximum. Practically, the stripping peak is defined as a certain area around the wavelength refering to particles with an energy corresponding to the extraction voltage. This assumption considers the majority of the photons from stripped particles.

The integrated emissivity E of the three peaks (E_{H_α} for the unshifted H_α peak, E_D for the Doppler shifted peak and E_S for the stripping peak) can be described by an advanced corona model [102]. Thereby the excitation channels can be different for the sake of the species and the particle velocity:

$$
\begin{aligned}
E_{\mathrm{H}_\alpha} &= n_{\mathrm{H}_0}(v) n_{\mathrm{H}_2} \sigma_{0\alpha,\mathrm{Diss}} v \frac{A_{3,2}}{A_{3,1}+A_{3,2}}\,, && (3.2)\\
E_{\mathrm{D}} &= \left(n_{\mathrm{H}_0}(v_{\max})\sigma_{0\alpha} v_{\max} + n_{\mathrm{H}^-}(v_{\max})\sigma_{-1\alpha} v_{\max}\right) n_{\mathrm{H}_2} \frac{A_{3,2}}{A_{3,1}+A_{3,2}}\,, && (3.3)\\
E_{\mathrm{S}} &= \int_{v<v_{\max}} n_{\mathrm{H}_0}(v) n_{\mathrm{H}_2} \sigma_{0\alpha} v \frac{A_{3,2}}{A_{3,1}+A_{3,2}} \mathrm{d}v\,. && (3.4)
\end{aligned}
$$

v is the particle velocity, $v_{\max}$ denotes the maximum velocity that a particle can gain in the extraction system. $\sigma_{-1\alpha}$ is the cross section of reaction (2.25), $\sigma_{0\alpha}$ for reaction (2.26) and $\sigma_{0\alpha,\mathrm{Diss}}$ for reaction (2.27). $n_{\mathrm{H}_0}(v)$ is the density of the neutral beam particles, n_{H^-} is the negative ion density and n_{H_2} the density of the background gas. $A_{3,1}$ is the de-excitation probability coefficient for the de-excitation from the state 3 to the state 1 (Lyman-β-line) and $A_{3,2}$ from the state 3 to 2 (Balmer-α-line).

3.2.2 BES standard evaluation

The evaluation of a single BES spectrum allows the determination of the beam divergence and the stripping fraction averaged within the cone of the line-of-sight. In the following paragraph the *standard evaluation* will be explained, which has been used so far. In section 5.1.1.3 of this thesis, a better evaluation technique leading to a smaller evaluation error is developed.

In small sources the *standard evaluation* has been a valid technique [92, 103]. In order to determine the divergence, the part of the Doppler shifted peak with all values above a certain limit (typically 30%) of the maximum peak value (in order to avoid the influence of background noise) is fitted with a Gaussian fit. Another reason for the fit of the center part can be seen in figure 3.9. While the fit has a good agreement with the measurement in the center, a deviation at the edges is observed. This deviation is assumed to come from a halo, consisting of particles with a relatively large trajectory angle τ. Since this contribution is very small, the majority of the radiating beam particles (with a smaller angle τ) are from the core beamlet and generate the center part of the Doppler shifted peak.

From the standard deviation s_{Doppler} of the Gaussian fit, the divergence ϵ can be calculated [101]:

$$\epsilon = \frac{s_{\mathrm{Doppler}}}{|\lambda_0 - \lambda_{\mathrm{Doppler}}| \tan\theta} \tag{3.5}$$

However, first the standard deviation has to be corrected from the line broadening effects which are caused by the apparatus profile of the spectrometer and the broadening of the line-of-sight [101]. However this correction is almost negligible for the BES systems at BATMAN, MANITU and ELISE.

The stripping fraction f_{S} is defined by the ratio of the current density of the not fully accelerated particles (which are solely neutral hydrogen atoms) and the whole beam (consisting of neutrals and negative hydrogen ions) current density:

$$f_{\mathrm{S}} = \frac{j_{\mathrm{H}_0}(v < v_{\mathrm{max}})}{j_{\mathrm{H}_0}(v < v_{\mathrm{max}}) + (j_{\mathrm{H}_0}(v_{\mathrm{max}}) + j_{\mathrm{H}^-}(v_{\mathrm{max}}))}\,, \tag{3.6}$$

where j_{H_0} is the current density of H_0 and j_{H^-} of H^-. The emissivity of the emitted H_α light is proportional to the current density, which makes it possible to determine the stripping fraction from a BES spectrum.

$$\begin{aligned}
j_{\mathrm{H}_0}(v < v_{\mathrm{max}}) &\propto n_{\mathrm{H}_2} \frac{E_{\mathrm{S}}}{\sigma_{0\alpha}(v)} \mathrm{d}v\,, && (3.7)\\
j_{\mathrm{H}_0}(v_{\mathrm{max}}) &\propto n_{\mathrm{H}_2}(1 - f_{\mathrm{N}}) \frac{E_{\mathrm{D}}}{\sigma_{0\alpha}(v_{\mathrm{max}})}\,, && (3.8)\\
j_{\mathrm{H}^-}(v_{\mathrm{max}}) &\propto n_{\mathrm{H}_2} f_{\mathrm{N}} \frac{E_{\mathrm{D}}}{\sigma_{-1\alpha}(v_{\mathrm{max}})}\,. && (3.9)
\end{aligned}$$

f_{N} is the neutralisation degree and depends on the traveling distance of the negative ions in the extraction system and the density profile of the background gas in the tank. It is given by the ratio of the beam particle densities:

$$f_{\mathrm{N}} = \frac{n_{\mathrm{H}^-}(v_{\mathrm{max}})}{n_{\mathrm{H}^-}(v_{\mathrm{max}}) + n_{\mathrm{H}_0}(v_{\mathrm{max}})}\,. \tag{3.10}$$

For the evaluation an absolute calibration of the spectroscopic system is not needed. However for the integration of the peaks the integration limit has to be set manually, which can lead to a measurement error. This will be discussed in section 5.4. For the evaluation of the stripping fraction from the integrals of the Doppler shifted peak and the stripping peak the following assumptions are made in the standard evaluation: The Doppler shifted peak originates only from fully accelerated (mono-energetic) radiating particles. Its broadening is due to the trajectory angle distribution of the particles, i.e. the divergence of the beamlet. For the stripping peak, generated by the not fully accelerated radiating hydrogen atoms, the broadening comes from a convolution of the their angular distribution, which can be different from the one of the fully accelerated beam particles and of the distribution of the kinetic energy of the particles. Since the cross sections for excitation are almost constant in the energy range, the cross sections in equation (3.7) to (3.9) are replaced by an average cross section. Then equation (3.6) can be rewritten as:

$$f_{\mathrm{S}} = \frac{\frac{E_{\mathrm{S}}}{\sigma_{0\alpha,\mathrm{ave1}}}}{\frac{E_{\mathrm{S}}}{\sigma_{0\alpha,\mathrm{ave1}}} + \left((1-f_{\mathrm{N}})\frac{E_{\mathrm{D}}}{\sigma_{0\alpha,\mathrm{ave2}}} + f_{\mathrm{N}}\frac{E_{\mathrm{D}}}{\sigma_{-1\alpha,\mathrm{ave1}}}\right)} \tag{3.11}$$

The measured stripping fraction in the IPP prototype source determined by equation (3.11) is at least two times lower as the predicted value by models [92, 103] (see section 2.5.2.2). The reason for this may be due to the described assumptions for the stripping evaluation from BES spectra. Whether or not the described assumptions are reasonable will be investigated and discussed in chapter 5.4. Also, as already mentioned, the assumed density profile in the extraction system in the models, predicting the stripping losses, may need improvements. Section 5.4 will also help to improve the density profile which is used for modeling.

4 Modeling

4.1 State of the art

Up to now, various codes to model beamlet extraction, formation and acceleration in negative ion sources have been developed in different groups for different purposes, mainly concerning single beamlets [91, 104, 105, 106, 107, 108, 109, 110, 111]. The number of codes simulating large beams consisting of multiple beamlets is yet smaller. This chapter will give an overview of codes which are mainly used for beam and beamlet simulation in NBI ion sources for negative ions and demonstrate the necessity for the new code BBC-NI which was developped within this thesis. The field of activity and the method of operation of this code will be presented in the next section.

Most of the existing codes tackle only a single (mainly in ion sources for accelerators) or few beamlets. The treatment of a whole grid system in a negative ion source for NBI would need a high CPU performance, large memory requirement and a long calculation time, which is presently not feasible. Due to the limit of simulating only a part of the beamlets in negative NBI ion sources global beam physics aspects cannot be covered by the existing codes. The available codes mainly differ in the treatment of the plasma physics in the area upstream the extraction, the plasma to beam transition and the particles interactions in the extraction system. The majority are trajectory codes which have in common a self-consistent model only for the space charge calculation of the main ion species in the extraction system. This implies particle interaction from Coulomb forces between charged particles and electromagnetic forces from the presence of attendant fields. The transition from the source plasma to the ion beam cannot be described correctly by the trajectory codes. A fully self-consistent treatment of the beam formation can only be done with PIC (**P**article **I**n **C**ell [112]) codes, which are more complex and have long calculation times (at least several days on modern computers even when parallelised). Therefore PIC codes for beamlet simulation are rare with respect to trajectory codes. The optimal application of the codes is for single aperture small ion sources. However they are also used for multiple aperture large ion sources, e.g. in NBI. The existing codes treat their problem either in 2D or 3D geometry. Frequently used codes for simulating the beam formation and transport in large ion sources are introduced in the following.

4.1.1 2D Codes

2D codes principally have the disadvantage that they cannot take full 3D magnetic fields into account. However in the negative ion sources for ITER NBI a complex 3D magnetic field topology is present. Still some 2D codes come into operation:

SLACCAD (Stanford Linear Accelerator Code - CAD): This is a 2D axial symmetric trajectory code for a single beamlet which was modified from an earlier version for beamlet formation [104]. It does not include physical effects like magnetic fields or the space charge of co-extracted electrons. However, since the calculation is fast, it is still often used to calculate beam optics for ion sources.

NIGUN: It is a 2D simulation for a single beamlet of negative ions. It is also a trajectory code. NIGUN has an enhanced model of the plasma sheath at the extraction [105]. It can take also positive ion species like Cs^+ into account.

4.1.2 3D Codes

KOBRA3-INP[11]: The code is capable of a 3D calculation of a negative ion beam [106]. It is a ray tracing code solving the Poisson equation self-consistently. However, the plasma conditions at the extraction are assumed by a simple charge compensation model. But with KOBRA3-INP it is possible to take an inhomogeneous current distribution at the meniscus into account. This has been done in this thesis. KOBRA3-INP is able to simulate a single, but also a few beamlets.

BYPO: This code is also able to do 3D beamlet modelling [107, 108, 109]. Additionally it has a more sophisticated plasma module compared to the other codes. With its help, the self-consistent description of the meniscus is done

---

[11] INP - Ingenieurbüro für Naturwissenschaft und Programmentwicklung, Junkerstraße 99, 65205 Wiesbaden

by implementing plasma physics features. This leads to a more realistic treatment of the extraction region.

Opera-3D[12]: This is a commercial code, which is mainly used to investigate magnetic field configurations and stripping losses [108]. It is also able to simulate several beamlets in one calculation in order to investigate the beamlet-beamlet interaction.

There are three other 3D codes, which are particularly dealing with special physical issues of negative ion beams for fusion applications:

EAMCC (Electrostatic Accelerator Monte Carlo Code): This code models the transmission of the beam as well as the production of secondary particles in the accelerator [91] in order to calculate the flux of backstreaming positive ions. The electric field is usually imported from previous calculations with SLACCAD while the magnetic field comes from Opera-3D. Interactions of the beam particles with the background gas and the surfaces of the electrodes are calculated with the help of a Monte Carlo module. This provides information on stripped particles and secondary electrons within the extraction system. Additionally the heat load on the electrodes can be obtained.

dBES: This analytic code is currently developed at Consorzio RFX in Padua and it simulates BES spectra. For this approach, the angle and energy distribution of the beam particles at the grounded grid is needed as input parameter. By solving a complex bundle of vector equations the spectra for various BES line-of-sights can be calculated. The main purpose of the code is to optimise the line-of-sight geometry for NBI systems equipped with a BES diagnostic tool [110].

ONIX (Orsay Negative Ion eXtraction): The code is a self-consistent parallelised full 3D particle-in-cell Monte Carlo collision code [111, 113]. A major problem of the codes presented so far is the lack of a self consistent model (plasma and beam). Beside dBES all codes are trajectory codes which have a more or less simple module in order to describe the plasma conditions before the extraction and the meniscus formation.

---

[12] Opera 3D design software, Cobham group, http://www.cobham.com/about-cobham/aerospace-and-security/about-us/antenna-systems/specialist-technical-services-and-software/products-and-services/design-simulation-software/opera/opera-3d.aspx

> The domain box of ONIX presently has a range of 20×20 mm in horizontal and vertical direction and 25 mm along the beam axis. The region of interest is one plasma grid aperture. This includes the formation of the plasma sheath upstream the plasma grid and also the extraction at the meniscus and in the first gap. One task of the code is to calculate the beam formation at the plasma grid aperture. Due to the long calculation time (several weeks), it is only possible to simulate a single aperture at the moment.

OPERA and KOBRA3-INP are able to simulate several beamlets. But the simulation of a large beam from several hundred apertures in a reasonable calculation time is not possible. With dBES, BES spectra can be simulated but not the associated power density profile deposited by the beam on the calorimeter or the power loads on the grids of the extraction system. Hence, in order to simulate the whole beam of a hydrogen ion source for ITER NBI, with all the beam line diagnostics included, a new code, the BBC-NI code, is necessary.

4.2 Bavarian Beam Code for Negative Ions (BBC-NI)

BBC-NI is capable of simulating the whole beam from a large ITER relevant ion source, i.e. from the plasma grid to the calorimeter. BBC-NI is a full 3D trajectory code. Its beam simulation includes all power loads at the relevant beamline components, grid currents and BES spectra from existing lines-of-sight in the experiment. This forward calculation of BES spectra is a new feature in the beam simulation. This thesis will show that BBC-NI is an indispensable instrument to determine more preciscly the beam parameters from beam diagnostic measurements, in particular from BES.

However, as it will be shown, to determine the beam parameters in large negative ion sources for ITER, the full set of beam diagnostics (calorimeter, thermocouples, BES) as well as beam modeling are necessary (see chapter 5.1.2 and 5.2).

4.2.1 Transport

BBC-NI is a trajectory code for the extracted negative ions and the products of their collision reactions as it can be seen in the equations (2.21) - (2.27). The reactions implemented in the code are explained in the second part of this chapter.

The code calculates the trajectory independently for each particle from the initialisation till the end when it hits a wall. The number of treated particles is usually in the range of $1 \cdot 10^8$ to $1 \cdot 10^9$ depending on the calculation time. The calculation is done by solving the equation of motion with a time step based numerical integration method, the modified midpoint rule invented by Gragg [114], which is an advanced application of the explicit Euler method. The temporal step size ($10^{-19} - 10^{-9}\,$s) is controlled by a step size control module. It considers the domain size of a electric or magnetic field map. In order to acquire the whole information from the field map, the temporal step size has to be smaller than the domain size of the fields divided by the particle velocity. For minimising the calculation time, the step size control module increases the step size as far as possible while still considering the restrictions related to the domain size and the particle velocity. The step size control module strongly decreases the calculation time when no electric and magnetic field map has to be taken into account (for beam simulations starting at the grounded grid), since then only the geometric boundary conditions of the beam line limit the increase of the temporal step size.

A particle at the position $\vec{r}$ with mass m and charge q is treated by the Lorentz force due to the presence of the magnetic field $\vec{B}(\vec{r})$ and the electric field $\vec{E}(\vec{r})$. The force $\vec{F}(\vec{r},\vec{v})$ is calculated by the relativistic Lorentz equation since the particles have a high energy, which corresponds to high velocity v, especially for the electrons:

$$\vec{F}(\vec{r},\vec{v}) = q\gamma(\vec{E}(\vec{r}) + \vec{v} \times \vec{B}(\vec{r}))\,, \tag{4.1}$$

with the Lorentz factor

$$\gamma = \sqrt{1 - \left(\frac{v}{c}\right)^2}\,. \tag{4.2}$$

The determination of the electric and magnetic field at a given position is done by a 3D interpolation. The spatial step size (calculated from the temporal step size and the actual particle velocity) for each particle has to be at least as small as the grid sizes of the implemented field maps.

For each time step a wall-collision module checks the position of the particle for a possible hit on implemented surfaces, i.e. grids, scrapers or the calorimeter. In case of such an event, the next particle is launched.

4.2.2 Collisions

BBC-NI considers all necessary collisions of the beam particles (H^-,H_0) with the background gas. They were described by the reactions (2.21) - (2.27) on page 43. The probability for a collision reaction within a time step Δt in the time interval $t_{k-1} \leq t \leq t_k$ is given by [112]:

$$P(t_k) = 1 - \exp\left(-v(t_k)\Delta t n_{\mathrm{H}_2}\sigma[v(t_k)]\right) , \tag{4.3}$$

where n_{H_2} is the background density and σ is the cross section. For the sake of simplicity the equation is approximated with

$$P(t_k) = \Delta x n_{\mathrm{H}_2}\sigma + O[(\Delta x)^2] . \tag{4.4}$$

$O[(\Delta x)^2]$ is the order of the error, which tends to be zero for small Δx (which is the case in BBC-NI), and $\Delta x = v(t_k)\Delta t$. The H_2 density in the extraction system and drift region is calculated from the pressure and the temperature. They are input parameters and interpolated from a 1D line profile along the beam axis. The value of a cross section for a certain energy is derived from a fit of the available data points. For H^- double stripping, H_0 excitation and dissociative excitation the fit is a Chebyshev polynomial [115]. For H^- stripping, H_0 and H_2 ionisation the fit is an individual fit function from [89]. The data points from the cross section values from H^- excitation are fitted with a Cubic polynomial.

A Monte Carlo module generates a normal distributed random number $\mathrm{z} \in (0, 1)$ which is used to decide whether a reaction takes place. This is the case for

$$\mathrm{z} \leq P(t_k) . \tag{4.5}$$

When additional particles are created, e.g. electrons in stripping reactions, their trajectories are taken into account and calculated as well. Their direction of flight at their creation point is equal to the original particles. This assumption is reasonable due to the high energies and the low velocities perpendicular to the beamlet axis of the beam particles.

4.2.3 Photon emission

If a reaction leading to an excited hydrogen atom takes place, the photon-emission-module, which is a special feature of BBC-NI, is executed and generates a BES spectrum. This task can be separated into two parts. First solving a geometric problem and secondly solving a spectroscopy problem when creating a spectrum. The geometric task checks whether the treated particle is within a line-of-sight. If this is the case, the spectroscopy part generates a photon and calculates the spectral detection:

Geometric module: BBC-NI checks if the currently treated particle, i.e. the excited hydrogen atom, is within a line-of-sight. This is done by solving a 3D analytic vector equation. If the particle is within a line-of-sight, the code generates a photon as it will be explained in the next subsection. For the sake of simplicity the H_0 excitation and de-excitation are simulated at the same time step although some time passes between that two processes. The error from this method is rather small. The Einstein coefficient for a hydrogen molecule de-excited from the main quantum number $n = 3$ to $n = 2$ is $4.4 \cdot 10^7\,\mathrm{s}^{-1}$. Hence the traveling distance for excited particles with a typical kinetic energy in the described IPP ion sources is in the range of centimeters. This is comparable to the spatial dimensions of the line-of-sight.

Spectroscopic module: If a radiating hydrogen atom is within the line-of-sight, the next step for detecting H_α radiation in the BBC-NI code is the photon field generation. If an excited hydrogen atom would emit only one photon as it is the case in reality, the number of photons hitting the detector simulated by BBC-NI would be almost zero. The reason is due to the total number of calculated particles ($10^5 - 10^8$) which is limited by the CPU time, the excitation probability (< 0.1‰) and the isotropic radiation. In BBC-NI a excited hydrogen atom is assumed to have a photon field which practically exists out of many "mini"-photons (mγ). They differ in polar and azimuthal angles. This method is a numerical approach. The number of mγ, $N_{\mathrm{m}\gamma}$, is set individually (usually in the range of $1 \cdot 10^6$) by defining the step size for the two angles:

$$N_{\mathrm{m}\gamma} = \frac{(360°)^2}{\Delta a_{\mathrm{azimuth}} \cdot \Delta a_{\mathrm{polar}}}\,. \tag{4.6}$$

$\Delta a_{\mathrm{azimuth}}$ and $\Delta a_{\mathrm{polar}}$ are the azimuthal and polar step sizes. The emissivity $E_{\mathrm{m}\gamma}$ of all mγ is then normalised to 1:

$$1 = \sum_{i=1}^{N_{\mathrm{m}\gamma}} E_{\mathrm{m}\gamma}(i)\,. \tag{4.7}$$

The module checks by a vector equation for every single virtual mγ whether it hits the detector at the end of the line-of-sight or not. This is done by determining the intersection of the detector surface with the propagation vector of the single mγ. In the case of a solution for this equation, the wavelength spectrum of the single mγ is distributed as a Gaussian peak with the standard deviation determined by natural line broadening effects. The extent of line broadening is an input parameter coming from the spectrometer. The wavelength position of the Gaussian peak is determined self-consistently by the Doppler shift due to the H_0 velocity vector and the propagation vector of the single mγ.

Finally, the sum of the spectra from all detected mγ is the spectrum of the photon field emitted from one hydrogen atom. The emissivity of the photon field $E_{\gamma\mathrm{field}}$ is calculated by:

$$E_{\gamma\mathrm{field}} = N_{\mathrm{m}\gamma,\mathrm{detected}} \cdot E_{\mathrm{m}\gamma} \,. \tag{4.8}$$

Finally, the sum of the spectra from all photon fields from all excited hydrogen atoms leads to the simulated BES spectrum.
Additionally, BBC-NI creates a protocol with detailed information for all radiating hydrogen atoms contributing to a BES spectrum for a given line-of-sight. This data sheet contains the position and velocity components at the de-excitation, the wavelength of the maximum emissivity of the respective photon field, the trajectory angle τ and the aperture number where the particle started.

4.2.4 Starting conditions and application

BBC-NI has two operational modes depending on the starting conditions of the negative hydrogen ions:

BBC-NI Advanced

The advanced mode of BBC-NI starts the particles upstream of the plasma grid and takes the whole acceleration phase of the negative ions into account. Since all major beam effects are considered, i.e. acceleration within the electric field, magnetic field deflection, heavy particle collisions, it is possible to simulate the whole beam and an entire BES spectrum, including the part coming from stripped particles. This allows the beamlet reconstruction within the extraction system. In this region, no measurements of the background gas density or the electric field map with diagnostics are possible. However these parameters are crucial for the beamlet shape, the stripping and grid losses (see chapter 2.5.2) and have to be provided by other codes.

The electric field map is an essential input for the advanced mode. Since BBC-NI has no solver for the Poisson equation and does not consider particle interaction the field map has to be calculated separately. Within this thesis, the commercial code KOBRA3-INP is used. Also the starting conditions of the particles (starting coordinate, starting velocity vector) for the trajectories in BBC-NI are taken from KOBRA3-INP.

Due to the calculation time (several hours), KOBRA3-INP (see section 4.1.2) is used for calculating the electric field of the extraction system for only one aperture. BBC-NI takes this 3D electric field map and applies it for all apertures.

BBC-NI Simple

The simple mode of BBC-NI sets the particle start at the grounded grid of the extraction system taking only the fully accelerated negative ions into account. Applying an electric field would force the temporal step size control to small steps in the range of the electric field mesh grid size, which increases the calculation time for each single particle. Since the calculation with BBC-NI Simple starts after the acceleration phase, no electric field is needed. Due to the absence of this field, the temporal step size can be increased and much more overall particles are taken into account. This leads to more generated photons and better statistics for the compilation of the BES spectra. The calculation time for this application mode (less than one day) is decreased by an order of magnitude compared to BBC-NI Advanced. However, only the Doppler shifted peak and the unshifted H_α peak are simulated.

In order to keep the starting conditions simple, the particles start in the centre of the apertures with a normalised velocity vector, perpendicular to the grid surface. This vector can then be transformed by various rotations setting the start conditions as shown in figure 4.1. First the start velocity vector is rotated around a polar angle β_p and an azimuthal angle β_a. This approximation respects possible steering effects which can occur in the extraction system and have to be considered as input parameters.

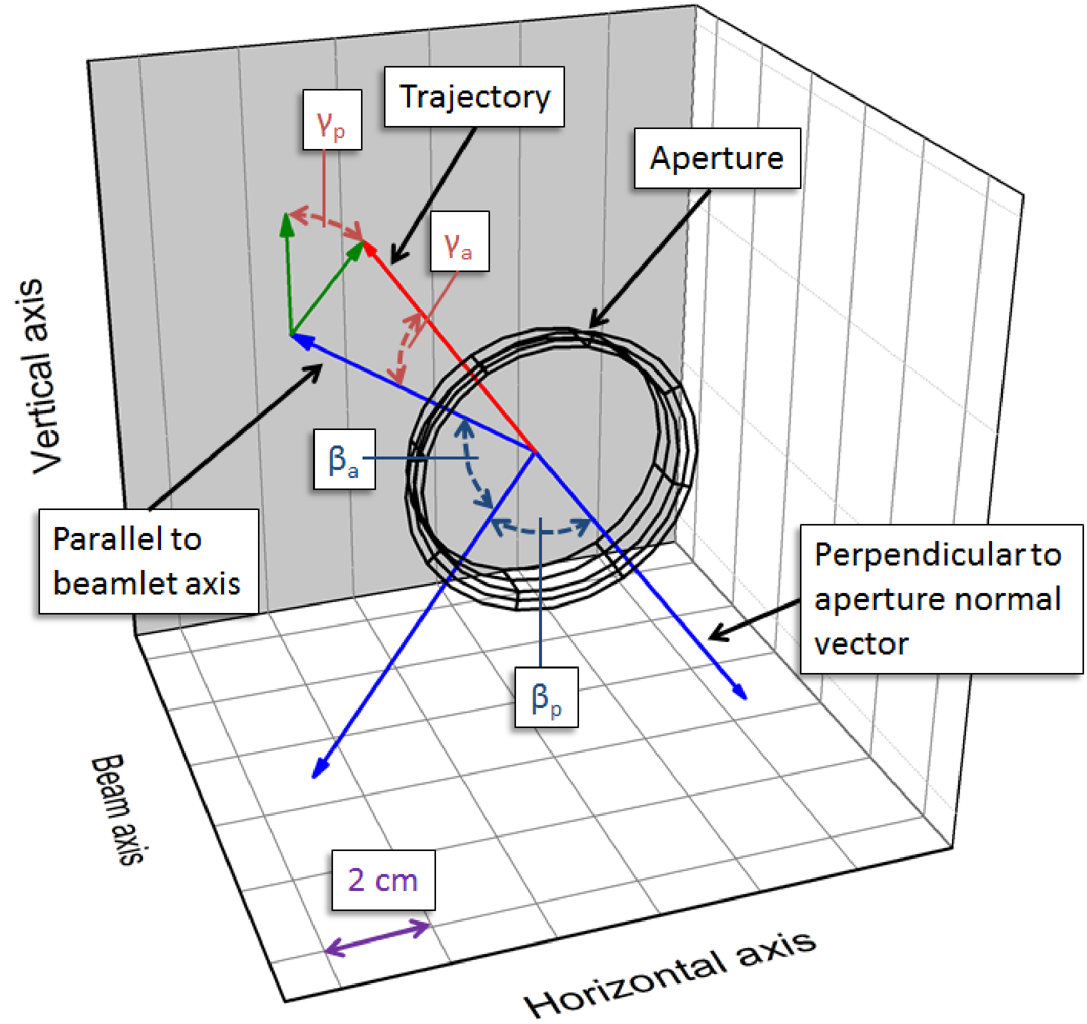

Figure 4.1: *Angles for the starting velocity vector in BBC-NI Simple.*

Afterwards the vector is then rotated by an azimuthal angle γ_a which is distributed with a Gaussian probability and a normally distributed polar angle γ_p. Thereby the standard deviation of the Gaussian distribution is determined by the divergence ϵ which is an input parameter. γ_a is calculated numerically by the following equation while the equation for γ_p is solved analytically:

$$\gamma_\mathrm{a} = \sqrt{2}\epsilon\,\mathrm{erf}^{-1}(\mathrm{z}_1)\,, \tag{4.9}$$

$$\gamma_\mathrm{p} = 2\pi\,\mathrm{z}_2\,. \tag{4.10}$$

z_1 and z_2 are two normally distributed random numbers.

Hence in this thesis BBC-NI Advanced is used only when beamlet formation or stripping is important. BBC-NI Simple is used to get a better understanding of the formation of the main Doppler shifted peak in a BES spectrum. Furthermore BBC-NI Simple is suitable to study inhomogeneous distributions of the accelerated current density (see chapter 2.5.2).

4.3 Support codes

BBC-NI needs several input parameters, which have to be delivered by other codes:

- The electric field in the extraction system.
- The magnetic field in the extraction system.
- The starting coordinates and velocities of the particles.
- The H_2 density profile in the extraction system.

Their generation is explained in the following sections.

4.3.1 Electric field

The electric field in the extraction system is complicated because the vacuum field from the extraction electrodes is changed by the influence of the charged beam particles. As already mentioned, the electric field map in the extraction system is calculated by the commercial code KOBRA3-INP, which is available at IPP Garching. The calculation domain is limited to one extraction aperture to keep the calculation time in an acceptable setting. The number of particles which can be calculated in a reasonable time (several hours) is up to $100,000$.

With KOBRA3-INP various starting conditions for the extracted particles can be defined. The common case is a laminar flow of the negative ions towards the meniscus. For positive ions this is a valid assumption and easy to implement. As mentioned in chapter 2.5.1 the aperture illumination for negative ions, however, might not be homogeneous. For this case, one can implement starting conditions, which means the coordinate and starting velocity of each treated particle. This was also done in this thesis.

4.3.2 Magnetic field

The magnetic field maps are generated by the code PerMag [116] for permanent magnets and with the commercial finite element analysis software ANSYS [117] for magnetic fields generated by a current.

Since the magnetic fields at the ion source at BATMAN are solely generated by permanent magnets, PerMag is used in order to calculate the magnetic field map for BBC-NI calculations.

At ELISE, the magnetic filter field is generated by a current through the plasma grid (see section 2.4.4). For this reason the magnetic field of ELISE for BBC-NI is calculated by PerMag, considering the magnetic field from the electron deflection magnets, and ANSYS, considering the filter field.

4.3.3 Starting conditions at the meniscus and density profile

Usually, for the sake of simplicity, in calculations on the beamlet formation, a laminar flow of the negative ions to the meniscus is assumed. As already mentioned in section 2.5.2.1, an inhomogeneous aperture illumination, i.e. an asymmetric H^- density distribution at the meniscus might be more realistic.

To get this aperture illumination of the extracted negative ions, the transport to the meniscus was calculated by the IPP code TrajAn [70].

It delivers for each aperture the particle coordinates of the extracted negative ions at the meniscus including the velocity distribution in horizontal,vertical direction and along the beam axis. Thereby, the number of particles per aperture can be over $100,000$, which is enough for KOBRA3-INP calculations.

As an input parameter, TrajAn needs the form of the meniscus. This parameter is first calculated with KOBRA3-INP assuming a laminar flow of negative ions to the extraction aperture. This approach leads to a small error on the meniscus shape and elongation, however it is the best possible procedure which is available up to now.

Finally, a density profile for the BBC-NI Advanced mode has to be provided. This profile is calculated by a simple Excel program called Excelstrip. The basic assumptions of this model are given in chapter 5.4.

4.3.4 Summary

In summary, a sketch of the working principle of BBC-NI is shown in figure 4.2. In the center of figure 4.2 is the BBC-NI box including the work space of the code. Above this box, the input layer (1) describes the necessary input parameters. Either they have to be defined by the code operator, like the geometry of the grid

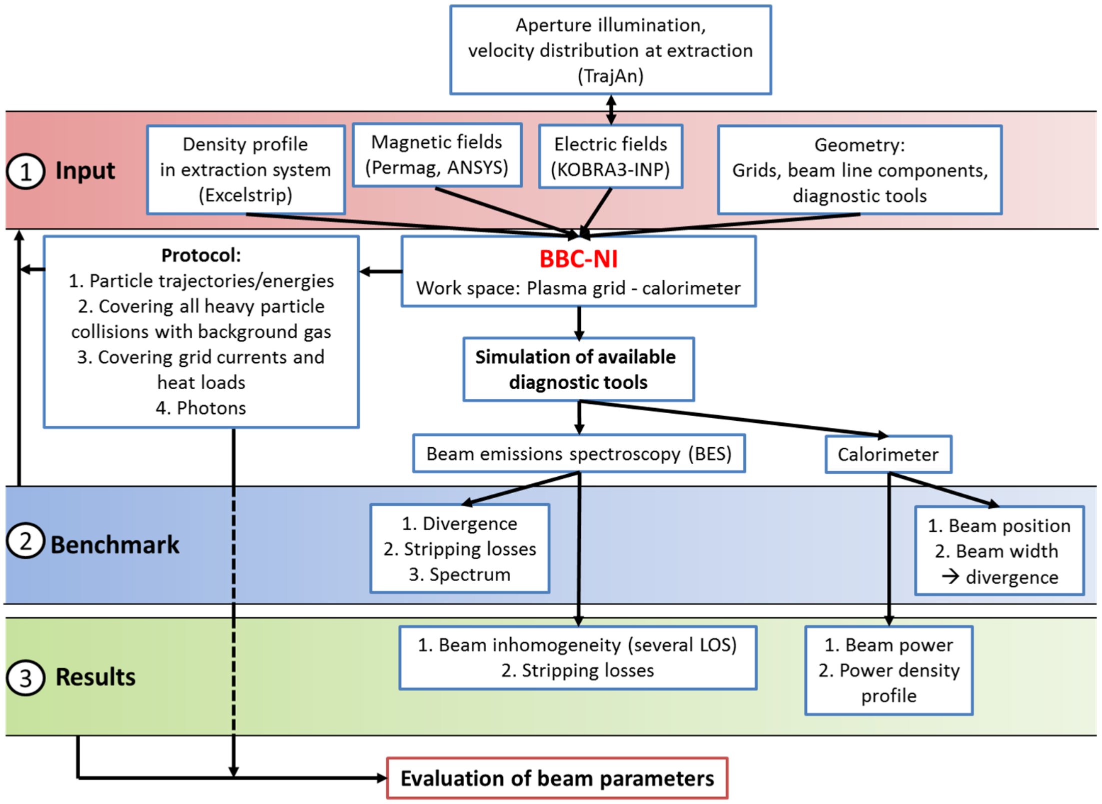

Figure 4.2: *Sketch of the working principle of BBC-NI.*

system or the beam line, or the input parameters can come from calculations from other codes. This applies for the density profile in the extraction system and the magnetic and electric fields.

BBC-NI is then able to simulate the beam including all available diagnostic tools. In a first step, which is indicated by the benchmark layer (2), the code has been benchmarked by the help of various protocols containing relevant information on particle properties. The input parameters have been adjusted during this benchmark in order to increase the precision of the BBC-NI calculation. With the protocol data from the code the BES evaluation has been improved within the scope of this thesis. This will be shown in the next chapter (see sections 5.1 and 5.1.2).

Finally, the code can the be used to do simulations of ion beams. The obtained results (3) are then compared with real measurements. A successful simulation can help to determine the beam properties from the measurements of beam diagnostic tools at large negative ion sources.This of importance for the ITER NBI source. A first investigation on the determination of the beam properties, concerning the beam inhomogeneity at ELISE and the stripping losses at BATMAN from BES calculations, has been done in this thesis (see section 5.2 and 5.4).

5 Results

5.1 BES spectra evaluation

As already mentioned in chapter 3.2, beam emission spectroscopy can be used to determine beam parameters, which are mainly the average beamlet divergence and stripping. Since the divergence of one beamlet is linked to its extracted current density, the beam inhomogeneity, i.e. the inhomogeneity of the current density distribution at the extraction, could be determined by measuring the spatial divergence distribution of the beam. This measurement is done with a line-of-sight array (see section 3.2).

This chapter will clarify the origin of the light emitting particles contributing to the spectrum. It will answer the question if the BES measurement of one line-of-sight collects information on the whole beam, part of the beam or only from several beamlets. Furthermore, this chapter will analyse the shape of a BES spectrum, in particular the Doppler shifted peak. Only by understanding the effects leading to the form of the peak, a correct evaluation of the divergence and therefore also the beam inhomogeneity is possible.

In a first step, BBC-NI Simple was used for simulations of the small beam at BATMAN, as here the locality of the measurement, i.e. a small amount of beamlet contributions to a spectrum of a single line-of-sight, is assumed to be much better maintained due to the small size compared to ELISE. Hence the underlying effects leading to the shape of the Doppler shifted peak can be better identified. With that knowledge, BBC-NI Simple simulations of the large beam at ELISE were performed, showing a higher complexity.

5.1.1 Small NBI ion sources

5.1.1.1 Benchmark at BATMAN

BBC-NI was benchmarked in a first step with BES measurements obtained at the testbed BATMAN. The ion source with a low number of apertures (126) and the

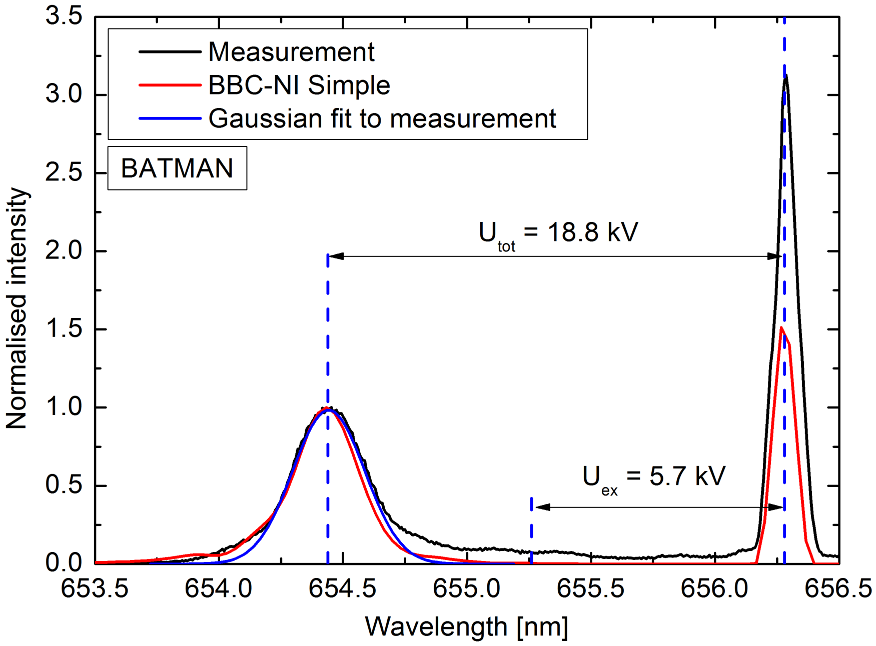

Figure 5.1: *Comparison of a simulation (BBC-NI Simple) and a measured BES spectrum at BATMAN. Additionally a Gaussian fit of the full Doppler shifted peak is shown. Indicated by the dotted lines are the Doppler shifts referring to the energies obtained by the extraction respectively the total voltage. The source filling pressure was 0.58 Pa and the normalised perveance was 0.12.*

diagnostic tools were already described in chapter 2.4.3. This first benchmark was done with BBC-NI Simple, since with BBC-NI Advanced it is not possible to reconstruct a BES spectrum properly. This is due to the electric field, calculated with KOBRA3-INP. The calculated electric field does not reflect reality as it will be explained in section 5.3.

Figure 5.1 shows the comparison of a measured BES spectrum with a simulation from BBC-NI Simple. The focus for this benchmark was to pattern the unshifted H_α peak and the Doppler shifted peak with the simulation in the best possible way. A stripping peak does not appear in the simulation because BBC-NI Simple simulates only the beam after the grounded grid. Since the trajectory angle distribution of the particles in the simulation is Gaussian (see section 4.2.4), a main Doppler shifted peak with a Gaussian shape is expected. This chapter will show that this prediction is not the case in general.

The calculated spectrum fits the measured one quite well. Looking at the unshifted H_α peak of the simulation it can be seen, that the simulation underestimates the emissivity at this wavelength. This is due to reflections of the plasma light of the source contributing to the spectrum. This contribution is not taken into account within the BBC-NI Simple simulation.

For the Doppler shifted peak the left side of the peak fits very good to the measurement (The terms "left" and "right" side is only valid for this case of a blue shifted spectrum). It can be seen that the shape of the simulated Doppler peak is not fully Gaussian. The reason for the small deviation at the left edge comes from statistical effects as discussed in the next section. The shape of the right side from the simulated Doppler shifted peak shows also a good accordance with the measurement. But the decrease of the calculated Doppler shifted peak happens at a slightly smaller wavelength. This gap occurs due to photons, emitted from hydrogen atoms which had a stripping reaction at high energies. A detailed analysis on the stripping contribution will be given in section 5.4. From the gap it can be seen that the part of the measured spectrum generated by photons from stripped particles is much larger than it was taken into account with standard evaluation of the BES spectrum.

The fact of a very good reproduction of the left side of the Doppler shifted peak with the BBC-NI Simple simulation makes the presence of a halo or a non-Gaussian beamlet shape (see section 2.5.2.2), i.e. a large fraction of particles with a high trajectory angle caused by other unidentified effects, unlikely. In fact, the shape of the peak has its origin in geometric effects like the area- and angle-effect and the origin-effect (see next section). The deconvolution of these effects, on the basis of this benchmark, is now done in the following section. The underlying spectrum and BBC-NI Simple results for the deconvolution are always taken from the benchmark shown in figure 5.1.

5.1.1.2 Shape effects

Area- and angle-effect

As mentioned in chapter 4.2.3 photons contributing to one BES spectrum are emitted by excited hydrogen atoms within the given line-of-sight. The wavelength of the photon is determined by the trajectory angle τ of the radiating hydrogen atom in the plane of the line-of-sight and the beam axis.

BBC-NI records for every detected photon (consisting of many mγ) the peak wavelength and the trajectory angle from the emitting hydrogen atom (see 4.2.3).

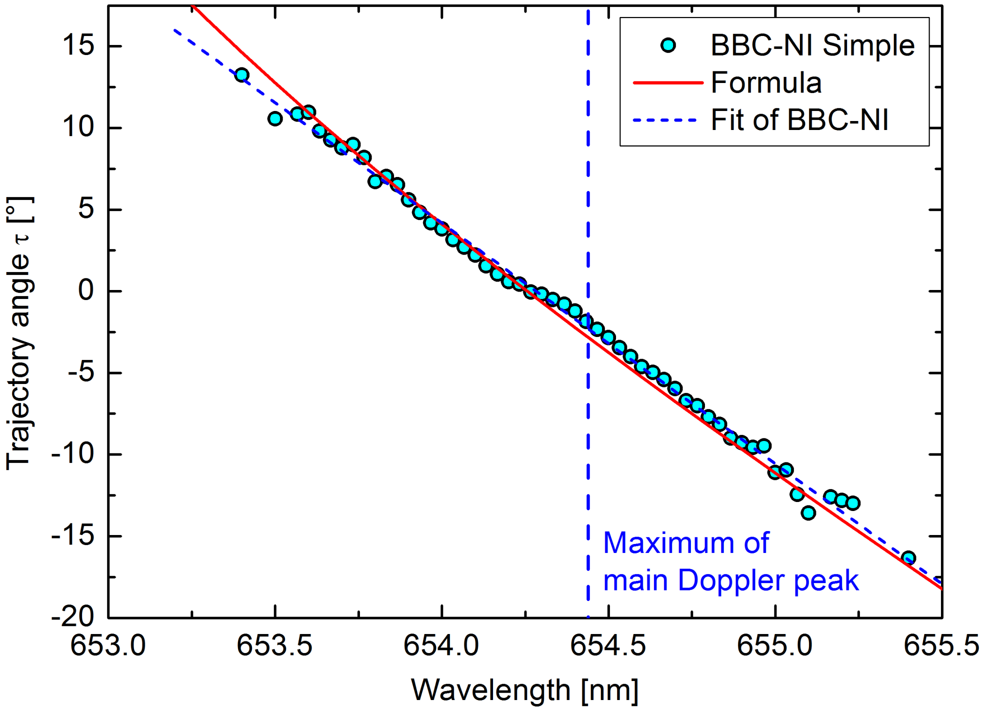

Figure 5.2: *Correlation between trajectory angle τ of radiating particles and the respective photon wavelength at BATMAN. Indicated by the blue dotted line is the position of the maximum of the full Doppler shifted peak.*

For a certain wavelength, several emitting H_0 can contribute to the spectrum. In the protocol the trajectory angles of all particles, radiating photons in a specific small wavelength range, a so-called bin which can be set individually as an input parameter (in this case 33 pm), are averaged.

Figure 5.2 shows the correlation between the wavelength and the trajectory angle τ for photons generated in BBC-NI Simple and as a comparison the correlation according to equation (3.1) describing the connection of the wavelength from a photon emitted by a particle having no velocity components in vertical but only in horizontal direction. The formula and the calculated result from BBC-NI Simple show a very good agreement. This means that the shape of the BES spectrum is determined by the trajectory angles and the observation angle θ.

Figure 5.3 helps to explain the small statistical deviation of the simulation from the measurement at the left edge of the Doppler shifted peak. The figure shows the correlation of the average emissivity with the wavelength. As noted in 4.2.3 every radiating particle contributes to the spectrum by a photon field with a specific emissivity. For every wavelength bin the emissivity of all photons is averaged and

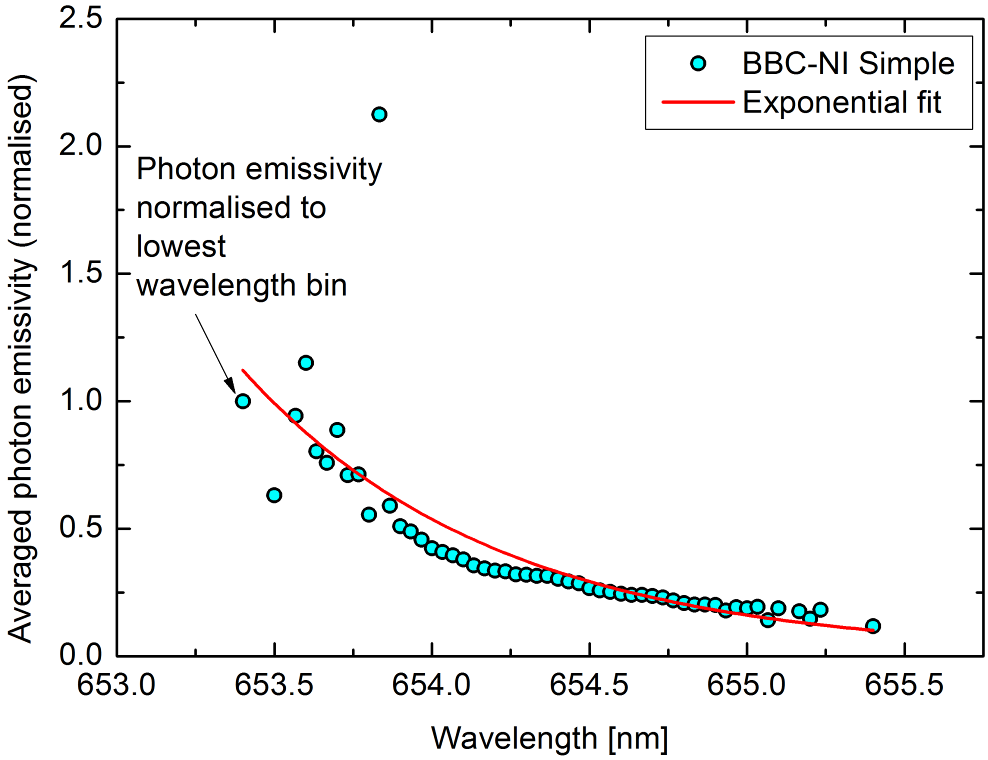

Figure 5.3: *Averaged photon emissivity for a certain wavelength range.*

normalised to the averaged emissivity of the photons at the lowest wavelength. The average emissivity decreases with increasing wavelength. As shown in figure 5.2 a shift to a high wavelength predominantly stands for a negative trajectory angle τ of the emitting hydrogen atoms. These particles are therefore usually emitting in greater distance from the optic head than the hydrogen atoms with a positive trajectory angle.

The area- and angle-effect determine the detected emissivity from a radiating particle (see chapter 3.2) and the emissivity therefore depends on the position of the radiating particle with respect to the line-of-sight. Figure 5.3 shows that the angle-effect is dominant and leads to a non-symmetric shape of the Doppler peak. Otherwise, the emissivity would increase with a lower wavelength.

However, there are strong outlier at low wavelengths. Photons with a low wavelength can be emitted from particles at a position very close to the optic head. In this region the emissivity of a photon is very sensitive to the particle position, because a slight change in the position leads to a strong change of the solid angle. It determines the number of mγ (see section 4.2.3) which are detected in the simulation. On the other hand, the probability of the presence of an emitting particle at this position is very low since the trajectory angle is Gaussian distributed. Hence only few photons from these particles are contributing to the spectrum, however their emissivity is comparatively high. Since the low calculation time (≈ 12h) is responsible for a low amount of radiating particles with a large trajectory angle τ, the angle-effect leads to statistical deviations at low wavelengths in BBC-NI Simple calculations. This error can be in principle reduced by increasing the calculation time. The presented results are from calculations where a compromise between feasibility and error minimisations was chosen. The effect of statistical deviations has been already seen in figure 5.1. Additionally the effect also adds to the form of the Doppler shifted peak a left-handed asymmetry.

Origin-effect

The angle-effect explains only partially the deviation of the Doppler shifted peak from an expected Gaussian form. Another deviation comes from the fact that several beamlets contribute to the spectrum from a line-of-sight, but with different parts of the trajectory angle distribution.

Figure 5.4 shows the frequency counts of the radiating particles separated by their trajectory angle, which contribute to the calculated spectrum in figure 5.1. Additionally, two fits are shown, a Gaussian fit and a Lorentzian fit. The Gauss curve $G(x)$ is described by the equation

$$G(x) = A \cdot exp\left(-0.5\left(\frac{x-\eta}{s}\right)^2\right) , \tag{5.1}$$

where x is the free parameter (in this case the trajectory angle τ), η is the center of the peak and s is the standard deviation. The Lorentz curve $L(x)$ is described by

$$L(x) = y_0 + \left(\frac{2A}{\pi}\right)\left(\frac{w}{(4(x-\eta)^2 + w^2)}\right) \tag{5.2}$$

y_0 is the offset, A is a dimensionless parameter, η is the center of the peak and w is the width. As already mentioned, a Gaussian shape of the frequency counts would be expected due to the starting conditions of BBC-NI Simple. Again as in the real spectrum, the Gaussian fit does not describe the form of the frequency

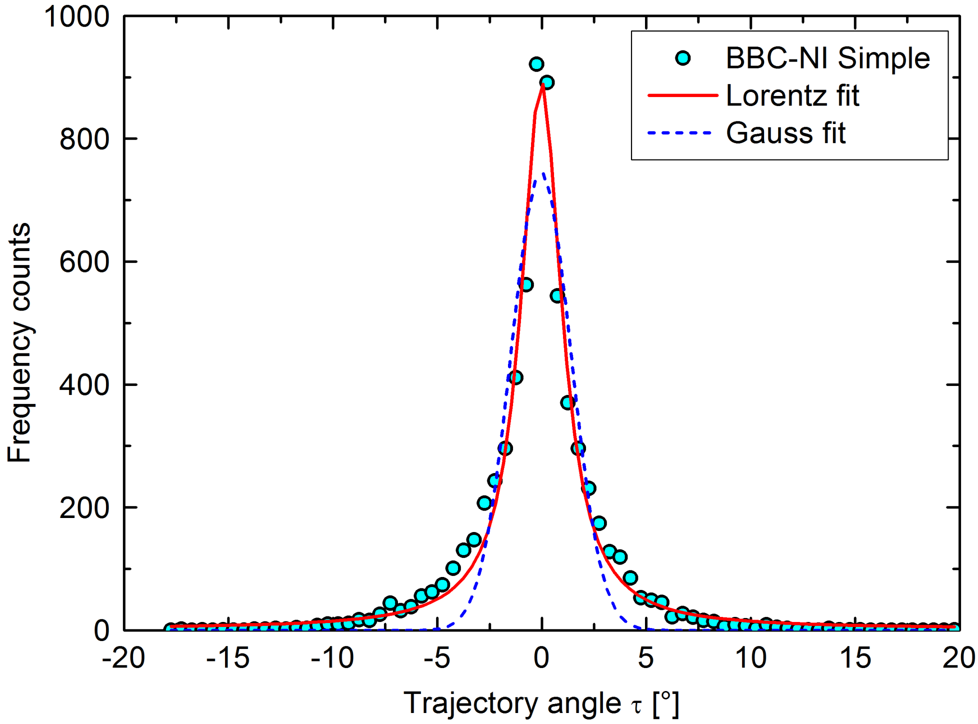

Figure 5.4: *Photon frequency counts with respect to horizontal angle of the light emitting particles.*

counts. On the contrary the Lorentz fit does much better reproduce the form. However, whether it is already the most appropriate function is not approved yet. Still, the standard evaluation can be improved, which will be shown in section 5.1.1.3.

The findings already show that the trajectory angle distribution of the radiating particles, contributing to one spectrum, is not necessarily Gaussian, although the distribution of the trajectory angles of the velocity vector for all particles is Gaussian.

This effect can be explained by the fact that a BES spectrum contains photons from radiating particles from several beamlets. Figure 5.5 shows on the left side the grid pattern of the grounded grid at BATMAN. The 126 apertures are aligned in 12 aperture rows. Additionally, the vertical dimension of the considered line-of-sight is projected on the pattern. As already introduced in chapter 3.2 the line-of-sight is located around 1.5 m downstream the grounded grid with a observation angle of 153°. The right side of figure 5.5 shows the part of radiating particles contributing to the LOS in percentage referred to their origin. It can be seen, that the BES spectrum in the respective line-of-sight is made up of photons

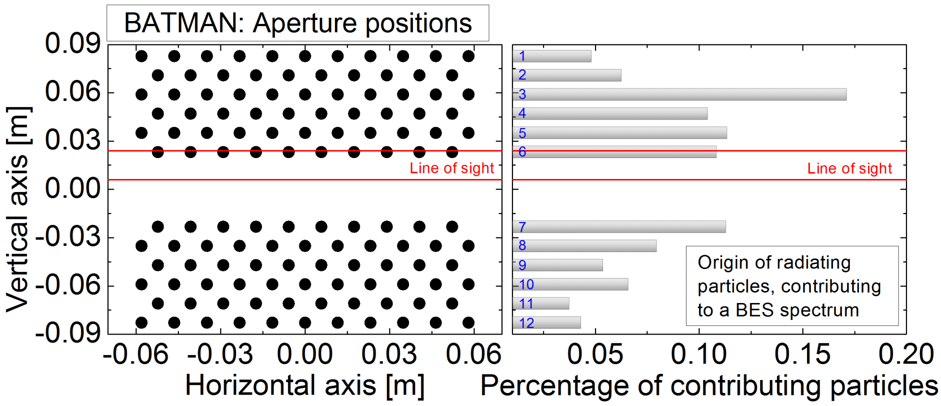

Figure 5.5: *Left side: grid pattern of the LAG at BATMAN. Additionally the vertical position of the line-of-sight is shown. Right side: origin and amount of contributing photons from the radiating particles leading to a BES spectrum at BATMAN.*

emitted from particles coming from every aperture row, respectively from every grid aperture. Thereby the contributions from every row, which lie between 4% and 17%, are significant. Surprisingly, the largest amount comes from row 3, which might be due to statistics.

For a better understanding, the formation of the Doppler shifted peak, with the influence of the origin-effect, can be described in the following. For the sake of simplicity the line-of-sight in this exemplified case is assumed to be vertically in the center of the twelve aperture rows. The trajectory angles of the particles coming from each row are Gaussian distributed as it is the standard starting condition of BBC-NI Simple. Figure 5.6 shows on the left and on the right side each three curves of a Gaussian trajectory angle distribution. These distributions refer to the particles from the respective rows, which can be identified by the number on the six graphs.

Particles from row 1 and 12, the two most outer ones, can only get into the centered line-of-sight when the angle between the particle velocity vector and the beamlet axis perpendicular to the trajectory angle τ is large enough. This angle, perpendicular to the trajectory angle τ, limits the possible trajectory angle range due to the geometry. This range is different for each aperture row and indicated in the six periphery graphs by the grey area.

The trajectory angle distribution of the particles (which is also valid for the radiating particles) seen by the line-of-sight is the sum of all grey areas. The graph in the center of figure 5.6 shows the sum with a comparison of the original

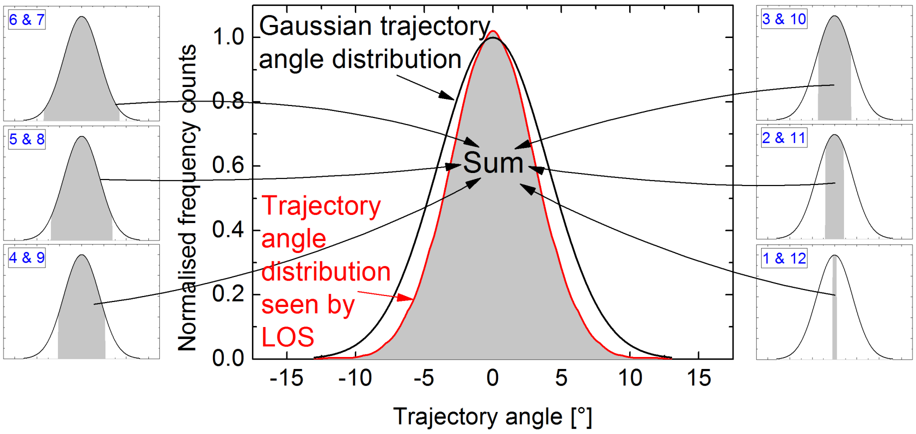

Figure 5.6: *Model of the composition for the angular distribution seen by a line-of-sight in the center (vertically). The grey area of the six graphs located on the left and right side of the main graph indicate the range of trajectory angles from* H_0 *of the respective aperture rows which are seen by the line-of-sight.*

Gaussian trajectory angle distribution for the particles of each aperture. The contribution from particles from of all apertures leads to a superelevation of the distribution profile in the center. In a result, the angle distribution seen by the line-of-sight is more narrow than it was set in the starting conditions and it is non-Gaussian. The sketch makes clear, that the origin-effect is more pronounced with increasing divergence.

In the case of the investigated spectrum at BATMAN, the effect described above, leads to a trajectory angle distribution which is close to a Lorentzian one. In fact this simple model can only describe roughly the geometric effect while the 3D calculation in BBC-NI Simple allows the determination of the realistic trajectory angle distribution.

Discussion

The non-Gaussian shape of the main Doppler shifted peak for small ion source is mainly understood. Three basic effects lead to the shape of the Doppler shifted peak. First the angle distribution of the emitting particles seen by the line-of-sight is narrower than the original distribution of the overall beam particles. Therefore, the Gaussian peak will also be narrower than expected. This effect is decreasing with lower divergence since this reduces the contribution of radiating particles coming from apertures which are vertically far away from the line-of-sight. Secondly, due to the angle-effect the left edge of the Doppler shifted peak broadens up. Thirdly, the contribution of stripping particles leads to a different broadening of the right edge. This depends on the density profile in the extraction system and the extraction voltage (see chapter 5.4).

Summarizing all effects, the shape of the Doppler shifted peak is only Gaussian for the special case when the divergence is low. Besides this a divergence evaluated from the Doppler shifted peak is rather a global beam parameter than representing the divergence of some aperture rows.

5.1.1.3 Advanced Doppler peak evaluation

The next step is to find a new evaluation method for evaluating the BES spectra at BATMAN since the assumption of a Gaussian shape of the Doppler shifted peak is only valid for low divergence. For small divergences the standard evaluation (see section 3.2.2) is expected to be still a good application. BATMAN is usually operating at divergences roughly between 1.5° and 4° [85]. In the next paragraph a new evaluation, the parametrisation method, is presented and compared with the standard evaluation. This comparison will show for which divergence range the standard evaluation may still be valid and where the new parametrisation method is necessary.

The idea is to find a parametrisation of the full Doppler shifted peak. For this purpose, the left side of the peak, which is determined by the beam optics in contrast to the right side (stripping contributions), has to be fitted by a user-defined function F which delivers a representative parameter w. Since the function is likely to have a bell-shaped form, the parameter probably will be a kind of width. This representative parameter is the input for a parametrisation function whose solution is a value for the divergence. For the function F it turned out, that the left edge of the Doppler shifted peak can be fitted quite well by a Lorentz curve (see equation (5.2)). The shape of the left side of the Doppler shifted peak depends on the individual contribution of the particles from every aperture and the angle effect. Therefore the shape depends on the position and observation angle of the line-of-sight. This means the parameters of a parametrisation can only be provided for every line-of-sight individually. The shape of the Doppler shifted peak is determined by the normalised perveances in the extraction grid system and the space charge of the beam. The free parameters are therefore the

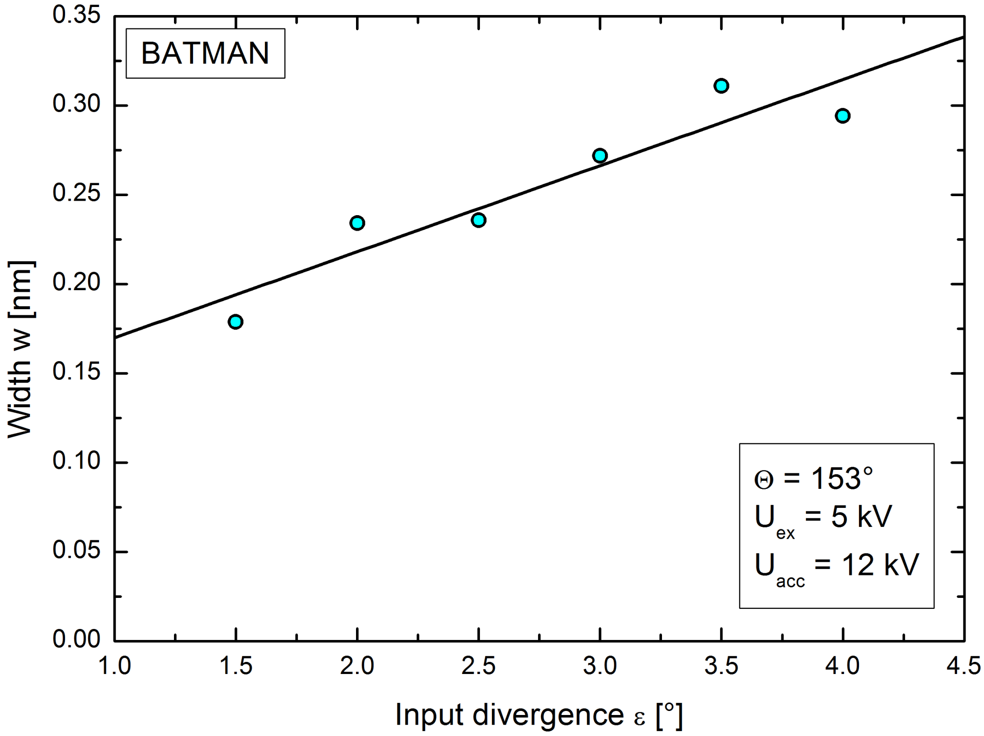

Figure 5.7: *Correlation between input divergence in BBC-NI Simple and the width obtained from the fit of the left side of the simulated Doppler shifted peak with a Lorentz curve. The parameters for the extraction and acceleration voltage for the underlying calculations were fixed simulating the change of the divergence by changing the current density.*

acceleration voltage U_{acc}, the extraction voltage U_{ex} and the extracted current density j_{H^-}.

For a parametrisation a set of calculations with BBC-NI Simple were performed. For a given total voltage, which consists of a tuple of fixed U_{acc} and U_{ex}, several BES spectra for the prevailing line-of-sight at BATMAN were simulated. For each tuple divergences between 1.5° and 4°, which is the main divergence range at BATMAN, with a step size of 0.5° were set as input. This variation refers to different perveances by a change of the extracted current densities, determining the divergence. From a Lorentz fit of the Doppler shifted peak, the width w was determined from the evaluation of the calculated spectrum for the different divergences at fixed extraction and acceleration voltage. Figure 5.7 shows the correlation between the input divergence of BBC-NI Simple calculations and the width obtained from the Lorentz fit of the Doppler shifted peak in the simulated BES spectrum. The figure shows the case for an extraction voltage of 5 kV and an acceleration voltage of 12 kV. The BBC-NI Simple simulations were performed for extraction voltages between 5 kV and 9 kV in 1 kV steps at a fixed acceleration voltage. The acceleration voltage was varied between 12 kV and 16 kV in 1 kV steps. It turned out that the correlation between w and the divergence ϵ is almost linear in every investigated case, hence ϵ can be parameterised by:

$$\epsilon = m_1 w + t_1 \,, \tag{5.3}$$

with m_1 being the slope and t_1 as the interception. Furthermore the slope and the interception changes again linearly with the extraction voltage keeping the acceleration voltage fixed. Again this can be described by a linear relation:

$$\begin{aligned} m_1(U_{\mathrm{ex}}) &= m_2 U_{\mathrm{ex}} + t_2 \,, & (5.4) \\ t_1(U_{\mathrm{ex}}) &= m_3 U_{\mathrm{ex}} + t_3 \,. & (5.5) \end{aligned}$$

m_2 and m_3 are the slopes and t_2 and t_3 are the interceptions. For these four parameters, the same regulation as for m_1 and t_1 can be continued for the variation of the acceleration voltage leading to four further equations:

$$\begin{aligned} m_2(U_{\mathrm{acc}}) &= aU_{\mathrm{acc}} + b \,, & (5.6) \\ t_3(U_{\mathrm{acc}}) &= cU_{\mathrm{acc}} + d \,, & (5.7) \\ m_2(U_{\mathrm{acc}}) &= eU_{\mathrm{acc}} + f \,, & (5.8) \\ t_3(U_{\mathrm{acc}}) &= gU_{\mathrm{acc}} + h \,, & (5.9) \end{aligned}$$

and by linking equations 5.3 - 5.9 together, the parametrisation function for the divergence has the form

$$\epsilon = ((a \cdot U_{\mathrm{acc}} + b) \cdot U_{\mathrm{ex}} + (c \cdot U_{\mathrm{acc}} + d))w + ((e \cdot U_{\mathrm{acc}} + f) \cdot U_{\mathrm{ex}} + (g \cdot U_{\mathrm{acc}} + h)) \,. \tag{5.10}$$

The parameters a, b, c, d, e, f, g, h are then the individual characteristic parameters for a certain line-of-sight.
For a comparison of the two BES evaluation methods, figure 5.8 shows the correlation between input and output divergence. The parametrisation method delivers evaluated divergences which are rather close to the input. For the standard evaluation this is only valid for input divergences around 2°.
Figure 5.9 shows the average error by evaluating the divergence of the calculated spectra either with the parametrisation method or the standard evaluation. Since

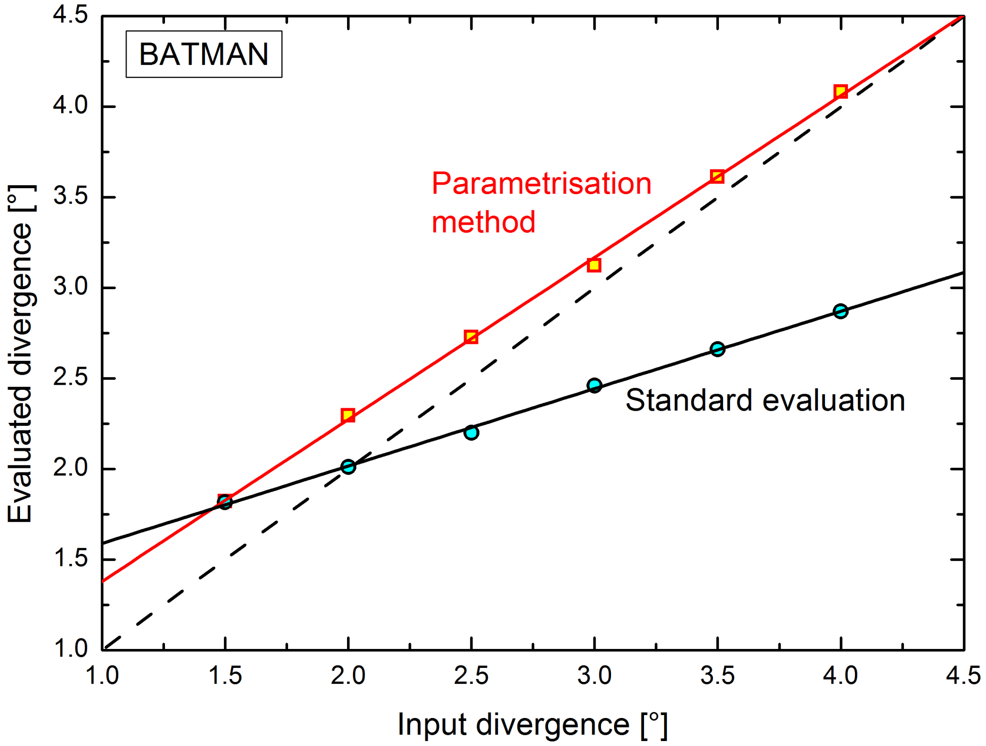

Figure 5.8: *Correlation between the obtained divergence by the parametrisation method and the standard evaluation with the input divergence of the analysed BES spectrum.*

for every input divergence several calculations (by a variation of the total voltage, as already explained) were performed, a standard deviation of the average error was calculated, which is also shown in figure 5.9.

Finally, for a divergence of 3° and more the parametrisation method reaches an error less than 15% which is better then the standard evaluation. At lower divergences the standard evaluation is still better. For a divergence of 1.5° both methods again have a relative high error of more than 20%. However, in order to determine a beam inhomogeneity of less than 10% with a relative error of 10% from several BES spectra, as required by ITER, the error of the divergence evaluation should be at least below 5%. This is because, as explained in section 2.5.2.2, the relative error of the current density measurement, which is necessary for equation (2.29), should be less than 5%. However the determination of a current density from several beamlets from the divergence measurement of a single BES line-of-sight does also have an error. This means that also the present parametrisation method is still not sufficient for the determination of the beam inhomogeneity with a BES line-of-sight array.

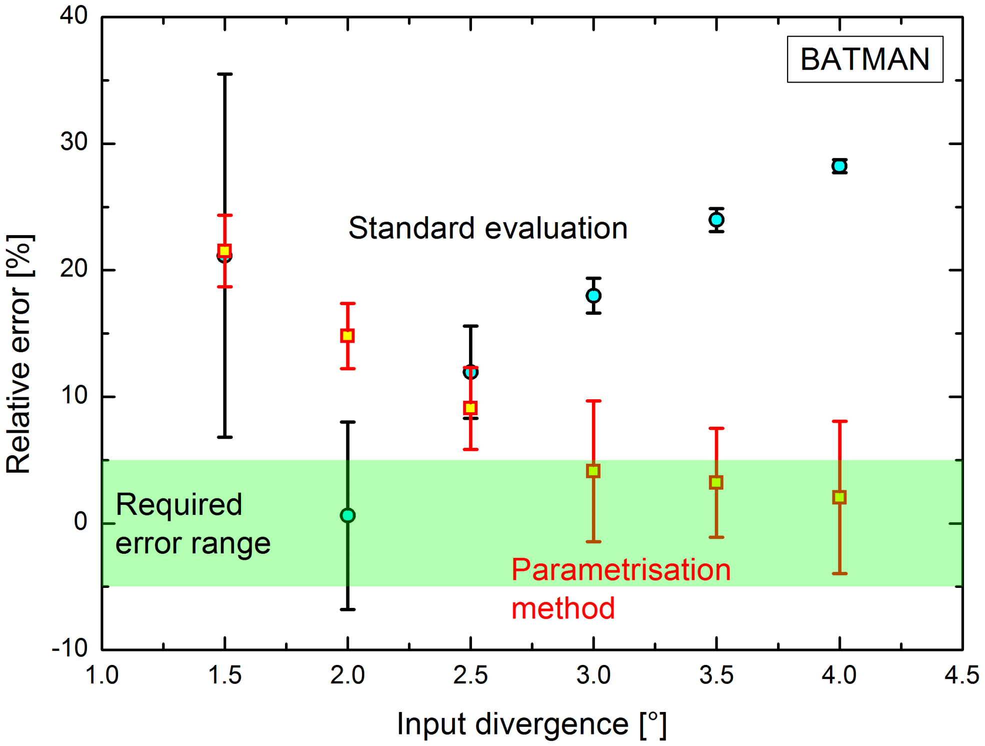

Figure 5.9: *Error occurring by evaluating the divergence from a BES spectrum with the standard evaluation and parametrisation method at BATMAN. The green area indicates the required error range for an absolute error of less than* 5%*.*

The reason for this relative large deviation of the parametrisation method at the low divergences is more probable due to the fit of the left side of the Doppler shifted peak with a Lorentz curve. In this regime the Doppler shifted peak is close to Gaussian, since the shape effects are less pronounced at low divergences. The Lorentz fit leads to an over estimation of the divergence. For future BES evaluation it may be the best solution to combine the standard evaluation and the parametrisation method. This could be done by choosing the respective evaluation depending on the beam optics regime.

However, also the standard evaluation with a Gaussian fit fails at 1.5°. This is not a mathematical problem, but has its reason in the automatic evaluation routine. The module, which sets the starting parameters for the Gaussian fit, is very simple. The determination of the start values for the free parameters is optimised for large divergences, i.e. $> 3°$.

The simulation and benchmark of the BES spectrum at the small source at BATMAN gives a better understanding of the spectrum formation. With BBC-

NI Simple the measurements of the BES diagnostic tool can be simulated and the evaluation of the spectrum can be improved. With this possibility the next step is to transfer this knowledge and application to the large source at ELISE. The aim is to have a proper evaluation of BES spectra at large sources. Furthermore the main goal is to determine the beam inhomogeneity at ELISE with the help of the BES line-of-sight array.

5.1.2 Large NBI ion sources

Like at BATMAN, the BES spectra obtained at ELISE will be influenced by the effects described above. At ELISE the Doppler shifted peak is at a higher wavelength (red-shifted) than the unshifted peak due to the observation angle of the BES system. The first effect, influencing the BES spectra, is the angle distribution of the radiating hydrogen atoms seen by a given line-of-sight (origin effect). Since the grid at ELISE is larger and has more apertures than the one at BATMAN, the effect will be more pronounced. Secondly the area- and angle-effect will also influence the Doppler shifted peak at ELISE. Because the observation angle of the lines-of-sight is smaller than 90°, the angle-effect will increase the left side of the Doppler shifted peak while the area effect again plays a comparatively minor role due to the same reason as in BATMAN. Thirdly the photons emitted from stripped particles at high energies comparable to the total acceleration energy, additionally increase the left side of the Doppler shifted peak. Therefore, an evaluation of the right side of the Doppler shifted peak to determine the beam divergence has only to consider the first effect, i.e. the angle distribution seen by the line-of-sight.

ELISE started its beam operation in September 2013 without caesium. This means the negative ions are mainly coming from volume production leading to a low extracted current density. Additionally, the flow of negative ions to plasma grid aperture can be assumed to be laminar so that the beam models should be more realistic. Figure 5.10 shows a BES spectrum obtained at ELISE in the line-of-sight number 5 for the pulse # 2764. The pulse parameters are shown in table 5.1. The shape of the Doppler shifted is highly non-symmetric and has a strong broadening. Both properties are unexpected. Furthermore the maximum of the Doppler peak is not at the wavelength where the Doppler shift is expected which cannot be explained up to now. Additionally a stripping peak is not clearly visible. The observations in the BES spectra obtained for the line-of-sight number 5, are also valid for the other horizontal lines-of-sight which are arranged in a vertical

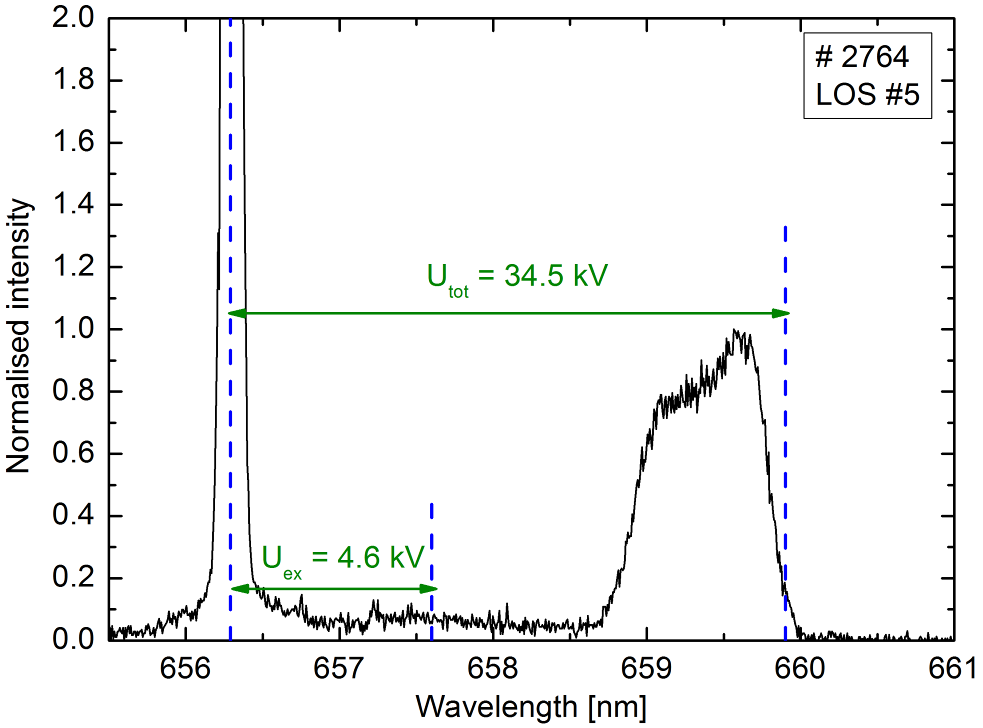

Figure 5.10: *BES spectrum obtained at ELISE at the horizontal LOS # 5 in volume operation. The peak positions predicted from theory are indicated by the blue dotted lines. The stripping peak is barely pronounced. The pulse parameters are shown in table 5.1.*

array. The BES spectra from the vertical lines-of-sight are much more closer to the expected ones. Figure 5.11 shows a BES spectrum from the line-of-sight number 19, also from pulse # 2764. It can be seen in the figure, that the shape of the measured Doppler shifted peak is much more similar to the shape of the calculated Doppler shifted peak. However, the width of the measured Doppler shifted peak is larger than the width of the Doppler shifted peak from the BBC-NI Simple calculation. As a result it can be summarised that also in the spectra from the vertical lines-of-sight the maximum of the Doppler shifted peak is not at the expected position for unknown reason.

Although having rather off-normal source conditions (low voltages, low extracted current density, no caesium), investigating the irregular Doppler shifted peak, especially the one spectra obtained with the horizontal lines-of-sight, in this unfavourable perveance condition (below the perveance optimum which is between 0.1 and 0.2 as shown in section 2.5.2.1) might lead to a better understanding of the BES spectrum in general.

Table 5.1: *Pulse parameters for shot number # 2764. For this shot, the source was operated in volume prduction.*

Parameter	**Value**
Isotope	Hydrogen
Filling pressure	0.59 Pa
Tank pressure	0.016 Pa
Extraction voltage	4.6 kV
Acceleration voltage	29.9 kV
Total voltage	34.5 kV
Extracted current density	20.9 $\mathrm{A/m^2}$
Ratio of co-extracted electrons to ions	9.9
Normalised perveance	0.056

Figure 5.12 shows the Doppler shifted peak for nine different pulses (pulse # 2764 from figure 5.10 is the upper left one) at different normalised perveances. The peaks were smoothed for a better presentation. From left to right and from top to bottom the extraction voltage was decreased which led to higher normalised perveance. The normalised perveance optimum was around 2.1 kV due to the low extracted current density as the source was operated in caesium-free condition.

In the normalised perveance optimum, the Doppler shifted peak has a bell shaped curve which seems to be Gaussian. To higher and lower normalised perveances the shape becomes broader and non-regular. Additionally the center of the peak shifts to lower wavelengths with higher perveance. Within this chapter, an explanation for the unexpected shape of the Doppler shifted peak will be discussed.

Figure 5.13 shows again the measured spectrum from pulse #2764 from the horizontal line-of-sight number 5, which is in the vertical center of the beamlet groups in the bottom segment (see figure 2.10 on page 32) and as a comparison spectra from different simulations. The shape of the Doppler shifted peak divers clearly from the expected one which was calculated with BBC-NI Simple. In order to understand the reason for the deviation the measured Doppler shifted peak was fitted with four Gaussians as a first step. The assumption for the fitting was to separate the ELISE beam into four “sub-beams” representing the four beamlet groups in a grid segment (see figure 2.10). The focus of every sub-beam, i.e. the predominant direction, was chosen individually leading to individual horizontal deflection angles. The Doppler shifted peak generated by each sub-beam is assumed to have a Gaussian profile. The deflection angle then determines

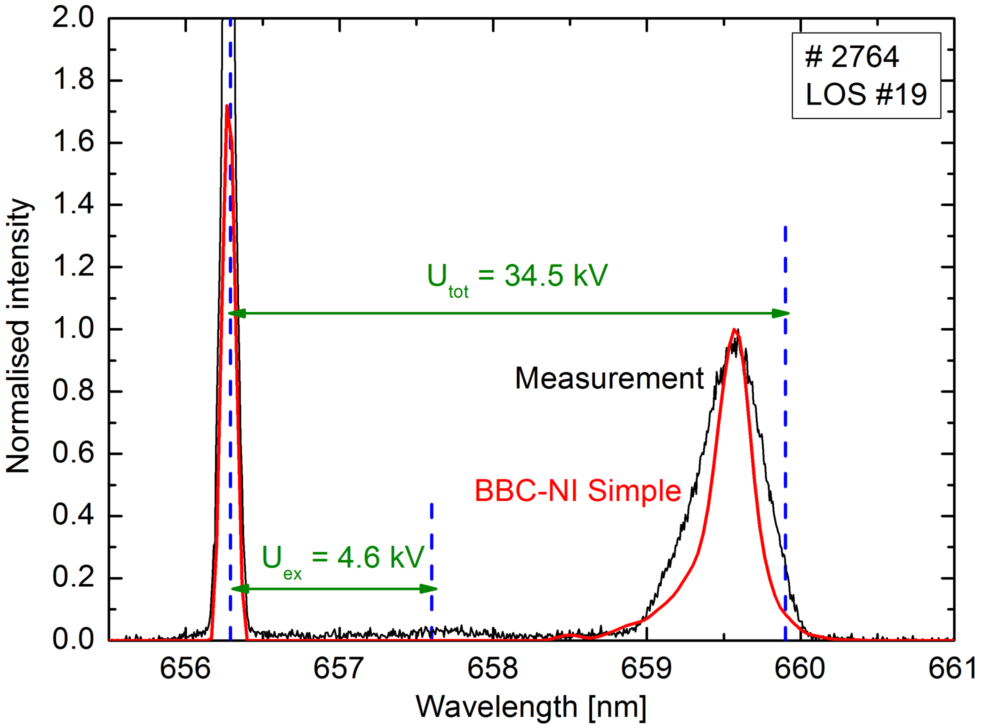

Figure 5.11: *BES spectrum obtained at ELISE at the vertical LOS # 19 in volume operation. The peak positions predicted from theory are indicated by the blue dotted lines. Additionally a BES spectrum for a BBC-NI Simple calculation is shown.*

the peak position. Finally the measured Doppler shifted peak was fitted by the sum of the four Gaussians. Table 5.2 shows the necessary deflection angles of the four sub-beams with respect to the beam axis. A positive value stands for a deflection of the sub-beam to the left side relative to the beam direction, a negative value stands for a deflection to the right side. The predictions for the deflection angles were checked with BBC-NI Simple calculations. Additionally, the best solution from a calculation series for the Doppler shifted peak is shown in figure 5.13 (red line). The deflection angles for the four sub-beams are given in table 5.2. The trend for the angles obtained by the simple four Gaussian fits and by BBC-NI Simple is roughly the same and also their magnitude, which is quite large.

However, introducing the four sub-beams is only a technically solution and does not have mandatorily a physical background. In order to explain the shape of the Doppler shifted peak, a significant part of fully accelerated beam particles have to be horizontally deflected by an angle which is in the range of the pre-

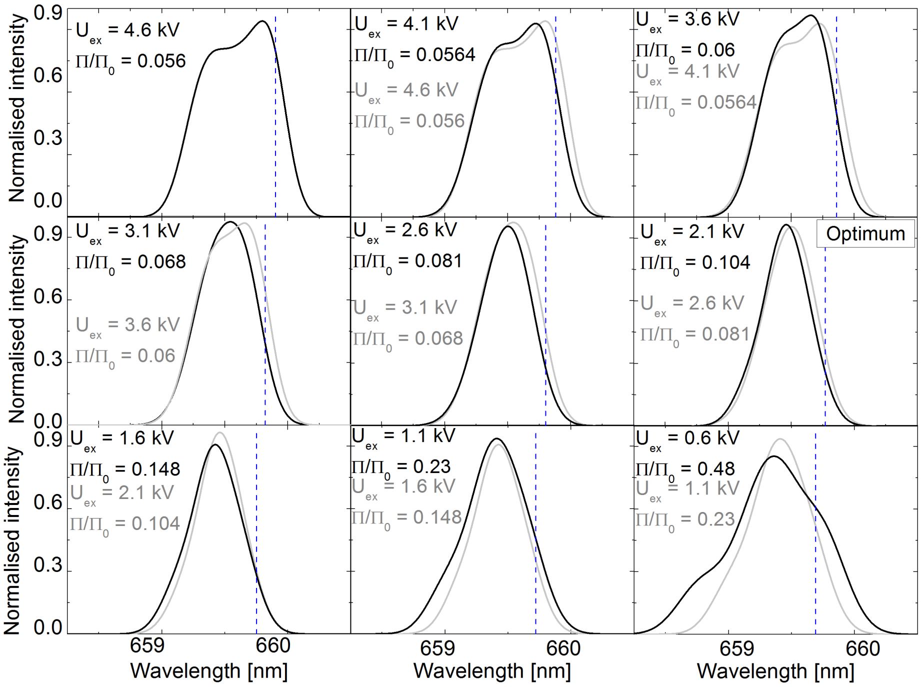

Figure 5.12: *Doppler shifted peaks from a BES spectrum of line-of-sight # 5 obtained at ELISE during a variation of the perveance. In every picture except for the first one, the actual Doppler shifted peak is indicated as a black curve while the Doppler shifted peak from the last pulse with a lower normalised perveance is indicated in grey. This is for a pulse to pulse comparison. The blue dotted line indicates the position of the maximum of the main Doppler shifted peak according to the theory.*

dicted ones in table 5.2. The reason for the occurrence of these angles is not clear up to now. The change of the shape of the Doppler shifted peak due to the normalised perveance variation is an indication that the Doppler shifted peak is influenced by the beam optics. This means that the electric and magnetic field configuration in the extraction system might lead to horizontal deflection angles. Furthermore, the deflected beamlets affect the whole beam represented by BES spectra. With the presence of a complex 3D magnetic field topology, the space charge of the beamlets influences the beam optics in an extensively way. For a different space charge of the beamlet, beam particles can travel through different magnetic field regions affecting their trajectory in a different way. For this reason the deflection angle (horizontal and vertical) can be influenced by the magnetic field, the extraction voltage (at a fixed acceleration voltage) and the extracted current density. As it will be shown in section 5.3 not only the deflection angle

Table 5.2: *Predicted deflection angles from the fit of the Doppler shifted peak with four Gaussians and from a BBC-NI Simple calculation with four different deflection angles for the four "sub-beam" from the four beamlet groups of the upper and lower grid half.*

Beamlet group	Fit	BBC-NI Simple
1	3.2°	4°
2	−0.2°	1.4°
3	−3.4°	−1.2°
4	−6.5°	−3.8°

but the whole beamlet homogeneity is affected.

In a next step, in order to study the influence of the magnetic field, the electric field and the extracted current density on the deflection angle of a beamlet, single aperture calculations with BBC-NI Advanced with the parameters of pulse # 2764 are presented. Subsequently, in section 5.1.2.4 the BES spectra of BBC-NI Simple calculations, utilising the obtained deflection angles from the BBC-NI Advanced calculations will be discussed, in order to check the validity of the calculated deflection angles.

5.1.2.1 Influence of the magnetic field

Figure 5.14 shows the horizontal and vertical deflection angles for different magnetic field configurations in the ELISE extraction system. As already explained in section 2.4, the magnetic filter field is generated by a current in the plasma grid which can be varied. Additionally the field of the deflection magnets is present in the extraction system, which is fixed. The horizontal and vertical magnetic field components along the beam axis for the ELISE grid system were already introduced in figure 2.15 on page 42. The magnetic filter field was calculated by ANSYS for a plasma grid current of 1 kA. The absolute values for the magnetic field strength are linearly scaled with the plasma grid current.

Four cases can be seen in figure 5.14:

Case 1: Both magnetic fields are zero, i.e. the plasma grid current is zero and no deflection magnets in the extraction grid. Then the deflection angles are zero as expected.

Case 2: No electron deflection field but the magnetic filter field is present. A vertical deflection only is expected, because the Lorentz force assumes only

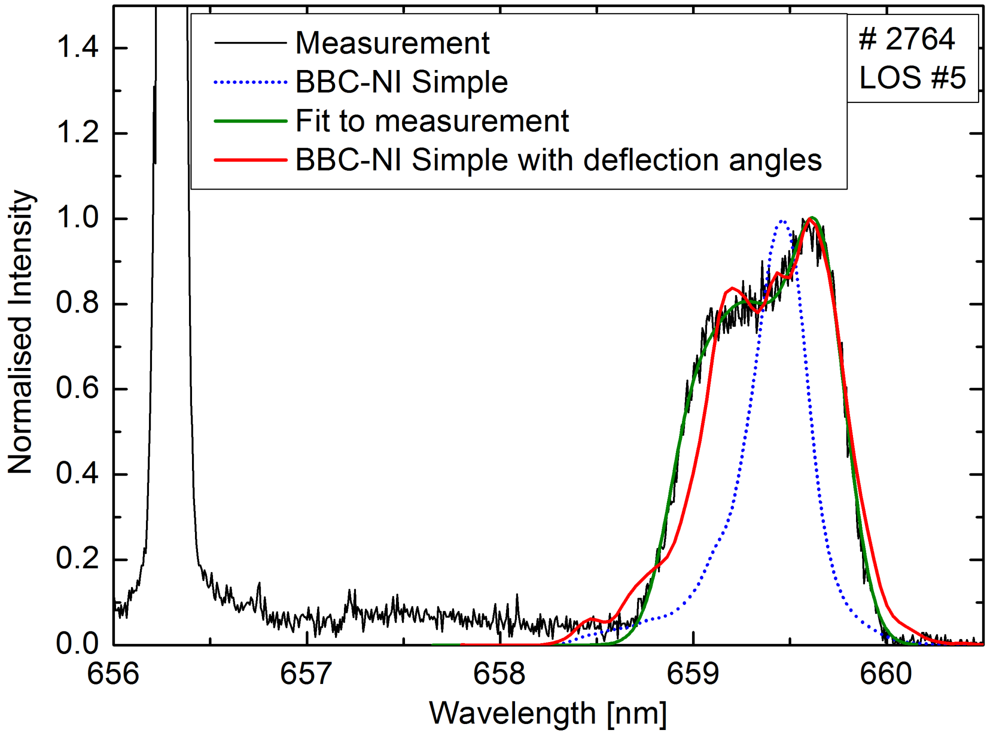

Figure 5.13: *BES spectrum obtained at ELISE (same as in figure 5.10). Also shown is the expected shape of the Doppler shifted peak by the dotted line. Furthermore a fit to the measured spectrum with four Gaussians and a spectrum from a BBC-NI Simple calculation considering horizontal deflection angles is shown.*

magnetic field components in horizontal direction. The calculation shows also a small horizontal deflection angle. This can be explained by the 3D structure of the filter field which has also vertical magnetic field components. However the influence of the filter field on the horizontal deflection is small.

Case 3: Both magnetic fields are present. In this case significant deflection angles emerge. As expected, a comparatively large horizontal and a small vertical deflection angle can be seen. The vertical deflection angle increases with higher PG current due to the higher horizontal magnetic field component. Below 1.5 kA the vertical deflection angle stays more or less constant.

The horizontal deflection angle shows the same behaviour below 1.5 kA. However with roughly 0.6° the angle is already significant, but still less than the first predicted angles (see table 5.2). With higher PG current a small decrease of the horizontal deflection angle can be observed due to the larger influence of the filter field, which leads to a small decrease of the vertical magnetic field component.

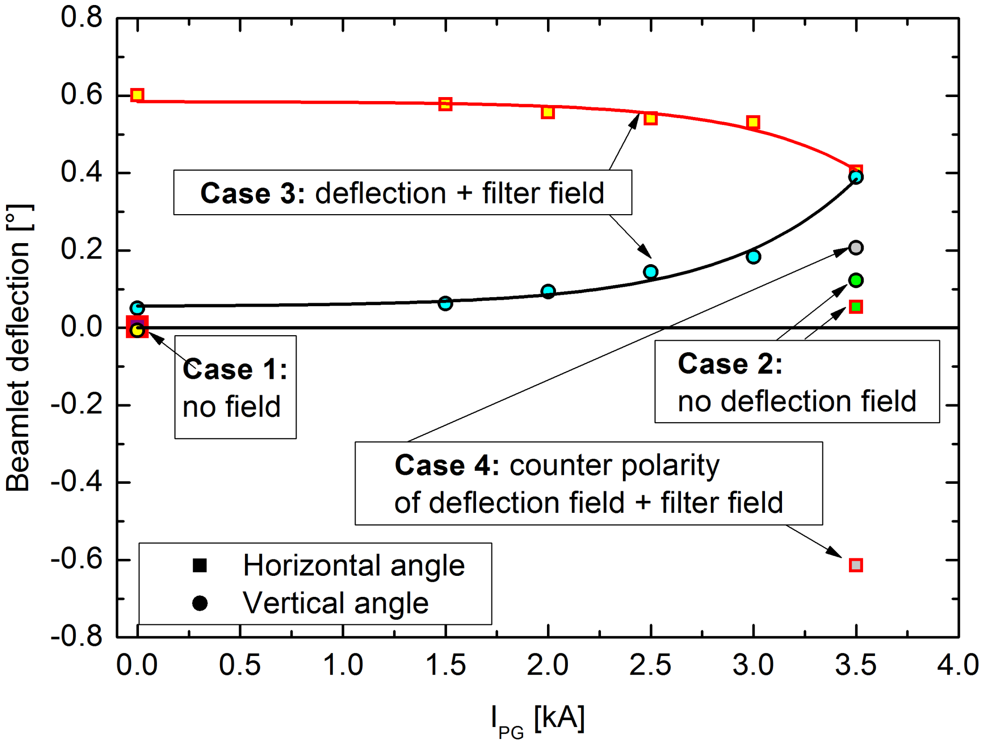

Figure 5.14: *Influence of various magnetic field configurations on the vertical and horizontal deflection angle of a beamlet obtained from BBC-NI Advanced calculations for the underlying pulse # 2764.*

Case 4: Both magnetic fields are present, but the deflection field has reverse polarity to case 3. This is because in the experiment the polarity of the deflection field alternates from aperture row to aperture row. Hence the two magnetic fields can also add up their vertical magnetic field components leading to a higher absolute horizontal deflection angle. However also the sign of the horizontal deflection angle is changed.

The calculations for the different magnetic field cases show a horizontal deflection angle due to the deflection field. Since the polarity of the deflection field alternates for each aperture row, the sign for the horizontal deflection angle alternates. The absolute value however has only a small variation with the polarity of the deflection field.

5.1.2.2 Influence of the extraction voltage

Figure 5.15 shows the obtained deflection angles by the single aperture calculations with BBC-NI Advanced for the normalised perveance variation presented

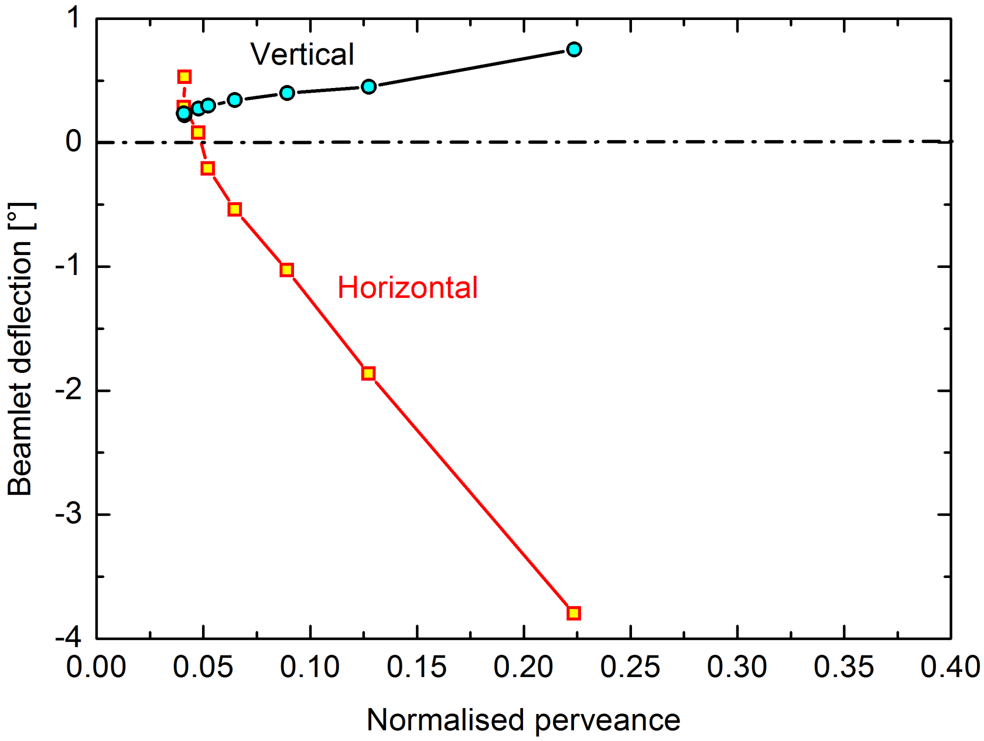

Figure 5.15: *Beamlet deflection for the variation of the normalised perveance by changing the extraction voltage, which also means a change in the extracted current density. The values are obtained from BBC-NI Advanced calculations with the underlying input parameters from the pulses of the perveance variation shown in figure 5.12 for one beamlet only.*

in figure 5.12. The magnetic field configuration refers to plasma grid current of 3.5 kA as in the experiment together with deflection magnets in the extraction system.

The vertical deflection angle has only a slight increase with higher normalised perveance. The horizontal deflection angle however decreases with increasing normalised perveance and even changes its sign during the variation. The deflection also reaches angular values which are comparable with the ones from the simple analysis of the ELISE BES spectrum (see table 5.2).

5.1.2.3 Influence of the extracted current density

The normalised perveance is commonly changed by the extraction voltage but also by a variation of the extracted current when the extraction voltage is constant. In principle the beam optics for a certain normalised perveance value are always the same without magnetic field. However an additional magnetic field in the

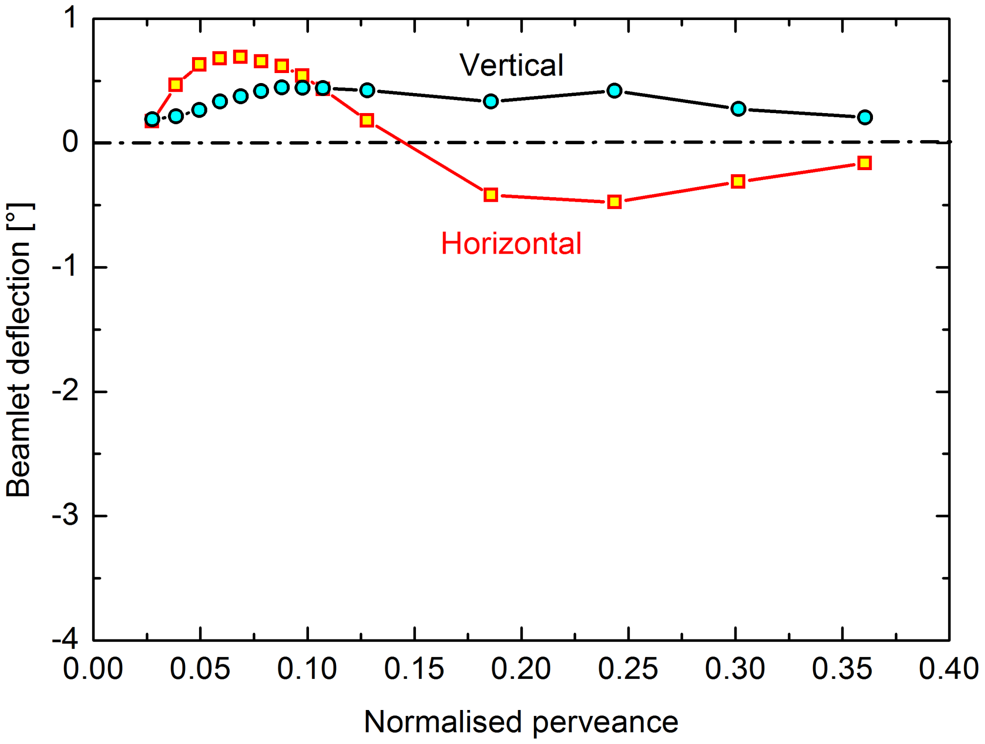

Figure 5.16: *Beamlet deflection for the variation of the normalised perveance by changing the extraction current at a fixed extraction voltage of 4.6 kV. The values are obtained from BBC-NI Advanced calculations.*

extraction system, as it is the case in the negative ion sources for ITER NBI, increases the complexity of the beamlet formation. The beam optics cannot be described explicitly by the value of the normalised perveance. Instead the values of the extracted current density and extraction voltage have to be taken into account. This means a change in the normalised perveance either by the extracted current density or the extraction voltage leads to different beam optics and therefore also deflection angles.

Figure 5.16 shows the horizontal and vertical deflection angle for a normalised perveance variation by changing the extracted current with fixed extraction voltage $U_{\mathrm{ex}} = 4.6\,\mathrm{kV}$ like in pulse # 2764. The vertical deflection slightly increases up to a normalised perveance of 0.1 and decreases again. However the minimum vertical deflection angle is always above 0.2°.

The horizontal deflection angle first increases up 0.7° at a normalised perveance of 0.07 and then decreases to negative values with a minimum of $-0.5°$ at a normalised perveance of 0.25. The zero crossing is at a normalised perveance of about 0.15 which is in the range of the optimum normalised perveance condition for the ELISE grid system. At this point an undisturbed BES spectrum is expected, which means the shape of the Doppler shifted peak is barely influenced by the beamlet deflection. This has been already observed in figure 5.12.

The reason for the different behavior of the horizontal deflection angle for a normalised perveance variation on the one hand by changing the extraction voltage and on the other hand by changing the extracted current is due to the space charge of the beamlet. Increasing the extracted current at the same extraction voltage leads to a higher space charge of the beamlet. The subsequent attractive and repulsive forces from particle interaction has a huge impact on the particle trajectories. The particle will likely travel through different electric and magnetic field regions for the two cases of normalised perveance variation because of the beamlet space charge. Therefore the trajectory for both cases at equal normalised perveance can be complectly different.

5.1.2.4 Reconstruction of ELISE BES spectra

The study on the beamlet deflection by the magnetic field configuration at ELISE showed up a possible reason for the unexpected shape of the Doppler shifted peak in figure 5.13. A BBC-NI Simple run for the pulses of the normalised perveance variation shown in figure 5.12 with the input of the obtained deflection angles from the BBC-NI Advanced calculations should allow the reconstruction of the BES spectra.

Figure 5.17 presents the result for two representative pulses from the normalised perveance variation shown in figure 5.12. The upper one shows the BES spectrum of LOS number 5 which is in the vertical center of lower beamlet groups. The extraction voltage was $U_{\mathrm{ex}} = 4.6\,\mathrm{kV}$ leading to under perveant conditions due to the low extracted current. The Doppler shifted peak in the spectrum of the BBC-NI Simple calculation, taking the deflection angles obtained from the BBC-NI Advanced calculation into account, does not fit the measured one.

The lower graph shows the same spectra (from the measurement and from BBC-NI Simple) but for a pulse with an extraction voltage of $U_{\mathrm{ex}} = 2.1\,\mathrm{kV}$. The beam of this pulse is around the normalised perveance optimum. In principle the simulated spectrum predominantly fits to the measured one with some deviation at the left side.

BBC-NI Simple assumes a Gaussian distribution of the particle velocity angle with respect to the beamlet axis. Considering a horizontal or vertical deflection angle in the model is simply done by adding an offset angle to the distribution.

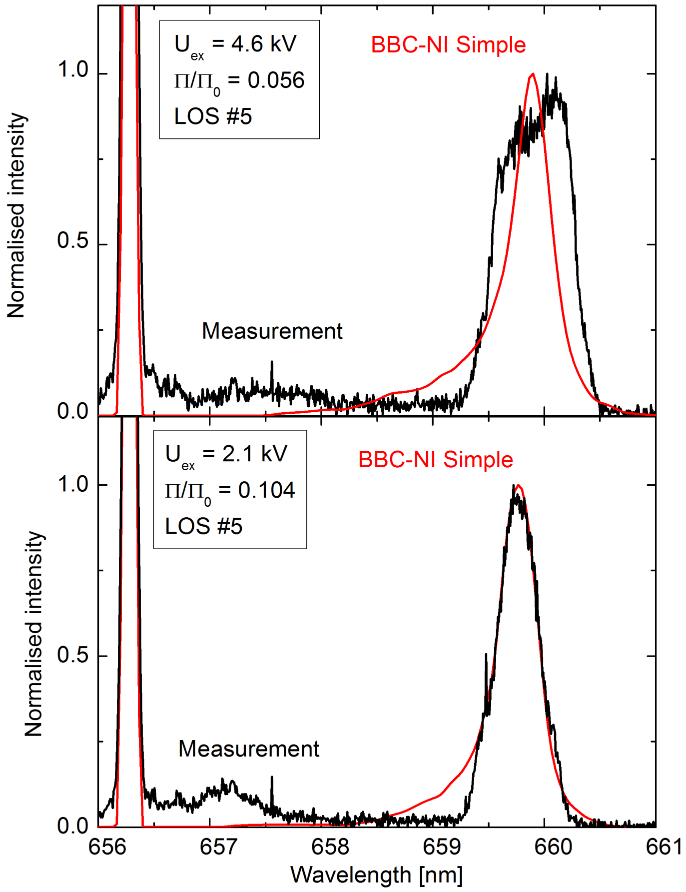

Figure 5.17: *ELISE BES spectra for two different extraction voltages. For the BBC-NI Simple calculation the obtained deflection angles from previous simulations were obtained from the BBC-NI Advanced calculations concerning the deflection angles.*

Actually the presence of the magnetic field may change the whole velocity angle distribution of the beamlet particles. The model of BBC-NI Simple does not sufficiently take this into account.

The next step should be a simulation of the BES spectra shown in figure 5.17 again but with BBC-NI Advanced. For this calculation of the whole beam, at least two different magnetic and electric field maps are necessary because of the alternating polarity of the deflection field. This means a further improvement of BBC-NI.

Up to now the case for a caesium free source was investigated. By caesium

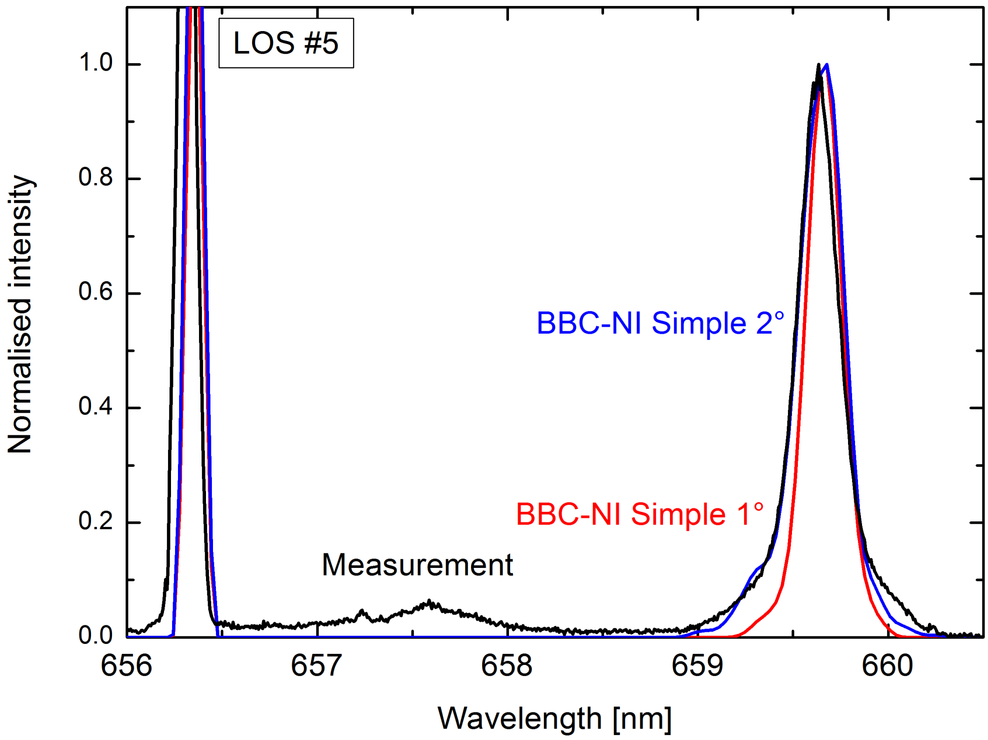

Figure 5.18: *ELISE BES spectrum in a caesium conditioned source with optimum perveance conditions. Additionally two simulated BBC-NI Simple spectra, one for* $1°$ *divergence and one for* $2°$*, are shown. The pulse parameters were* $U_{\mathrm{ex}} = 4.6\,kV$, $U_{\mathrm{acc}} = 24.1\,kV$, $j_{\mathrm{ex}} = 81\,A/m^2$ $\Pi/\Pi_0 = 0.178$ *and* $p_{\mathrm{source}} = 0.49\,Pa$*.*

conditioning of the source, i.e. evaporating caesium into the source, the extracted current density is increased affecting the space charge of each beamlet. Also the electric field in the first gap of the extraction system is different at the perveance optimum, i.e. stronger, compared to the case of an unconditioned source. Finally the flow of the negative ions to the meniscus is different due to the change from volume to surface production. This all affects the beam optics.

Figure 5.18 shows the BES spectrum of the beam pulse # 3331. The spectrum was measured in a well-caesiated source. The beam optics were in the perveance optimum at 0.178 for a extraction voltage of $U_{\mathrm{ex}} = 4.6\,\mathrm{kV}$, because of the extracted current density, which was at $81\,\mathrm{A/m^2}$ due to low RF power operation. The Doppler shifted peak is very narrow in contrast to the peaks obtained in an unconditioned source while the edges show a broadening.

Additionally two simulated spectra are shown in the figure, which come from BBC-NI Simple calculations. No deflection angle was considered. The input divergences were 1° and 2°. Although the obtained total voltage in the BBC-NI

Simple calculations comes from the measurement, it turned out that the Doppler shift in the calculated spectra is less than in the measurement. In order to compare the Doppler shifted peak from the measurement and from the simulations, the simulated spectrum was shifted by a wavelength of 0.1 nm to a higher wavelength. The deviation in the Doppler shift between measurement and simulation corresponds to a difference in the observation angle of about 1.4°. The observation angle is 50° with respect to the beam axis. A deviation of 1.4° means an error of 3 %, which could come partly from the imprecision of the installation. However this is unlikely to fully explain this deviation since the adjusting of the optics heads was carefully performed. Still a small horizontal beam deflection must be present.

The BBC-NI Simple calculation with a divergence of 1° fits very well to the measured peak in the center. In contrast the peak from the simulation with 2° has a good agreement with the measurement at the edges, above all on the left side. For the calculation with 1° the full width at half maximum (FWHM) is 0.22 nm while for calculation with 2° the it is 0.28 nm. The measured Doppler shifted peak has a FWHM of 0.25 nm. This means that the mean divergence of the beamlets seen by the line-of-sight will be very likely between 1° and 2°.

The simulation did not consider any deflection angle but the BES spectrum still fits very good to the measurement. This was already indicated by the perveance variation by changing the extracted current (see figure 5.16). Again, this underlines the statement that the magnetic field is the reason for the unexpected BES spectra, which were obtained in caesium-free source operation and non-optimum normalised perveance conditions.

As a result, this means in optimum normalised perveance conditions, the predicted BES spectra fit to the measured ones. This means for a negative hydrogen ion source for ITER NBI operating with caesium at high performance in the normalised perveance optimum, the BES can be evaluated in the same way as for small sources. However, the question which BES evaluation method (standard evaluation or parametrisation method) obtains better results in large ion source still is not answered yet. This will be discussed in the next section.

5.1.2.5 Advanced evaluation of ELISE BES spectra

Several BBC-NI Simple runs for various divergences at different extraction voltages but constant acceleration voltage were performed. Again like in section 5.1.1.3 for BATMAN the simulated BES spectra were evaluated by the standard evaluation

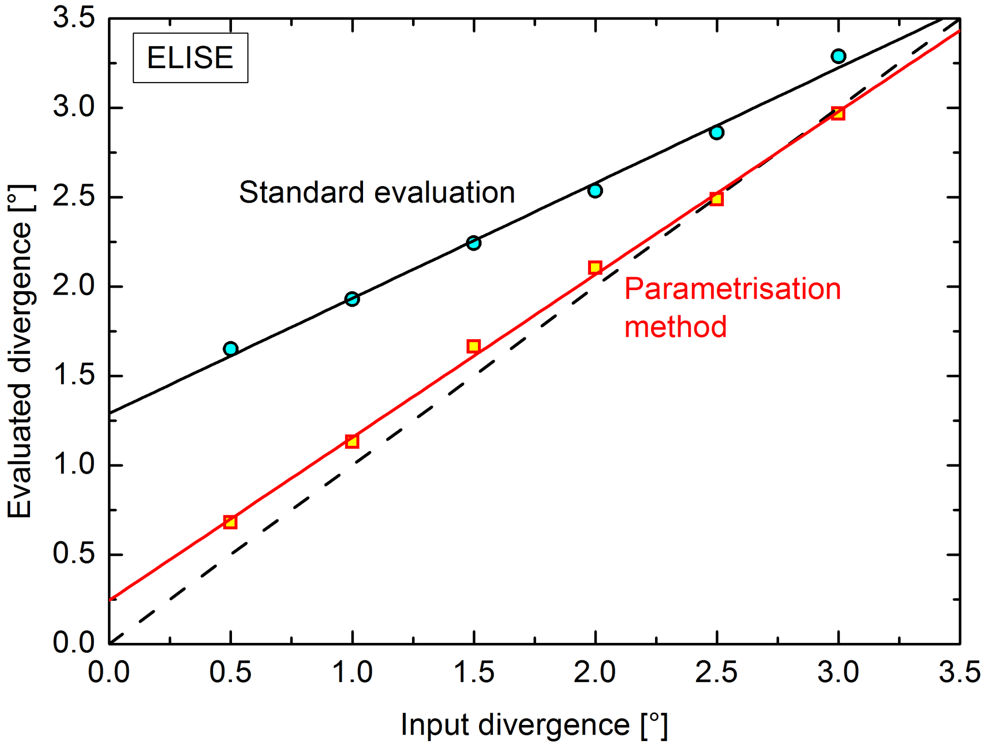

Figure 5.19: *Correlation between the obtained divergence by the parametrisation method and the standard evaluation with the input divergence of the analysed BES spectrum.*

method, which is a Gaussian fit to the center, and with a Lorentz fit of the right side of the main Doppler shifted peak and a parametrisation function following.

Figure 5.19 shows the comparison of the two evaluation methods within typical divergence range for ELISE. The results from the standard evaluation overestimates the divergence while the results from the parametrisation method are already very close to the optimum case. An explanation for this behaviour will be given within the discussion of figure 5.20 in the following.

As for BATMAN several variations of the divergence at fixed voltages have been performed to get a standard deviation of the error. The results are shown in figure 5.20. The parametrisation method shows less error than the standard evaluation. While the error of the standard evaluation is always $\geq 10\%$, the parametrisation method has an error of less than 10% for divergences $\geq 1.5°$. Only for small divergences the error is up to 30% but significantly lower than for the standard evaluation. Compared to BATMAN, the results from the standard evaluation at ELISE are much worse.

The reason for the standard evaluation failing at low divergences can be again

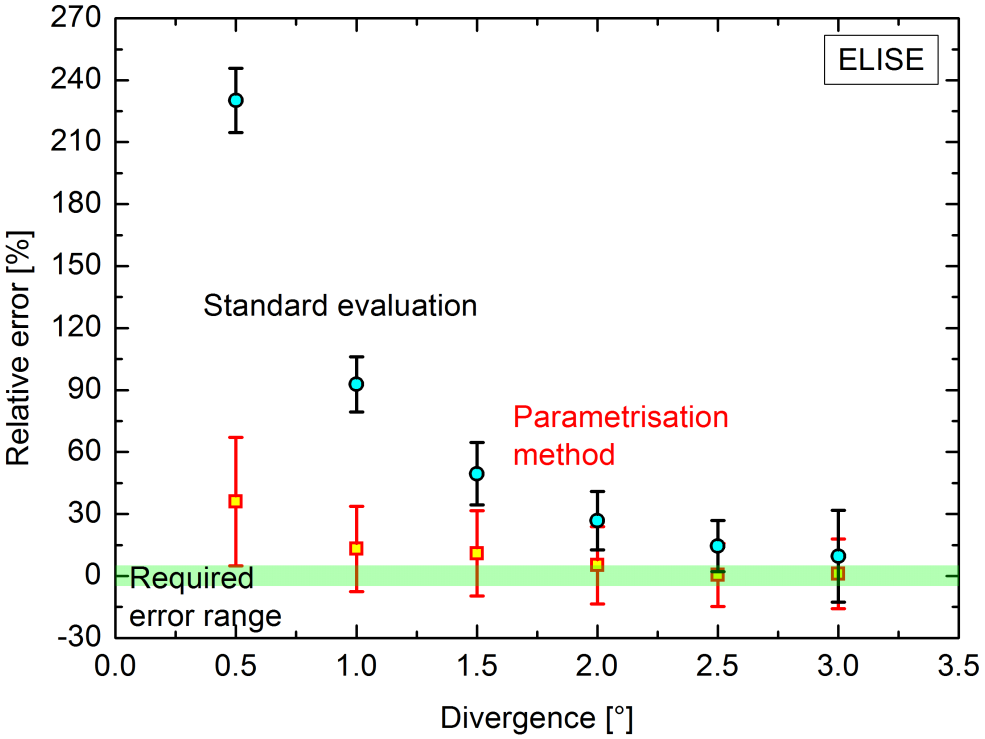

Figure 5.20: *Error occurring by evaluating the divergence from a BES spectrum with the standard evaluation and the parametrisation method at ELISE. The green area indicates the required error range for an absolute error of less than* 5%.

explained by the insufficient parameter initialisation for the Gaussian fit. This issue was already discussed at the end of section 5.1.1.3. Additionally the size of the beam has an influence. Since the radiating particles in one line-of-sight at ELISE have their origin in 640 apertures the horizontal angular distribution seen by the LOS is not Gaussian even at lower divergences as it is the case at BATMAN.

Furthermore the parametrisation method has better results since only the right side of the Doppler shifted peak is fitted with a Lorentz curve. The shape of this side is only correlated with the trajectory angle distribution seen by the line-of-sight. This distribution fits very good to a Lorentz function as already shown in chapter 5.1.1. However, the error at low divergences (less than 1°), which are required for ITER is still too high.

5.1.2.6 Discussion

This chapter showed two important results for BES in large hydrogen ion sources. First, the Doppler shifted peak of the BES spectra in an uncaesiated source or/and at bad normalised perveance conditions cannot be fully explained up to now. However the influence of the magnetic field on the beam particle trajectories leading to an average beamlet deflection is very likely to be the reason for the unexpected shape of the Doppler shifted peak in the BES spectra obtained at ELISE. A better understanding of the underlying beamlet formation is a future task in beamlet reconstruction. At high performance conditions with a beam at normalised perveance optimum, the simulation indeed does fit very well the measured spectrum. Therefore in this operation scenario, beam parameters can be obtained by the BES system. This is the important operation regime, where the required beam inhomogeneity has to be proven.

Furthermore, the parametrisation method allows a more precise determination of the divergence measurement from a BES spectrum as the standard evaluation. However, the standard evaluation is valid in small ion sources with a low aperture number. With the new large negative hydrogen ion source for ITER, the parametrisation method has to be implemented and further improved in order to minimise the error of the evaluation at least below 5%.

5.2 Beam inhomogeneity

This section deals with the possibility to reconstruct the beam inhomogeneity, i.e. the current density distribution at the extraction, from the spectra measured with a BES line-of-sight array and the subsequently evaluation of the spectra with the newly parametrisation method and the standard evaluation as a comparison. The current density distribution at the plasma grid aperture directly influences the individual beamlet divergence. Due to the generation and transport mechanisms of negative ions (see chapter 2.5.1) a variation of the current density distribution along the plasma grid is more likely to happen in vertical direction, because of the presence a vertical plasma drift in the source (see chapter 2.4.3). Obtaining and evaluating BES spectra from an vertical array of lines-of-sight will be a technique to measure the beam inhomogeneity as it is the case at ELISE and as it is envisaged for MITICA and SPIDER [98]. The definition of the beam inhomogeneity was already given in section 2.5.2.2 by equation (2.29). It considers the deviation of the extracted current density between the individual beamlets and should not exceed 10% (see section 2.3). Since the extracted current density does affect the beamlet divergence, an inhomogeneous beam is also reflected by an inhomogeneous divergence profile at the apertures.

In the following the principle feasibility of the reconstruction of the vertical divergence profile is investigated by assuming a certain vertical beam inhomogeneity as input for BBC-NI Simple calculations of BES spectra, although the error in the determination of the divergence for a single BES spectrum might be still to large (see section above). Hence, a case of a mean divergence of 2° was investigated as here the error is rather low. BBC-NI Simple is used, since it is not possible to reconstruct proper BES spectra with BBC-NI Advanced, yet (see section 5.3.4). For the following study two assumptions were made:

1. The current density is smoothly distributed along the vertical axis.
2. The extracted current at the edges can be either higher or lower. This results into a higher or lower divergence for the beamlets at the edges than for the central beamlets.

Since the divergence is an input parameter, its value was determined by a formula leading to a parabolic vertical divergence distribution at the apertures:

$$\epsilon_{\mathrm{s}}(z) = N_{\mathrm{p}} C z^2 + \epsilon \tag{5.11}$$

$\epsilon_{\mathrm{s}}(z)$ is the beamlet divergence for a beamlet at the vertical position z, N_{p} is the inhomogeneity parameter (i.e. it describes the bending of the parabola) with N_{p} being a simple integer, C being a constant and ϵ is the minimum, respective maximum divergence depending on the sign of N_{p}.

In twelve BBC-NI Simple calculations N_{p} was varied between -6 and 6 with $\epsilon = 2°$. The simulated spectra of the 16 vertical lines-of-sight were obtained and analysed.

Figure 5.21 shows two examples from these modeled cases: $N_{\mathrm{p}} = -1$ and $N_{\mathrm{p}} = -5$, i.e. a rather flat and a rather inhomogeneous divergence profile at the apertures. For the case of $N_{\mathrm{p}} = -1$ the reconstruction does not work well, while in contrast the reconstruction for the case $N_{\mathrm{p}} = -5$ is quite good. The standard evaluation overestimates the divergence in both cases as already shown in chapter 5.1.2. The shape of the profiles from the standard evaluation in a first glance seems to be in good agreement with the aperture profiles, however this might only be by chance for the two shown profiles. The divergence values obtained from the simulated BES spectra by the help of the parametrisation method show different behaviour for the two cases. For the flat aperture profile ($N_{\mathrm{p}} = -1$), the evaluated divergence values scatter widely around the input profile. In the case

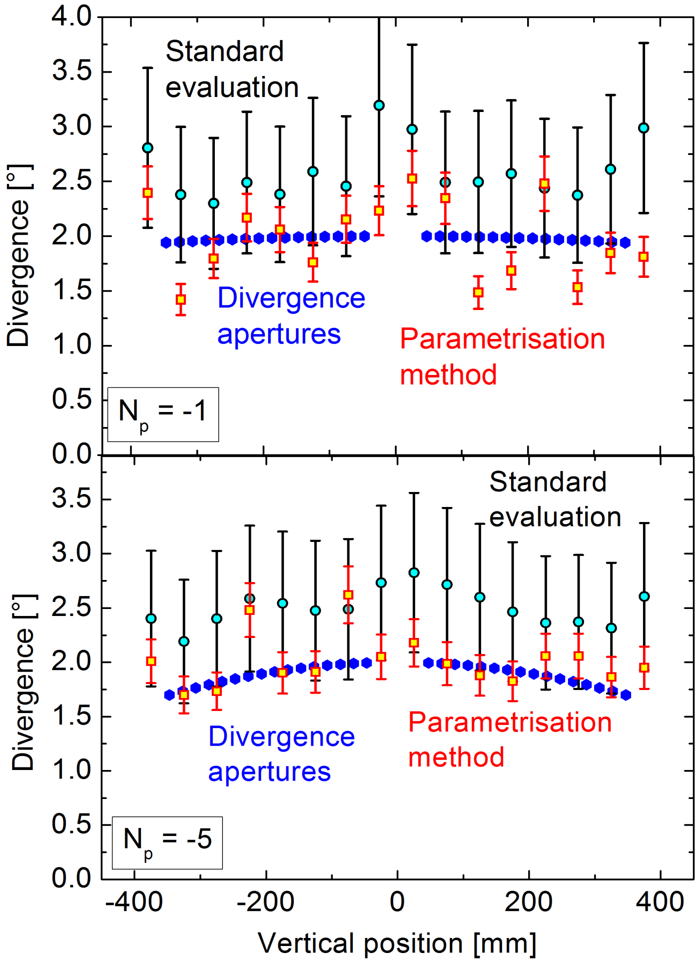

Figure 5.21: *Two assumed aperture divergence profiles at ELISE and the obtained divergence profiles from the vertical line-of-sight array with the two evaluation techniques.*

of $N_\mathrm{p} = -5$ the scattering is less pronounced and the input aperture divergence profile is predominantly reproduced by the parametrisation method.

However, looking at the error bars it can be already seen that a reconstruction of the input divergence profile (aperture profile) still is not possible. The error obtained at the divergence evaluation was presented in last section (see 5.1.2.5).

A more detailed analysis, which will be presented in the following, can emphasize the fact that a reconstruction of the aperture profile with the present methods is not possible. The BES divergence profile from the parametrisation method, where two profiles were already shown in figure 5.21, is fitted with a

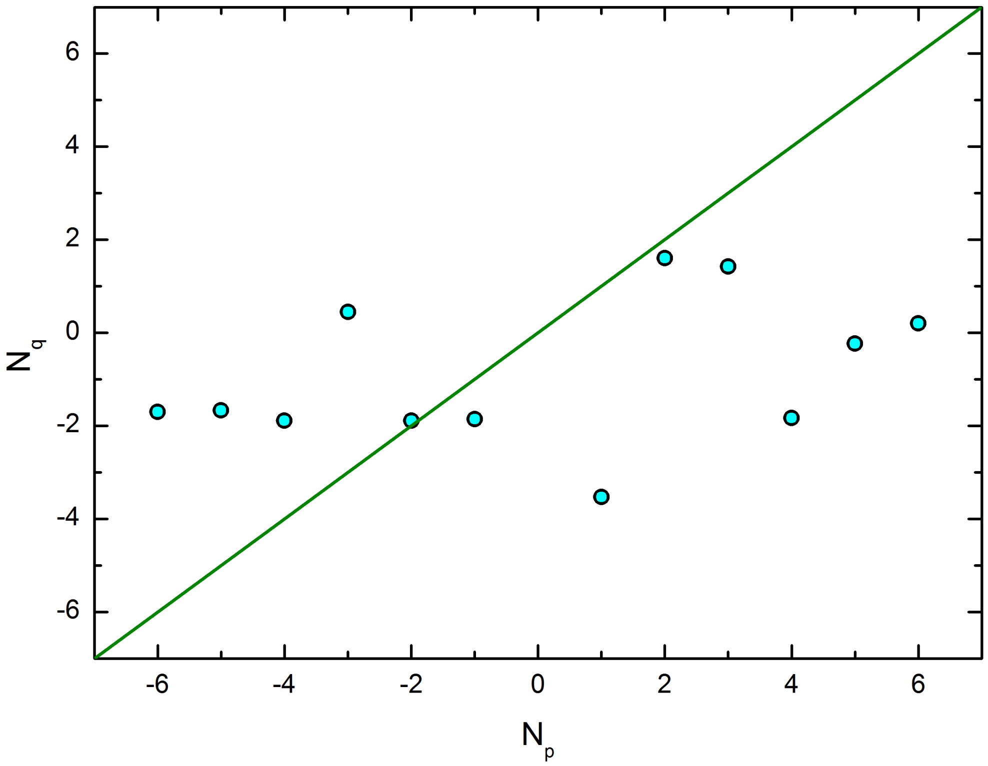

Figure 5.22: *Comparison between the inhomogeneity parameters of the aperture divergence profile* N_p *and the inhomogeneity parameter* N_q *of the fit from the BES divergence profile .*

simple parabola formula:

$$\epsilon_\mathrm{BES}(z) = N_\mathrm{q} C z^2 + \epsilon_\mathrm{m} \,. \tag{5.12}$$

$\epsilon_\mathrm{BES}(z)$ is the divergence depending on the vertical position z. C is again a constant as in equation (5.11) and N_q and ϵ_m are fit parameters, where N_q is representing the inhomogeneity parameter of the fitting curve. ϵ_m is the maximum, respectivly minimum divergence of the parabola fit of the BES divergence profile. Comparing N_p and N_q shows whether an aperture profile reconstruction is possible from the obtained divergences of the simulated BES spectra. Figure 5.22 shows the obtained correlation between N_p and N_q. A linear correlation would mean that the reconstruction of the input divergence profile, which is directly linked to the current distribution in front of the plasma grid apertures, is possible. In fact, due to the large error bars of the evaluated divergence values from the lines-of-sight even with the parametrisation method, the parabola fitting does more or less produce a flat line. Therefore, the reconstruction of the divergence profile at the apertures cannot be achieved with the current data evaluation of the BES system. As a consequence, as already mentioned, the evaluation error has to be minimised furthermore.

There are three solutions possible:

1. Improvement of the parametrisation method. Within the work of this thesis, the principle application of the parametrisation method was checked. Therefore the obtained fit function was kept simple. Up to now, the right side of the ELISE BES spectrum is fitted with a Lorentz function. However, in the case of low divergences, the main Doppler shifted peak is expected to be more Gaussian, since the origin-effect has only a minor role. A Voigt profile $V(x)$ described by the formula

   $$V(x) = y_0 + \frac{2Aw_\mathrm{L}\ln(2)}{\pi^{1.5}{w_\mathrm{G}}^2}\int_{-\infty}^{\infty}\frac{\mathrm{e}^{-t^2}}{\left(\sqrt{\ln(2)}\frac{w_\mathrm{L}}{w_\mathrm{G}}\right)^2+\left(\sqrt{4\ln(2)}\frac{(x-x_\mathrm{c})}{w_\mathrm{G}}-t\right)^2}\mathrm{d}t\,, \tag{5.13}$$

   might fit better to the shape of the Doppler shifted peak in any beam optics case, because a Voigt function is a superposition of a Gaussian and a Lorentz curve. y_0 is the offset variable, A is a dimensionless parameter and x_c is the center of the peak, w_G and w_L are two widths and t is a integral parameter. However, this would result into two values for the width representing the Doppler shifted peak. Generally, increasing the number of free parameters in a fit increases its quality. As a result the fitting of the Doppler shifted peak with a Voigt profile would lead to a standard deviation and a width-parameter. The two free variables parametrisation function would increase the complexity of the parametrisation technique.

2. Forward modeling of the BES spectra. For this method, the input parameters are chosen in a way, which leads to a good agreement of the obtained BES spectra from the calculation with the ones from a dedicated shot that is planned to be analysed. By adjusting the input parameters in consecutive steps, the agreement between calculation and measurement can be increased. At the end of this iterative approach, the assumed divergence profile for the simulation at the grounded grid is likely to be the realistic one.

   The advantage of this approach is a full database of all beam parameters for the specific pulse since they can be extracted from the simulation data.

However, in order to achieve successful forward modeling, the operator of the code has to know the input parameter very well. Additionally, a solution from the simulation which fits to the measurement might not necessarily be the best one. Other ones with different starting conditions but the same good agreement could refer to the realistic conditions more closely. It may only be separated by the help of additional diagnostic tools. This means for forward modeling, the experimental database of the whole diagnostic setup (e.g. calorimeter, grid currents,...) has to be taken into account.

3. The profile of the integrated Doppler emissivity obtained with the line-of-sight array depends also on the divergence and on the beam inhomogeneity. For determining this emissivity, the shape of the Doppler shifted peak is negligible. Only a calibration of the lines-of-sight is needed, which was done at ELISE. Comparing the obtained emissivity profile at ELISE with BBC-NI Simple calculations could give the possibility to determine a beam inhomogeneity. This method is also a version of forward modeling and will be done in a next step.

5.3 Beamlet homogeneity

Up to now, most of the results from BBC-NI calculations in this thesis were obtained with the BBC-NI Simple application. This means no consideration of electric and magnetic fields, all particles from one aperture start in the center and the velocity angle with respect to the beamlet axis is Gaussian distributed. The benchmarks on BES spectra obtained at BATMAN support this assumption. At ELISE the assumption of a Gaussian beamlet was only true for an operation scenario at relevant current densities and optimum normalised perveance conditions. However, the assumption of a Gaussian beamlet does not necessarily have to be valid. As it was shown in section 5.1.2, the magnetic and electric fields have a big influence on beam particle trajectories leading to “unexpected” BES spectra. Additionally TrajAn simulations indicate an inhomogeneous illumination of extraction aperture [70, 77], which can also influence the whole shape of the beamlet due to a different space charge distribution than it is the case for a homogeneous laminar flow of negative ions to the meniscus. Therefore the impact of these effects on the beamlet homogeneity has been studied for the ELISE grid system with BBC-NI Advanced simulations.

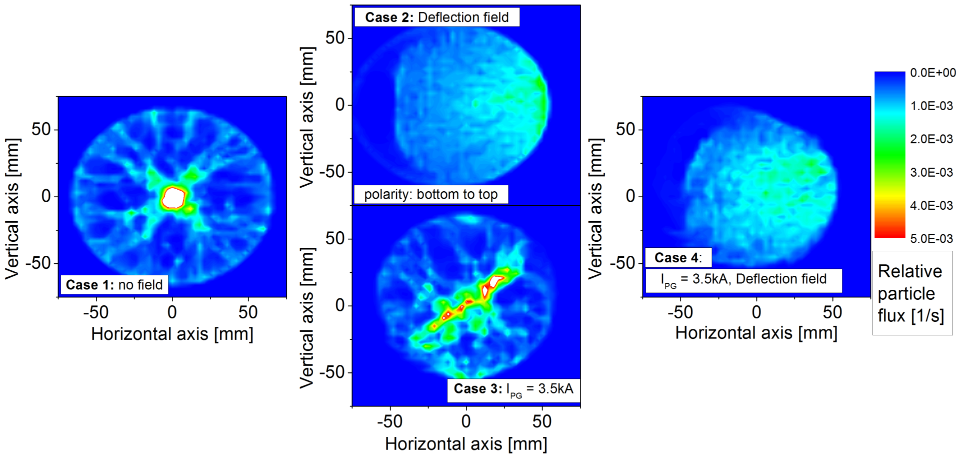

Figure 5.23: *Spatial flux distribution of a single beamlet at ELISE 0.6 m downstream the grounded grid with different magnetic field configurations.*

Beamlet homogeneity concerns the spatial particle flux distribution of a beamlet after the extraction system as well as the beam particle directions, which can be described by the distribution of the individual beam particle trajectory angle τ.

5.3.1 Influence of the magnetic field

As already explained in section 2.5.2.2, two magnetic fields are present in the extraction system, i.e. the filter field and the electron deflection field. Figure 5.23 shows the spatial ion flux distribution from a BBC-NI Advanced simulation of one single beamlet for four cases with no magnetic field present (case 1), each field individually (case 2 and 3) and the superposition of both magnetic fields (case 4) respectively. The input parameters refer again to pulse # 2764 at ELISE (see table 5.1 on page 91) without having caesium in the source, i.e. the extracted negative hydrogen ions are mainly generated by volume production and have their origin in the plasma bulk. The flow of negative ions to the meniscus therefore can be assumed to be laminar and spatially homogenous. The spatial particle flux distribution in figure 5.23 is taken about 0.6 m downstream the plasma grid. Case 1 shows the flux distribution of the beamlet with no magnetic field. As expected, it is very well focused and symmetric to the center where the highest flux is present, which is expected from the beam optics.

Adding only the deflection field (case 2) shifts the particle flux to the right side, due to the polarity of the magnetic field, as shown in the upper middle contour plot of figure 5.23. For a reversed polarity of the deflection field (which is present due to the alternating polarity in the aperture rows as explained in section 2.5), the shift would turn to the left side. The influence on the beamlet homogeneity by the magnetic filter field, generated by a current through the plasma grid (for case 3 it is 3.5 kA), can be seen in the lower middle contour plot. A band of high particle flux is formed with a prolongation from the upper right to the lower left. A simple horizontal magnetic field component would only shift the center, i.e. the position with the largest particle flux, upwards or downwards, depending on the field polarity. However the 3D shape of the real magnetic filter field leads to the observed particle flux distribution.

Having both magnetic fields present in the extraction system results in case 4 for the particle flux distribution. The influence on the beamlet homogeneity coming from the deflection field is higher than from the filter field. The particle flux distribution of the beamlet is completely different from the case without magnetic field. A functional description of the trajectory angle distribution, as it is done in BBC-NI Simple, is difficult for the case of the presence of magnetic fields.

Figure 5.24 shows the trajectory angle distribution for the two cases: with no magnetic fields and filter plus deflection field respectively. When no magnetic field is present, most of the particles have a very low trajectory angle τ. This results in the high particle flux in the beamlet center. Still, the trajectory angle distribution from this BBC-NI Advanced simulation is not symmetric and the maximum is not a trajectory angle of 0°. This is because of some numerical problems with the KOBRA3-INP electric field input. The reason is due to the beamlet formation calculated by KOBRA3-INP, which is not fully self-consistent like in PIC-codes and additionally, numerical artifacts occurring during the KOBRA3-INP simulation can have a slight influence on the symmetry of the trajectory angle distribution.

The maximum trajectory angle due to the solid angle of the aperture, determined by the grid geometry, would be at around ±9°. Due to the beam optics, the maximum trajectory angle is at ±6.2°. Taking the magnetic field into account changes this distribution. The shape is more smooth and the maximum is shifted to higher trajectory angles, because of the polarity of the deflection magnets.

Figure 5.23 and 5.24 show that the magnetic field in the extraction system can completely change the beamlet homogeneity. By chance, the assumption of a Gaussian trajectory angle distribution with BBC-NI Simple may fit to the

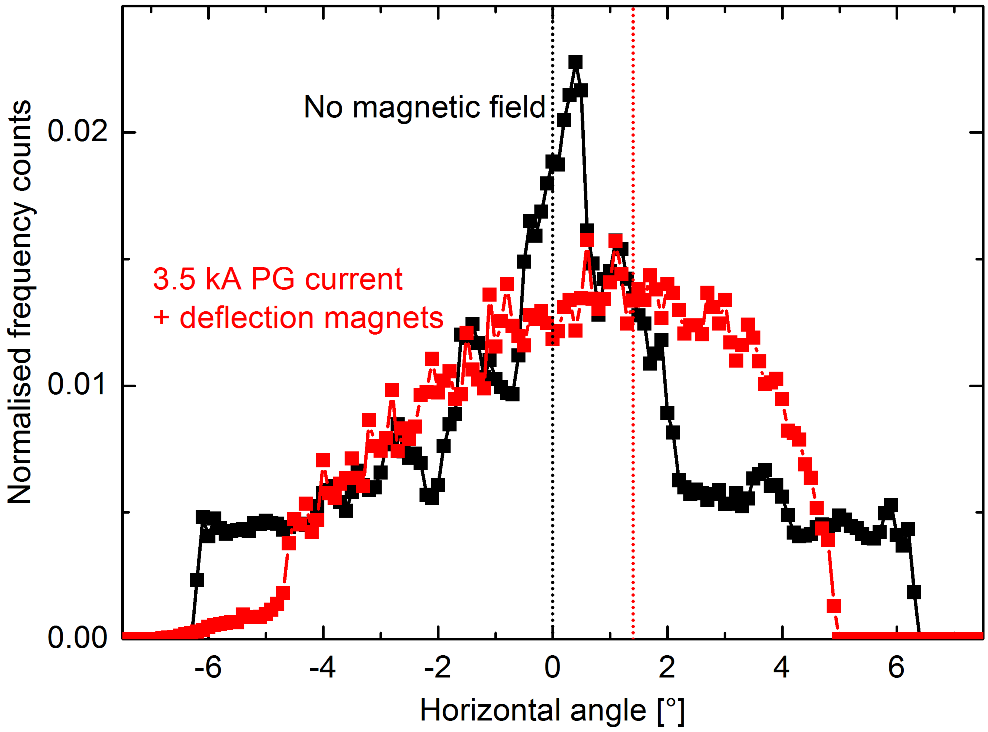

Figure 5.24: *Horizontal angular distribution of the beamlet particles for the case with no magnetic field and the magnetic field configuration at ELISE with a PG current of 3.5 kA.*

trajectory angle distribution of the realistic beamlet. This seems to be the case for BATMAN, since in the benchmark the BES spectrum could be reconstructed (see section 5.1.1.1). Dedicated beamlet homogeneity studies have to be performed though.

At ELISE the influence of the magnetic field changes the beamlet homogeneity in a way, that only for optimum normalised perveance conditions BBC-NI Simple is a valid model for the ELISE beam. This could be seen already in chapter 5.1.2. Apart from the optimum normalised perveance operation regime, BBC-NI Advanced with a realistic optic code has to be used for the simulation.

5.3.2 Influence of the electric field

The beamlet homogeneity is also influenced by the electric field. If there is a variation of the extraction and/or acceleration voltage with no magnetic field present, the beam optics are changed leading to different beamlet divergences. However the shape of the spatial particle flux distribution will stay rather constant. This

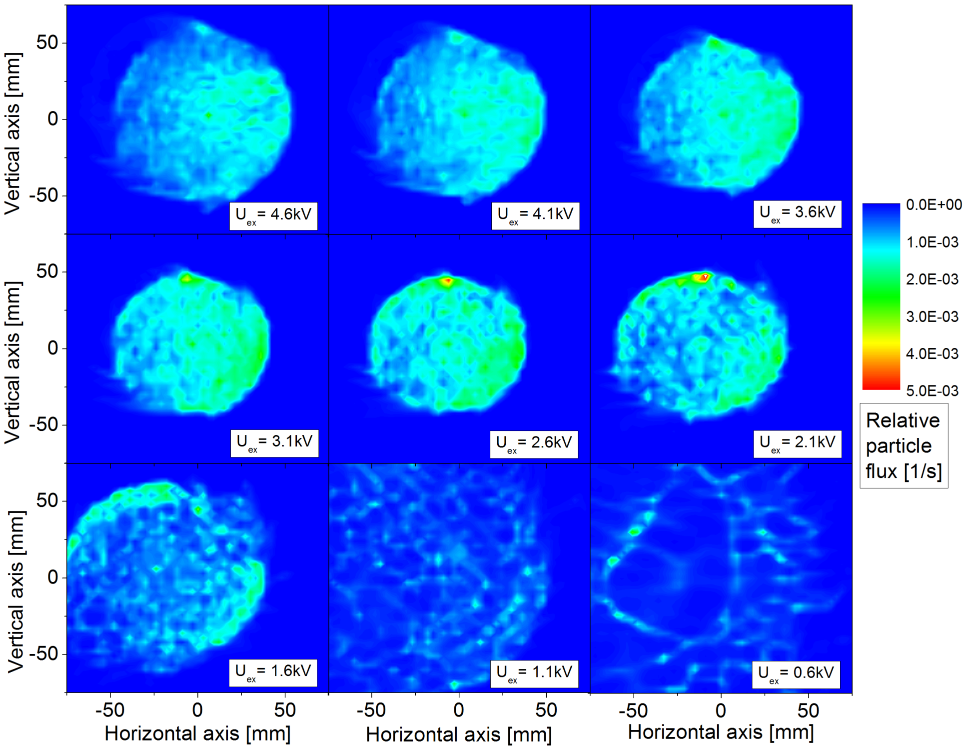

Figure 5.25: *BBC-NI Advanced calculations on the spatial negative ion flux distribution of a single beamlet at ELISE for different extraction voltages (affecting the normalised perveance), 0.6 m downstream the grounded grid. The full magnetic field configuration at ELISE is taken into account.*

means, most of the particles are in the beamlet center with a low trajectory angle τ.

When the magnetic field is taken into account, the influence of an electric field variation becomes complex too. Figure 5.25 shows the beamlet particle flux distributions for a variation of the extraction voltage. The underlying pulses are the same as for the perveance variation shown in figure 5.12. In the upper left contour plot the maximum of the spatial flux distribution is shifted to the right side. By decreasing the extraction voltage the area of a high particle flux is split up in two areas. For an extraction voltage of $U_{\mathrm{ex}} = 2.1\,\mathrm{kV}$, which is the normalised perveance optimum, they are located on the lower right and the upper left side.

The evolution of the spatial particle flux distribution clearly shows the big influence of the electric and magnetic field on the beamlet homogeneity. Due to the different electric field configuration, particles are led in different magnetic field regions. As a result, the variation of the beamlet homogeneity during a variation of the normalised perveance is a complex process.

The conclusion from this behaviour was already made up for the case of the magnetic field variation. By chance the assumption of a Gaussian trajectory angle distribution with BBC-NI Simple on the starting conditions may fit to the realistic beamlet homogeneity. However this might not be true in any case, which means BBC-NI Advanced has to be used in general.

5.3.3 Influence of asymmetric illumination

Beside the influence of the electric and magnetic field in the extraction system on the beamlet homogeneity, the starting conditions of the negative ions at the meniscus are also of importance. The distribution of the space charge at the meniscus and the transversal velocities have a big impact on the evolution of the beamlet shape in the extraction system.

Simulations which are performed with beam optic codes assume a laminar flow of the negative ions to the extraction aperture. As explained in section 2.5.2.1, this might be a good approximation in a caesium free source, where the negative ions are mainly coming from the plasma bulk. When the negative ion production happens on the plasma grid via the surface effect, the starting conditions are different. With the help of the code TrajAn (see chapter 4.3) the velocity components of the extracted particles at the meniscus have been determined. Additionally the code delivers the aperture illumination as shown in section 2.5.1. Since the negative ions have to come from the plasma grid surface around the extraction aperture the ions have a transversal velocity. Together with the space charge at the meniscus due to the inhomogeneous aperture illumination (see figure 2.11 in chapter 2.5.1) it is supposed to be the reason for some kind of beamlet halo or non-Gaussian beamlet shape (see section 2.5.2.2). The halo/non Gaussian beamlet particles with a relatively large divergence angle could be peeled off from the beamlet at the grounded grid aperture leading to the losses on it measured as the grounded grid current.

In KOBRA3-INP individual starting coordinates and velocities for every particle can be initialised. These input parameters are taken from the output of TrajAn (see section 4.3.3). Figure 5.26 shows the trajectory map with starting the conditions of the extracted negative ions, obtained from TrajAn. Every particle initialised for this calculation should be extracted. This is predicted by TrajAn and illustrated by the arrows. But it can be seen in the figure that many traject-

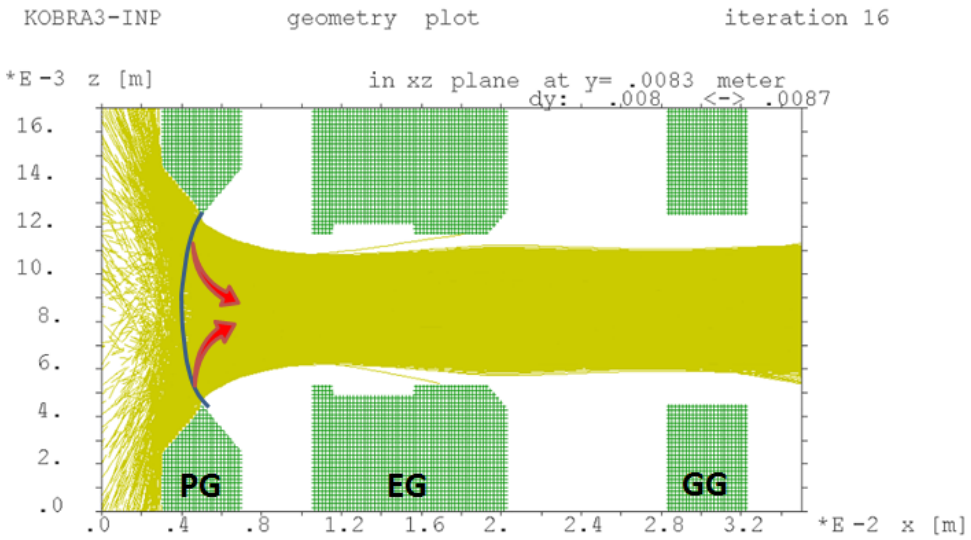

Figure 5.26: *Beamlet trajectories from a KOBRA3-INP simulation for BATMAN with the input of the starting conditions obtained from TrajAn. The parameters were* $U_{\mathrm{ex}} = 4.7\,kV$, $U_{\mathrm{acc}} = 13.1\,kV$ *and* $j_{\mathrm{ex}} = 275\,A/m^2$

ories lead back into the plasma. This means KOBRA3-INP cannot work properly with realistic input parameters for negative ions. Probably, the space charge map, build up in the code, leads to the back reflected particles. KOBRA3-INP has a rudimentary compensation module, simulating the plasma, building up the space charge map at the meniscus. The space charge compensation in the plasma in axial direction is Boltzmann distributed. The compensation degree can be adjusted by parameter variation, however it was not possible to reduce the back reflected particles. This indicates again that the plasma model in KOBRA3-INP like the models in other codes is not sufficient enough to take a non-laminar and perhaps more inhomogeneous flow of negative ions to the meniscus into account.

It should be mentioned here, that this problem might be less severe for the ITER NBI system, as here some “rectification” of the beamlet due to the acceleration to 1 MV appears. Simulations showed that for voltages of around 0.5 MV the calorimeter pattern from the beam could be reproduced very well [118].

5.3.4 Conclusion

In contrast to positive ion sources, the beamlet homogeneity in negative ion sources is much more complex. The beamlet homogeneity is determined by the electric and magnetic fields as well as by the aperture illumination. At least for

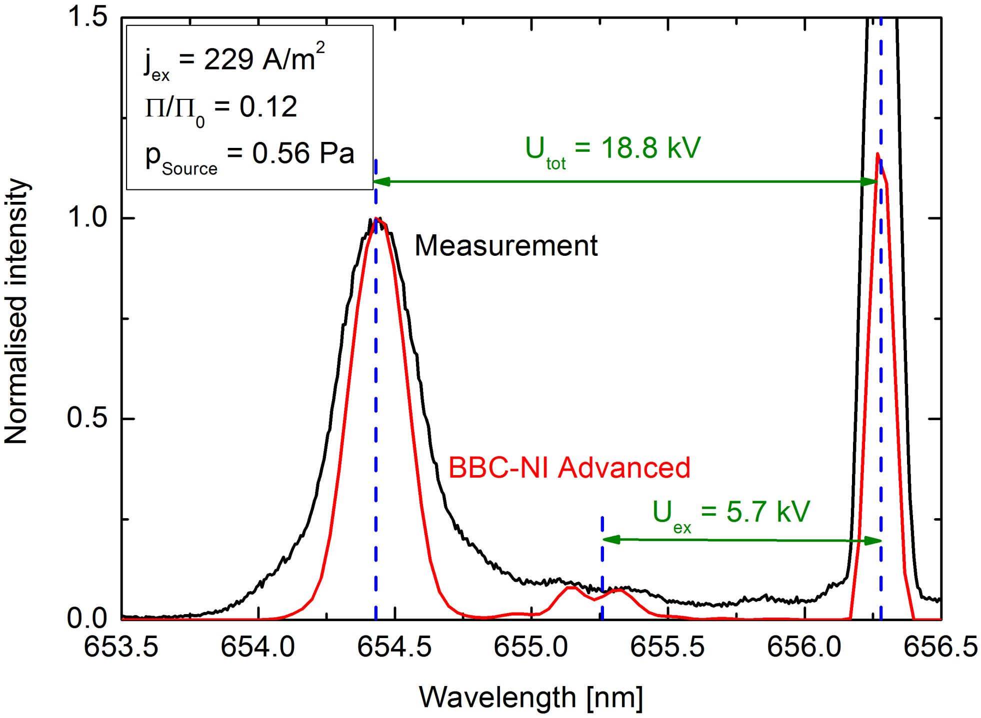

Figure 5.27: *Comparison of the measured BES spectrum at BATMAN with the simulated spectrum from BBC-NI Advanced. The broadening of the Doppler shifted peak in the simulation is less pronounced compared to the peak in the measurement.*

caesium free operation (i.e. a laminar flow of negative ions to the meniscus), simulations, for example with KOBRA3-INP, deliver valid results, where only the space charge compensation is a free parameter.

However, for the NBI system at ITER negative ions have to be generated by the surface effect, which needs a caesium coverage of the source walls. The currently available beam optic codes are not able to do a realistic simulation of this scenario. However, BBC-NI Advanced needs realistic electric field maps in the extraction system in order to be able to reconstruct BES spectra and power density profiles obtained at the large source at ELISE. In order to illustrate this problem, figure 5.27 shows a measured spectrum of the BATMAN pulse #84969 and a simulated spectrum from a BBC-NI Advanced calculation. The shift of the main Doppler peak and the stripping peak are in good agreement with the measurement. However, with BBC-NI Advanced and the respectively used KOBRA3-INP input, the broadening of the Doppler shifted peak and the stripping peak due to beam optics is heavily underestimated. With the electric field map from present beam optic codes like KOBRA3-INP, it is not possible to reconstruct realistic BES spectra obtained at negative ion sources for NBI.

New approaches by simulating the generation and extraction or the acceleration of negative ions self-consistingly with particle-in-cell codes (e.g. ONIX) may deliver these realistic electric field maps.

5.4 Stripping

A low beam inhomogeneity (see section 2.5.2.2) is important in order to minimise losses during the beam transmission to the fusion plasma. But also the stripping losses of the negative ions in the extraction grid system have to be minimised as far as possible in order to increase the source efficiency. Furthermore hydrogen atoms generated in the extraction system or hydrogen molecules from the H_2 background gas can be ionised by collisions and become backstreaming ions. These backstreaming can have severe damage to the source when their flux is too high (see chapter 2.5.2). This means, by the reduction of collision reactions and subsequently by the reduction of stripping losses, also the amount of backstreaming ions can be reduced.

The stripping losses depend on the density profile of the background gas in the extraction system as described with equation (2.28) on page 44. Because it is technically not possible to measure that profile it has to be described by dedicated models with proper assumptions, e.g. 3D Monte Carlo codes [22, 119]. For this thesis, for the sake of simplicity, the density profile is determined with the simple program Excelstrip [120], which describes the density profile quite well compared to the sophisticated codes. In Excelstrip, the H_2 temperature and the gas pressure (from gas pulses) in the source as well as the gas pressure in the tank are taken as input from the measurements. From that, the density profile together with the conductance of the grids is calculated as explained below. Figure 5.28 shows the results from this calculation.

The H_2 temperature in the plasma was determined from the Fulcher band, measured with optical emission spectroscopy [43]. It is around $(1200 \pm 100)\,\mathrm{K}$ for an ITER relevant source filling pressure of $0.3\,\mathrm{Pa}$. With increasing source filling pressure also the temperature increases (e.g. for $0.6\,\mathrm{Pa}$ it is $(1400 \pm 150)\,\mathrm{K}$) [43]. Although this temperature increase is not considered in the following BBC-NI Advanced calculation, it will be shown, that the plasma temperature has only minor effect on the stripping losses. The H_2 temperature in the tank is very

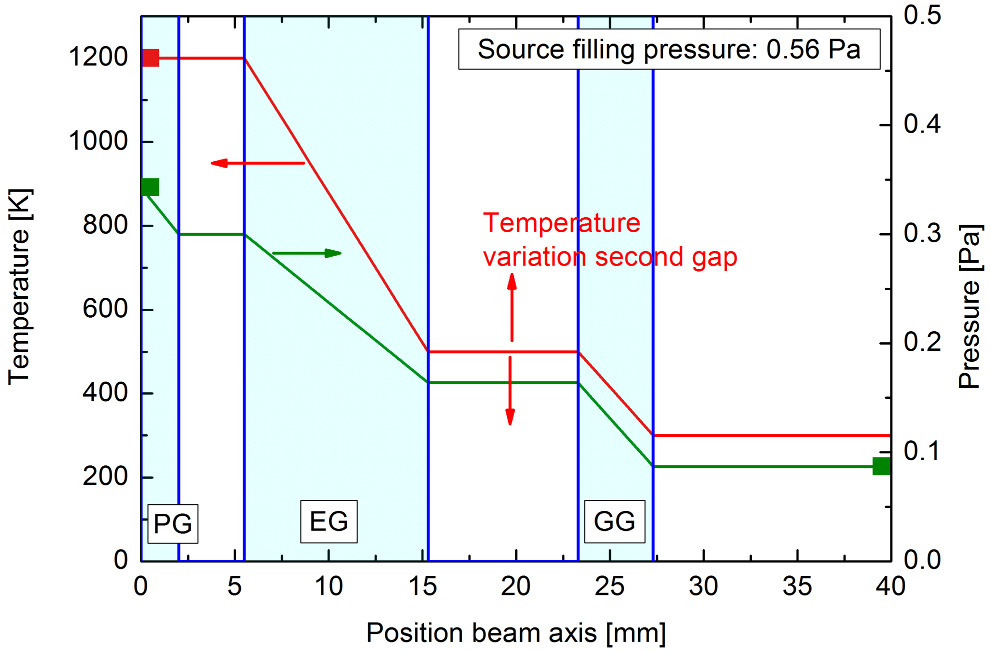

Figure 5.28: *Model of the pressure and estimated temperature profile in the extractions system of BATMAN. The values at the positions 0 mm and 40 mm on the beam axis are taken from measurements.*

likely to be room temperature. The pressure in the source is obtained by Baratron measurements while in the tank a Penning gauge is in operation. They measure the gas filling pressure, which is higher than the plasma pressure, due to the temperature of the heavy particles in the plasma. The positions of the pressure measurements are not close to the extraction system, which leads to a small error on the parameters that are shown in figure 5.28. The respective density profile for a background gas temperature in the second gap, which is exemplarily at 500 K, is shown in figure 5.29.

The temperature evolution in the grid system is determined by the temperature accommodation coefficient K_{ac} of the grids. This coefficient is defined as follows [22]:

$$T_{\mathrm{m1}} = T_{\mathrm{w}} + (T_{\mathrm{m0}} - T_{\mathrm{w}})(1 - K_{\mathrm{ac}})\,, \tag{5.14}$$

with T_{w} being the temperature of the respective grid surface and T_{m0} and T_{m1} being the "temperature" of a gas molecule before and after the collision with that surface.

The temperature distribution in the extraction system is calculated with the following assumptions:

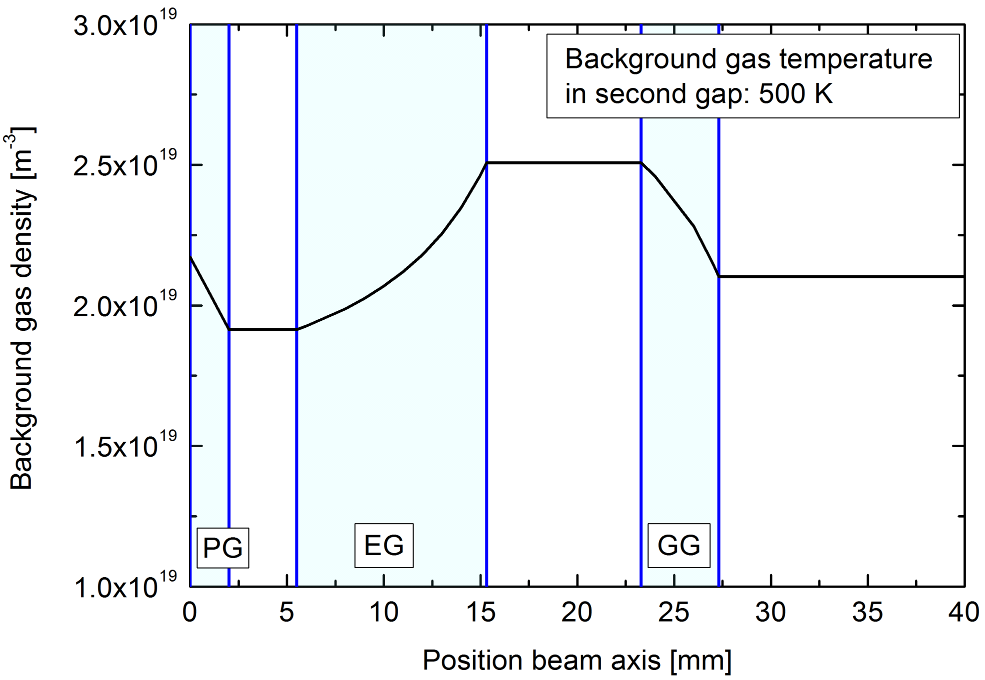

Figure 5.29: *Model of the density profile in the extraction system of BATMAN with a background gas temperature in the second gap of 500 K.*

1. The temperature is constant within the gaps.
2. The temperature decreases linearly within an aperture, because of collision of gas particles with the wall.

The gas temperature in the second gap is a free parameter for the setting of the temperature profile. The calculations from BBC-NI Advanced presented in this chapter will also predict a value for this temperature. However the main aim of these calculations is to enhance the evaluation of the stripping losses from a BES spectrum as it will be shown in this section.

With a certain temperature profile, the pressure evolution is calculated by text book formulas [121]. The assumption for the pressure is a linear decrease within the grid apertures, a constant pressure in the grid gaps and no additional lateral gas losses. This can be described by the formula

$$p_{\mathrm{a,d}} = p_{\mathrm{a,u}} - \frac{\Gamma}{L_{\mathrm{a}}}\,, \tag{5.15}$$

where $p_{\mathrm{a,d}}$ is the pressure downstream of one aperture and $p_{\mathrm{a,u}}$ refers to the upstream pressure. Γ is the gas flow and L_{a} the conductance of the aperture. However this equation is only valid for equal temperatures upstream and downstream the grid. For the sake of simplicity this was assumed, however it is probably not the case, leading to a calculated density profile in the grid system which has some deviation from reality. This error might be not too large, as a comparison of the model from Excelstrip with the ITER calculations showed a maximum deviation of 20%.

The conductance of one aperture is calculated by using the formula for circular tubes:

$$L_{\mathrm{a}} = \frac{\bar{c}}{4} A_{\mathrm{a}} \left(1 + \frac{3 l_{\mathrm{a}}}{8 r_{\mathrm{a}}}\right)^{-1} , \tag{5.16}$$

A_{a} being the aperture area, r_{a} the radius and l_{a} the aperture length. The mean gas velocity $\bar{c}$ can be written as:

$$\bar{c} = \sqrt{\frac{8 k_{\mathrm{B}} T_{\mathrm{g,a}}}{\pi m}} , \tag{5.17}$$

with $T_{\mathrm{g,a}}$ as the background gas temperature and m is the mass of the gas particles. k_{B} is the Boltzmann constant. $T_{\mathrm{g,a}}$ is an average temperature, obtained from the background gas temperature upstream and downstream of the respective grid. This reduces the error from equation (5.15).

The total gas flow is calculated with the conductance $L_{\mathrm{a},i}$ of an aperture a from grid i, the source pressure p_{source} and the tank pressure p_{tank}:

$$\Gamma = N_{\mathrm{a}} \left(\sum_i L_{\mathrm{a},i}^{-1}\right)^{-1} \left(p_{\mathrm{source}} - p_{\mathrm{tank}}\right) , \tag{5.18}$$

N_{a} being the number of apertures. The total gas flow from the source to the tank can be obtained from the pressure measurement in pure gas pulses. During plasma phases the H_2 gas flow through one aperture is reduced because of the dissociation degree which is around 10% [43]. Since the negative ion source is operated with a constant gas flow, the source pressure is reduced because the conductance increases with higher gas temperature, which is the case in plasma operation. From the temperature and the pressure profile the H_2 density in the extraction system is calculated. Figure 5.29 shows such a density profile exemplarily.

The stripping losses can be measured by BES only. As explained in chapter 3.2 this is done by the ratio of the integral of the Doppler shifted peak and the stripping peak (equation (3.11)). In the standard evaluation the integral borders for the stripping peak are chosen by reasonable assumptions: The cross section of reaction (2.21) has its maximum around 5 keV/amu. This is comparable to the ion energy at the beginning of the extraction grid. At this position the density of the background gas still is very high. Therefore most of the stripping occurs in this region. This results into the clear formation of the stripping peak in the BES spectrum (see figure 5.27). In order to take the Doppler broadening into account, in the standard evaluation the integral borders are set ±0.25 nm around the wavelength (see this practice in figure 3.9 on page 57) which corresponds to the extraction voltage.

For the simulation on the stripping losses, BBC-NI Advanced has to be used. For a plasma temperature of 1200 K and 1000 K respectively, the gas temperature in the second gap was varied in 100 K steps down to room temperature.

BBC-NI Advanced generated a BES spectrum, which was then analysed with the standard evaluation leading to a value for stripping losses. However, since the emissivity of radiating stripped particles is obtained by setting the integral borders to ±0.25 nm, the evaluated stripping losses might be underestimated. This is because photons from stripped particles with a high energy (comparable to the full accelerated particles) are not in the wavelength range of the stripping peak. BBC-NI records if a stripping collision occurs for every single H^-. This is counted up leading to the total value for the stripping losses in the simulation.

Figure 5.30 shows the results from the BBC-NI Advanced calculations. The underlying pulse parameters were $U_{\mathrm{ex}} = 5.7\,\mathrm{kV}$, $U_{\mathrm{acc}} = 13.1\,\mathrm{kV}$, $j_{\mathrm{ex}} = 229\,\mathrm{A/m^2}$ and a source filling gas pressure of $p_{\mathrm{source}} = 0.58\,\mathrm{Pa}$ referring to the BATMAN pulse #84969 (see figure 5.27). The full dotted points show the total stripping losses, counted up by the code. The values in the figure are therefore labeled with "Counter". With a lower gas temperature downstream the extraction grid, i.e. a larger H_2 density, the stripping losses increase exponentially. The difference in the H_2 gas temperature in the source does not have a large effect on the stripping losses.

In a second step, the simulated BES spectra are evaluated by the standard evaluation. The results on the stripping losses from this evaluation are lower than the total losses in the code. The stripping losses obtained from the stimulated spectra are indicated with the open dots. They can be compared to the experimental data of the shot which is underlying to these calculations. The blue horizontal lines indicates the stripping losses obtained from the measured BES spectrum in the experiment. The line crosses the exponential fit of the stripping losses determined by the simulated BES spectra between 400 K and 500 K. From

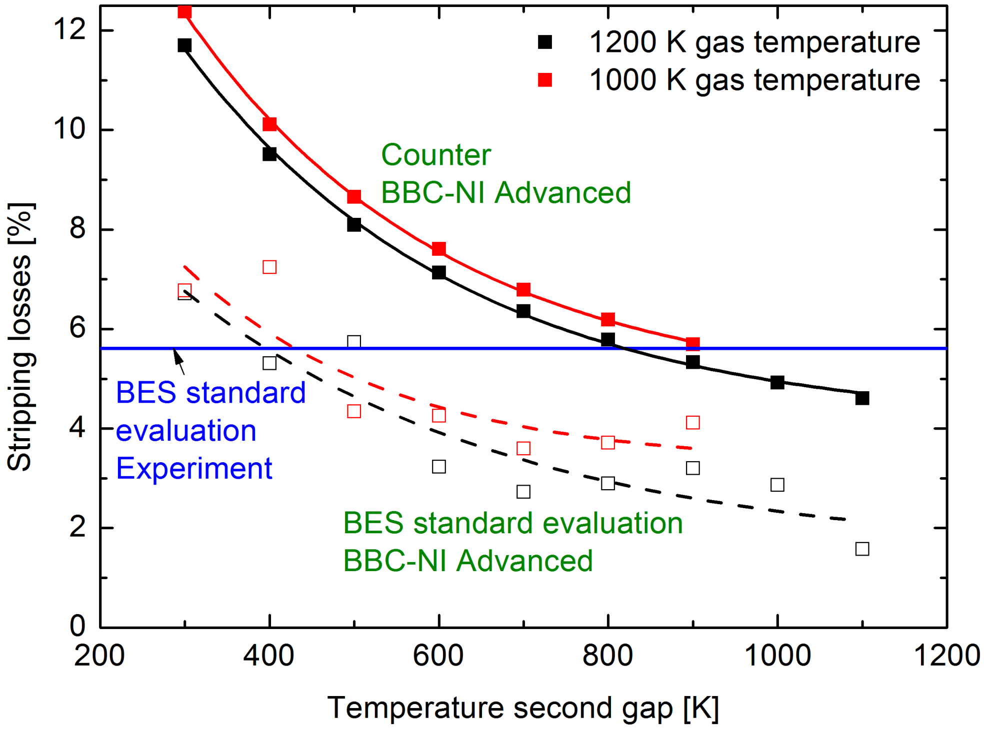

Figure 5.30: *Stripping losses for two H_2 gas temperatures in the source, obtained from BBC-NI Advanced calculations, for the variation of the temperature in the second gap of the extraction grid. Additionally the stripping losses measured by BES from the experimental shot, underlying to the calculation, is marked as a horizontal line. The normalised perveance of the used pulse is 0.12.*

the modeling two basic results can be drawn:

1. The stripping losses obtained from the standard evaluation of the BES spectrum clearly underestimate the predicted total losses. In this example the total stripping losses are about 2 times higher due to considering the high energetic stripped particles. This is shown by figure 5.31 for a BBC-NI Advanced calculation referring to the same BATMAN pulse # 84969. The gas temperature in the plasma for this calculation was set to 1200 K and the background gas temperature in the second gap was at 500 K according to the results above. In the figure, the relative amount of detected photons separated by the energy of the radiating stripped particles is presented. The histogram shows that a BES spectrum contains contributions of photons from stripped particles in the whole energy range up to the energy related to the total voltage of $U_{\text{tot}} = 18.8\,\text{kV}$. However, due to the standard evaluation of the stripping peak (with the fixed integral borders), only

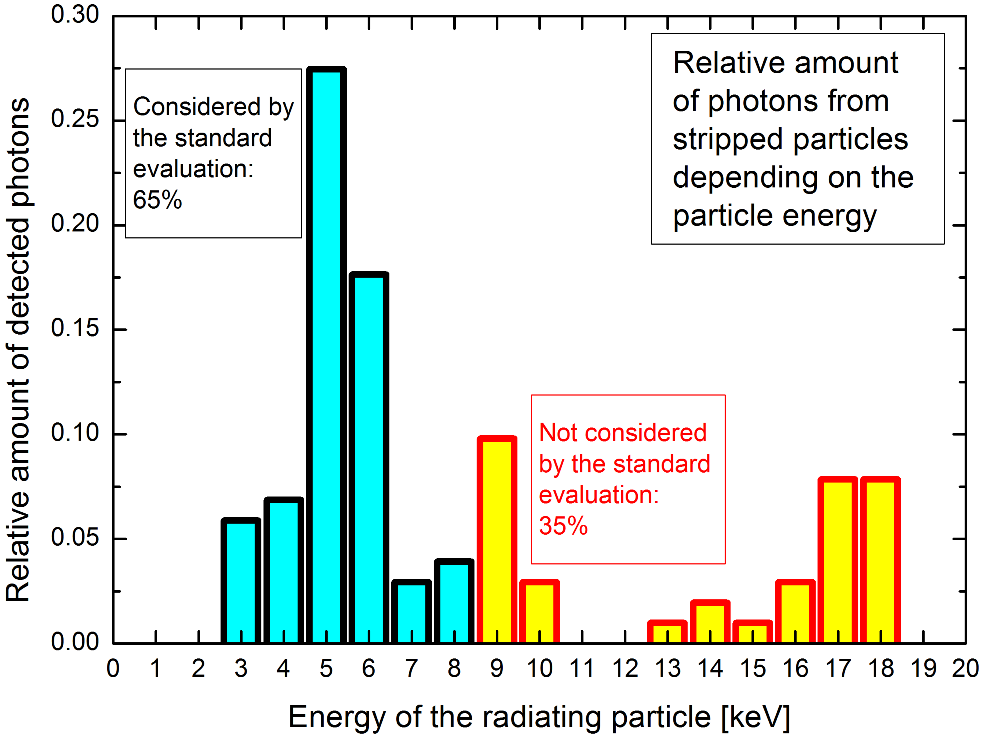

Figure 5.31: *Relative amount of detected photons from stripped particles, separated by their energy. For the determination of the stripping peak in the standard evaluation, only a certain energy range is considered indicated by the blue bars. In this case photons from radiating stripped particles with an energy* $> 8\,keV$ *are not considered in the standard evaluation. This refers to 35 % of the detected photons from stripped particles. The extraction voltage was* $5.7\mathrm{kV}$.

a part of the photons are considered by the evaluation, in this case only 65%. Photons which are emitted by high energetic particles (in this case $> 8\,\mathrm{keV}$), which have had a stripping reaction after the extraction grid at higher velocities, contribute to the main Doppler shifted peak. Hence, the separation between the amount coming from stripped particles and from fully accelerated particles in this wavelength region in the spectrum is quite difficult. A fast enhancement could be the fitting of the Doppler shifted peak, only taking the one side of the peak into account, namely the one which is not influenced by photons from stripped particles. Subtracting this fitted peak from the spectrum leaves only the spectrum coming from stripped particles. The two integrals which are necessary for the evaluation of the stripping losses can be taken from the subtracted spectrum and the fit of the Doppler shifted peak.

However, as already shown in chapter 5.1.1 and 5.1.2, the Doppler shifted peak is not necessarily Gaussian. This means also the stripping losses which would come from an enhanced standard evaluation have a notable error. But it would be at least smaller since the part of high energetic stripped particles would be increasingly taken into account.

A second more precise method would generate a BES spectrum with BBC-NI Simple, where the simulated Doppler shifted peak fits good to the measured one. Again, a substraction of the simulated peak from the measurement would lead to the spectrum coming from stripped particles. The error of the obtained value for the stripping losses would be smaller compared to the fitting method. This is due to the more precise reproduction of the Doppler shifted peak from the simulation than from the Gaussian fit.

2. The gas temperature after the extraction grid is around 500 K. This means a low temperature accommodation coefficient K_{ac} within the extraction grid. As a result, the density of the background gas in the gap between extraction grid and grounded grid is comparatively large since the gas temperature is close to room temperature. A decrease of this density could also decrease the stripping losses and subsequently also the backstreaming ions. The decrease of the stripping losses could be achieved by minimising the source filling pressure as far as possible while still having an ITER relevant negative ion current.

Furthermore the validity of the density profile predicted from the BBC-NI Advanced simulations can be confirmed by the BES spectrum obtained from the calculation.

Finally, figure 5.32 shows the simulated and respective measured spectrum from one BES channel for the case 1200 K gas temperature in the source and 500 K background gas temperature downstream the extraction grid. The beam optics determined by KOBRA3-INP are not fully correct. The reason for this was already discussed in detail in the last section. For the spectrum from BBC-NI Advanced this means that every peak in it is narrower than it should be in reality.

The stripping peak in the measurement is not clearly separated, however it is present and shows a hint of a double peak. With the density profile for the simulation, this double peak structure can be reproduced. Imagining a broadening of the peaks in the simulated spectrum, due to the use of a correct potential map, one could imagine a very good reconstruction of the measured spectrum.

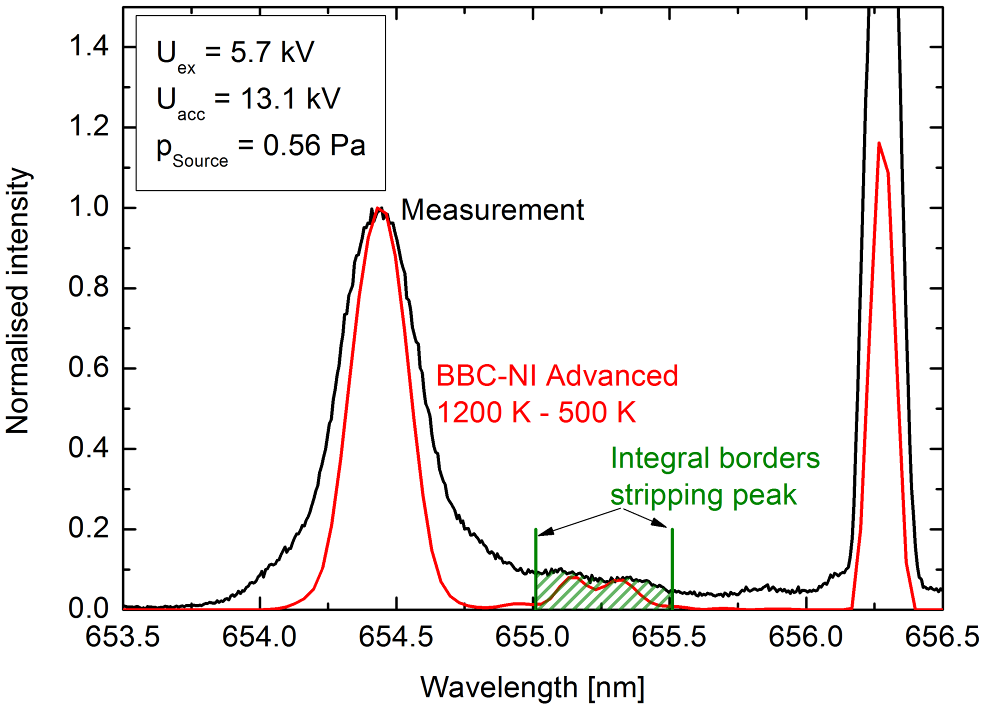

Figure 5.32: *Comparison of the measured BES spectrum at BATMAN with the simulated spectrum from BBC-NI Advanced. The agreement for the stripping losses is at a optimum for the given temperature profile.*

The discrepancy in the stripping losses between the model and the measurements described in section 2.5.2.2 might be explained by the error made in the standard evaluation, but also from a density profile which is not realistic enough. With the obtained results the deviation between model and measurement might be decreased in future investigations. The achievement of the obtained results was only possible, due to the large Doppler shift, provided by the design of the BES system, especially at ELISE. This allows a clear separation of the stripping peak from the Doppler shifted peak and the unshifted H_α peak in the range of the perveance optimum. However at SPIDER, the BES observation angle will be close to 75° and at MITICA even 85° [98]. This will smear the three peaks to one complex peak since the development of the Doppler shift is small and the spectrum will be even more difficult to analyse.

6 Summary

The main goal was to provide a tool for the determination of the beam properties of the large half ITER size ($1\,\mathrm{m} \times 0.86\,\mathrm{m}$) negative hydrogen ion source at ELISE. This is the trajectory code BBC-NI which has been developed within this thesis. It is able to simulate the whole beam from the extraction to the calorimeter including beam diagnostic tools and the outcome of their measurements. The desired beam properties are the beam divergence, the beam inhomogeneity and the stripping losses. With beam emission spectroscopy (BES) the H_α light of the beam was measured spatially resolved with an vertical array of 16 lines-of-sight. By obtaining the averaged divergence from each spectrum, a vertical divergence profile of the beam can be obtained. In optimum normalised perveance conditions, this profile correlates with the extracted current density distribution at the front of the plasma grid, which cannot be measured directly. In order to investigate the possibility of reconstructing the current density distribution at the plasma grid from BES spectra, BBC-NI came into operation.

With the help of BBC-NI Simple the formation and the quality of the beam parameter evaluation of a BES spectrum at small and large negative ion sources for NBI has been investigated. Subsequently the results from this task were applied on the reconstruction of the vertical current density distribution at the plasma grid. Finally, the evaluation of the stripping losses, which are important for the beam power losses and the amount of backstreaming ions, was analysed.

The standard evaluation of the Doppler shifted peak, i.e. a Gaussian fit of the Doppler shifted peak, in order to determine the line-of-sight averaged beam divergence originates from positive ion sources. This is a backward calculation of the beam divergence from the measured spectrum. The analysis of the Doppler shifted peak in negative ion sources is much more complex. This is due to the presence of the magnetic fields and the source size, because negative ion sources are larger than positive ions due to the achievable extracted current density.

With BBC-NI Simple the formation of the Doppler shifted peak in a BES spectrum was analysed in detail. In small sources, like the ITER prototype source at BATMAN or smaller, the reconstruction of the measured Doppler shifted peak by BBC-NI simulation was achieved. Several geometrical effects lead to the bell-shaped peak. These effects are the area- and angle-effect as well as the origin-effect.

In the large ion source (with several hundred apertures) at ELISE, depending on the perveance, a more complex deformation of the Doppler shifted peak was observed. This might come from the magnetic field (filter and electron deflection field) together with the electric field in the extraction system. Furthermore, the trajectories can be influenced by an inhomogeneous illumination of the extraction aperture, that might be present. The beamlet spatial flux distribution is no more Gaussian shaped as it is the case in positive ion sources but much more intricate in the directional and spatial flux distribution of the beamlet particles. This leads to the complex BES spectra.

The backward evaluation of the divergence from such a spectrum is not possible anymore. With larger size and number of apertures, the influence of the geometric effects increases, which makes the evaluation of the spectrum even more difficult. However, operating the negative ion source in the normalised perveance optimum leads to a less or not at all deformed Doppler shifted peak which can be treated with the standard evaluation of a BES spectrum. BBC-NI Simple simulations for a BES spectrum obtained at ELISE in optimum perveance conditions show a beam divergence between 1° and 2°, which is in the range of the design value.

Still, the divergence can be measured with less error by a new evaluation which is called the parametrisation method. Here, one side of the Doppler shifted peak is fitted by a Lorentz curve. With a relatively simple method for the parametrisation of the Lorentz curve, which was contrived within this thesis, the error of the divergence evaluation could be reduced. While the error of the standard evaluation for BES spectra in the large source at ELISE is always above 10%, the parametrisation method reaches an error of less then 10% for divergences larger than 1.5°. For a smaller divergence, the results from the parametrisation method have an error below 30% which is significantly lower than for the standard evaluation in this divergence regime. However, for a determination of the beam inhomogeneity, an error of a least 5% is necessary. The development of the parametrisation method was only possible due to the better understanding of the formation of the Doppler shifted peak due to the geometric effects.

Assuming a reasonable inhomogenous beam, simulated ELISE BES spectra were evaluated with the parametrisation method in order to check the possibility of a reliable reconstruction of the input divergence profile. It was found out that a reconstruction is not possible. The error of the divergence evaluation even with the new parametrisation method is still too large. The reason is due to the fit function of the Doppler shifted peak, which is still not adequate yet, i.e. the squared deviation between Doppler shifted peak and fit function is too large. This means, the determination of the beam inhomogeneity at ELISE, solely with the BES system is not possible. Furthermore, when operating ELISE in the perveance optimum a variation of the extracted current density has only a marginal effect on the divergence, due to the beam optics design. Therefore an inhomogeneous current density distribution in front of the plasma grid is hardly visible in the divergence profile.

In source operation it has been observed that stripping losses obtained by BES measurements showed smaller values ($\approx 3\%$) as predicted by models ($\approx 8\%$). In order to find the reason for this deviation the evaluation of the stripping losses from BES spectra has been investigated in this thesis. Several BBC-NI calculations with different density profiles in the extraction system were performed. The outcome of the evaluated simulated BES spectra were compared with the evaluations from the underlying pulse. The density profile of the extraction system from the calculation which had the best agreement on the evaluated stripping losses compared to the experimental results could be a very close indication to the real profile, which cannot be measured directly. Additionally, the calculation shows a discrepancy between the stripping losses evaluated by the simulated BES spectrum and the total stripping losses occurring in the simulation. The standard evaluation of the stripping losses underestimates the total losses by a factor of about two. This is in the order of the deviation for the stripping losses between measurement and model. The reason is due to the high energetic stripped particles which cannot be neglected. The strong presence of the high energetic stripped particles is due to the relatively large background gas density in the gap between extraction and grounded grid and high cross sections for the stripping reactions a particle energy related to the extraction voltage. The radiation of these particles does not contribute to the stripping peak but to the Doppler shifted peak, i.e. the stripping peak (coming from not fully accelerated radiating beam particles) and the main Doppler shifted peak (coming from fully accelerated radiating beam particles) have an overlap. Therefore the high energetic stripped particles are not taken into account by the evaluation of the measured BES spectra since the deconvolution of the Doppler shifted peak is almost impossible.

The main results are, that first of all, the evaluation of the beam divergence from a BES spectrum was improved with the parametrisation method. Furthermore it turned out that the evaluation of stripping losses and beam inhomogeneity in large negative hydrogen ion sources cannot be performed by backward calculations from a BES spectra, i.e. by the analysis of the spectra. This means forward modeling has to be done, which does also include the simulation of other beam diagnostic tools, like the power density profile measured by the calorimeter. Combining all beam diagnostic tools and reconstructing their outcome with a BBC-NI Advanced simulation, gives the possibility to determine the beam parameters by extracting them from the BBC-NI code protocols. This requires a lot of effort and is not well suited for a routine analysis.

For ITER this means that solely a BES system for the determination of the beam parameters (i.e. stripping losses and beam inhomogeneity), as it is presently foreseen, is not sufficient. Several beam diagnostic tools, e.g. the calorimeter which can determine the power density profile of the beam, and a code like BBC-NI are necessary. Additionally for the application of BBC-NI Advanced, a beam optic code is needed, which is able to generate a realistic electric field map in the extraction system. Such an optic code is not available so far.

Appendix

A Error discussion on the beam inhomogeneity

For the derivation of the error of the beam inhomogeneity it is assumed that the beamlet current density j_k, of the clearly defined beamlet k, has the maximum deviation from the averaged beamlet current density from N apertures. Thereby j_i is the beamlet current density from beamlet i, with $i \in [1, N] \setminus \mathrm{k}$. Equation (2.29) on page 46 can then be written as:

$$\Upsilon = \frac{(N-1)j_\mathrm{k} - \sum_{i=1,i\neq k}^{N} j_i}{\sum_{i=1}^{N} j_i} \,. \tag{6.1}$$

The maximum error $\Delta\Upsilon$ is defined as

$$\Delta\Upsilon = \sum_{i=1}^{N} \left(\Delta j_i \frac{\partial \Upsilon}{\partial j_i} \right) \,, \tag{6.2}$$

with Δj_i being the error of the current density measurement from beamlet i. Equation (6.2) becomes:

$$\begin{aligned} \Delta\Upsilon = & \underbrace{\Delta j_\mathrm{k} \frac{(N-1)\sum_{i=1}^{N} j_i - \left[(N-1)\, j_\mathrm{k} - \sum_{i=1,i\neq k}^{N} j_i\right]}{\left(\sum_{i=1}^{N} j_i\right)^2}}_{S_1} \\ & + \underbrace{\sum_{j=1,j\neq k}^{N} \Delta j_j \frac{\sum_{i=1}^{N} j_i - \left[(N-1)\, j_\mathrm{k} - \sum_{i=1,i\neq k}^{N} j_i\right]}{\left(\sum_{i=1}^{N} j_i\right)^2}}_{S_2} \,. \end{aligned} \tag{6.3}$$

The first summand S_1 can be written as:

$$S_1 = \Delta j_\mathrm{k} \frac{N \sum_{i=1,i\neq k}^{N} j_i}{\left(\sum_{i=1}^{N} j_i\right)^2} \,. \tag{6.4}$$

For large N, and for small deviations of j_i from the average beamlet current density, which is the case for a beam with a beam inhomogeneity of 10%, it can be approximated that $\sum_{i=1,i\neq k}^{N} j_i \approx \sum_{i=1}^{N} j_i$. Equation 6.4 can be eased to

$$S_1 = \frac{\Delta j_\mathrm{k}}{\frac{1}{N}\sum_{i=1}^{N} j_i} \,. \tag{6.5}$$

The second summand S_2 can be approximated by assuming $\Delta j_i = \Delta j_\mathrm{k}$. This case leads to the largest possible error, because by definition j_k should have the maximum deviation from the averaged beamlet current. S_2 can be written as:

$$S_2 = N\Delta j_\mathrm{k} \frac{2\sum_{i=1}^{N} j_i - (N-2) j_\mathrm{k}}{\left(\sum_{i=1}^{N} j_i\right)^2} \,. \tag{6.6}$$

For a low beam inhomogeneity with Υ being less then 10% it can be assumed that $j_\mathrm{k} \approx j_i \ \forall i$. For a large N, this means that $\sum_{i=1}^{N} j_i \approx (N-2) j_\mathrm{k}$. The second summand can then be written as

$$S_2 = \frac{\Delta j_\mathrm{k}}{\frac{1}{N}\sum_{i=1}^{N} j_i} \,. \tag{6.7}$$

As a result equation (6.3) is simplified to

$$\Delta\Upsilon = 2\frac{\Delta j_\mathrm{k}}{\frac{1}{N}\sum_{i=1}^{N} j_i} \,. \tag{6.8}$$

For an ITER relevant beam inhomogeneity of 10%, $j_\mathrm{k} = 1.1\frac{1}{N}\sum_{i=1}^{N} j_i$ respectively $j_\mathrm{k} = 0.9\frac{1}{N}\sum_{i=1}^{N} j_i$, the relative error of the current measurement for j_k is either $\frac{\Delta\Upsilon}{2\cdot 1.1}$ or $\frac{\Delta\Upsilon}{2\cdot 0.9}$, which is both approximately $\frac{\Delta\Upsilon}{2}$. This means for a relative error of Υ being 10%, the current density measurement has to have a relative error less than 5%.

Bibliography

[1] ITER-Director, ITER-FEAT - outline design report, *Tech. rep.*, ITER Organisation (2000).

[2] K. Tokimatsu, J. Fujino, S. Konishi, Y. Ogawa, K. Yamaji, *Role of nuclear fusion in future energy systems and the environment under future uncertainties*. Energy Policy **31** (8), 775 (2003).

[3] U. Fischer, H. Tsige-Tamirat, *Activation characteristics of a solid breeder blanket for a fusion power demonstration reactor*. J. Nucl. Mat. **307** (0), 798 (2002).

[4] K. Brodén, R. Edwards, M. Lindberg, P. Rocco, M. Zucchetti, *Waste from fusion reactor: A comparison with other energy producing systems*. Fusion Eng. Des. **42** (1), 1 (1998).

[5] J. Sheffield, *The physics of magnetic fusion reactors*. Rev. Mod. Phys. **66**, 1015 (1994).

[6] A. Harms, K. Schoepf, G. Miley, D. Kingdon, *Principles of fusion energy* (World Scientific Pub Co, 2000).

[7] Y. Ohara, *Development of high power ion sources for fusion*. Rev. Sci. Inst. **69** (2), 908 (1998).

[8] E. Speth, *et al.*, *Rf ion sources for fusion applications: design, development and performance*. Fusion Eng. Des. **46** (2), 383 (1999).

[9] S. Peruzzo, *et al.*, *Thermal analyses for the design of the ITER-NBI arc driven ion source*. Fusion Eng. Des. **82**, 933 (2007). Proceedings of the 24th Symposium on Fusion Technology SOFT-24.

[10] Y. Okumura, *et al.*, *Development of a 500 keV, 22 A D^- ion source for the neutral beam injector for JT-60U*. Rev. Sci. Inst. **67** (3), 1018 (1996).

[11] R. Hemsworth, *et al.*, *Status of the ITER heating neutral beam system*. Nucl. Fusion **49** (4), 045006 (2009).

[12] A. Rau, *The negative ion of hydrogen*. J. Astrophys. Astr. **17** (3), 113 (1996).

[13] K. Berkner, *Advanced neutral-beam technology* (1980).

[14] C. Hopf, Private communication (2013).

[15] E. Speth, *Neutral beam heating of fusion plasmas*. Rep. Prog. Phys. **52** (1), 57 (1989).

[16] H. Vernickel, *et al.*, *ASDEX upgrade: A poloidal divertor tokamak adapted to reactor requirements*. J. Nucl. Mater. **128** (0), 71 (1984).

[17] R. Aymar, P. Barabaschi, Y. Shimomura, *The ITER design*. Plasma Phys. Control. Fusion **44** (5), 519 (2002).

[18] G. Tardini, *et al.*, *Comparison of theory based transport models with ASDEX Upgrade data*. Nucl. Fusion **42** (3), 258 (2002).

[19] A. Stäbler, J. Stober, P. Franzen, O. Gruber, F. Ryter, *Contributions to the 26th EPS Conference on Controlled Fusion and Plasma Physics* (1999), vol. 23J, pp. 1437–1440.

[20] F. Wagner, *et al.*, *On the heating mix of ITER*. Plasma Phys. Control. Fusion **52** (12), 124044 (2010).

[21] R. Trainham, *et al.*, *Negative ion sources for neutral beam injection into fusion machines*. Rev. Sci. Inst. **69** (2), 926 (1998).

[22] A. Krylov, R. Hemsworth, *Gas flow and related beam losses in the ITER neutral beam injector*. Fusion Eng. Des. **81** (19), 2239 (2006).

[23] E. Speth, *et al.*, *Overview of the RF source development programme at IPP Garching*. Nucl. Fusion **46** (6), S220 (2006).

[24] R. Nocentini, R. Gutser, B. Heinemann, M. Fröschle, R. Riedl, *Optimization of the cooling circuit and thermo-mechanical analysis for the extraction grid of ELISE*. Fusion Eng. Des. **86** (6), 916 (2011).

[25] M. Kuriyama, *et al.*, *Development of Negative-Ion Based NBI System for JT-60*. J. Nucl. Sci. Technol. **35** (11), 739 (1998).

[26] Y. Takeiri, *et al.*, *High-power and long-pulse injection with negative-ion-based neutral beam injectors in the Large Helical Device*. Nucl. Fusion **46** (6), 199 (2006).

[27] M. Kuriyama, *et al.*, *Status of the 1 MeV Accelerator Design for ITER NBI*. AIP Conf. Proc. **1390** (1), 545 (2011).

[28] H. P. L. de Esch, *et al.*, *Status of physics design of the HNB accelerator for ITER*. AIP Conf. Proc. **1515** (1), 512 (2013).

[29] M. Taniguchi, *et al.*, *Voltage holding study of 1 MeV accelerator for ITER neutral beam injector*. Rev. Sci. Inst. **83**(2), 02B121 (2012).

[30] Y. Takeiri, *Negative ion source development for fusion application*. Rev. Sci. Inst. **81**(2), 02B114 (2010).

[31] A. Kojima, *et al.*, *Achievement and improvement of the JT-60U negative ion source for JT-60 Super Advanced (invited)*. Rev. Sci. Inst. **81**(2), 02B112 (2010).

[32] A. Stäbler, *et al.*, *Development of a RF-driven ion source for the ITER NBI system*. Fusion Eng. Des. **84**, 265 (2009). Proceeding of the 25th Symposium on Fusion Technology(SOFT-25).

[33] U. Fantz, *et al.*, *Physical performance analysis and progress of the development of the negative ion RF source for the ITER NBI system*. Nucl. Fusion **49** (12), 125007 (2009).

[34] A. Masiello, *et al.*, *The European contribution to the development of the ITER NB injector*. Fusion Eng. Des. **86** (6), 860 (2011).

[35] M. Allan, S. F. Wong, *Effect of Vibrational and Rotational Exictation on Dissociative Attachment in Hydrogen*. Phys. Rev. Lett. **41**, 1791 (1978).

[36] M. Bacal, *Physics aspects of negative ion sources*. Nucl. Fusion **46** (6), S250 (2006).

[37] D. Wünderlich, *et al.*, *On the proton flux toward the plasma grid in a RF-driven negative hydrogen ion source for ITER NBI*. Plasma Phys. Control. Fusion **54** (12), 125002 (2012).

[38] M. J. J. Eerden, M. C. M. van de Sanden, D. K. Otorbaev, D. C. Schram, *Cross section for the mutual neutralization reaction* $H_2^+ + H^-$*, calculated in a multiple-crossing Landau-Zener approximation*. Phys. Rev. A **51**, 3362 (1995).

[39] R. K. Janev, Z. M. Radulović, *Ion-ion recombination and ion-pair formation processes in alkali-hydrogen diatomic systems*. Phys. Rev. A **17**, 889 (1978).

[40] R. Janev, W. Langer, K. Evans, D. Post, *Elementary Processes in Hydrogen-Helium Plasmas* (Springer-Verlag, Berlin Heidelberg, 1987).

[41] R. K. Janev, Collision processes in low-temperature hydrogen plasmas, *Berichte des Forschungszentrums Jülich JUEL-4105* (2003).

[42] D. Wünderlich, Private communication (2014).

[43] P. McNeely, D. Wünderlich, the NNBI Team, *Neutral depletion in an* H^- *source operated at high RF power and low input gas flow*. Plasma Sources Sci. Technol. **20** (4), 049801 (2011).

[44] U. Fantz, *et al.*, *Plasma diagnostic tools for optimizing negative hydrogen ion sources*. Rev. Sci. Inst. **77**(3), 03A516 (2006).

[45] W. Kraus, *et al.*, *RF Negative Ion Source Development at IPP Garching*. AIP Conf. Proc. **925** (1), 224 (2007).

[46] M. Dremel, *et al.*, *Design of cryosorption pumps for TEST BEDS of ITER relevant Neutral Beam Injectors*. Fusion Eng. Des. **74**, 205 (2005). Proceedings of the 23rd Symposium of Fusion Technology SOFT 23.

[47] W. Kraus, *et al.*, *Long pulse large area beam extraction with a rf driven* H^-/D^- *source*. Rev. Sci. Inst. **79**(2), 02C108 (2008).

[48] P. Franzen, *et al.*, *Progress of the development of the IPP RF negative ion source for the ITER neutral beam system*. Nucl. Fusion **47** (4), 264 (2007).

[49] W. Kraus, *et al.*, *The development of the radio frequency driven negative ion source for neutral beam injectors (invited)*. Rev. Sci. Inst. **83**(2), 02B104 (2012).

[50] P. Franzen, *et al.*, *The IPP RF Source: A High Power, Low Pressure Negative Ion Source For The Neutral Beam Injection System Of ITER*. AIP Conf. Proc. **993** (1), 51 (2008).

[51] S. Christ-Koch, U. Fantz, M. Berger, N. Team, *Laser photodetachment on a high power, low pressure rf-driven negative hydrogen ion source*. Plasma Sources Sci. Technol. **18** (2), 025003 (2009).

[52] L. Schiesko, P. Franzen, U. Fantz, Magnetic configuration of the beam source, *F4E-GRT-313 development of the NB mechanical components - final report*, Max-Planck-Institut für Plasmaphysik (2011).

[53] U. Fantz, C. Wimmer, the NNBI Team, *Quantification Of Cesium In Negative Hydrogen Ion Sources By Laser Absorption Spectroscopy*. AIP Conf. Proc. **1390** (1), 348 (2011).

[54] R. Gutser, *Experiments and Simulations for the Dynamics of Cesium in Negative Hydrogen Ion Sources for ITER N-NBI*, Ph.D. thesis, University of Augsburg (2010).

[55] U. Fantz, C. Wimmer, *Cesium dynamics in long pulse operation of negative hydrogen ion sources for fusion*. Rev. Sci. Inst. **83**(2), 02B110 (2012).

[56] H. B. Michaelson, *The work function of the elements and its periodicity*. J. Appl. Phys. **48** (11), 4729 (1977).

[57] W. Graham, *Proceedings of the second International Symposium on the Production and Neutralization of Negative Hydrogen Ions and Beams*, T. Sluyters, ed. (Brookhaven National Laboratory, Upton, New York, 1980), pp. 126–133.

[58] R. Gutser, C. Wimmer, U. Fantz, *Work function measurements during plasma exposition at conditions relevant in negative ion sources for the ITER neutral beam injection*. Rev. Sci. Inst. **82**(2), 023506 (2011).

[59] U. Fantz, *et al.*, *Diagnostics of the cesium amount in an RF negative ion source and the correlation with the extracted current density*. Fusion Eng. Des. **74** (1), 299 (2005). Proceedings of the 23rd Symposium of Fusion Technology SOFT 23.

[60] L. Schiesko, P. McNeely, U. Fantz, P. Franzen, N. Team, *Caesium influence on plasma parameters and source performance during conditioning of the prototype ITER neutral beam injector negative ion source*. Plasma Phys. Control. Fusion **53** (8), 085029 (2011).

[61] D. Wünderlich, R. Gutser, U. Fantz, *PIC-MC code for the transport of plasma particles and surface produced negative ions across a magnetic field*. Proceedings of the 29th International Conference on the Phenomena in Ionized gases (2009).

[62] L. Schiesko, P. McNeely, P. Franzen, U. Fantz, the NNBI Team, *Magnetic field dependence of the plasma properties in a negative hydrogen ion source for fusion*. Plasma Phys. Control. Fusion **54** (10), 105002 (2012).

[63] U. Fantz, *et al.*, *Negative ion RF sources for ITER NBI: status of the development and recent achievements*. Plasma Phys. Control. Fusion **49** (12B), B563 (2007).

[64] B. Heinemann, *et al.*, *The negative ion source test facility ELISE*. Fusion Eng. Des. **86** (6), 768 (2011). Proceedings of the 26th Symposium of Fusion Technology (SOFT-26).

[65] M. Fröschle, *et al.*, *Magnetic filter field for ELISE Concepts and design*. Fusion Eng. Des. **88** (6), 1015 (2013).

[66] R. Nocentini, R. Gutser, B. Heinemann, M. Froeschle, R. Riedl, *Plasma grid design for optimized filter field configuration for the NBI test facility ELISE*. Fusion Eng. Des. **84** (12), 2131 (2009).

[67] B. Heinemann, *et al.*, *Design of the "half-size" ITER neutral beam source for the test facility ELISE*. Fusion Eng. Des. **84** (2), 915 (2009). Proceeding of the 25th Symposium on Fusion Technology (SOFT-25).

[68] H. de Esch, R. Hemsworth, P. Massmann, *Updated physics design ITER-SINGAP accelerator*. Fusion Eng. Des. **73** (2), 329 (2005).

[69] B. Schunke, D. Bora, R. Hemsworth, A. Tanga, *Status of the Negative Ion Based Heating and Diagnostic Neutral Beams for ITER*. AIP Conf. Proc. **1097** (1), 480 (2009).

[70] R. Gutser, D. Wünderlich, U. Fantz, the NNBI-Team, *Negative hydrogen ion transport in RF-driven ion sources for ITER NBI*. Plasma Phys. Control. Fusion **51** (4), 045005 (2009).

[71] R. Nocentini, *Multidisciplinary design optimization of an ion source for fusion reactors*, Ph.D. thesis, Technical university of Munich (2011).

[72] D. Wünderlich, R. Gutser, U. Fantz, *PIC code for the plasma sheath in large caesiated RF sources for negative hydrogen ions*. Plasma Sources Sci. Technol. **18** (4), 045031 (2009).

[73] S. Mochalskyy, A. F. Lifschitz, T. Minea, *Origin of extracted negative ions by 3D PIC-MCC modeling. Surface vs Volume comparison*. AIP Conf. Proc. **1390** (1), 30 (2011).

[74] A. Hatayama, *Progress in modeling and numerical simulation of negative hydrogen ion sources (invited)*. Rev. Sci. Inst. **79**(2), 02 (2008).

[75] F. Taccogna, *et al.*, *Particle modelling of the hybrid negative ion source*. Plasma Sources Sci. Technol. **20** (2), 024009 (2011).

[76] D. Wünderlich, S. Mochalskyy, U. Fantz, P. Franzen, the NNBI-Team, *Modelling the ion source for ITER NBI: from the generation of negative hydrogen ions to their extraction*. Plasma Sources Sci. Technol. **23** (1), 015008 (2014).

[77] R. Gutser, D. Wünderlich, U. Fantz, the NNBI-Team, *Transport of negative hydrogen and deuterium ions in RF-driven ion sources*. Plasma Phys. Control. Fusion **52** (4), 045017 (2010).

[78] J. D. Lawson, *Perveance and the Bennett Pinch Relation in Partially-Neutralized Electron Beams*. J. Electron. Control. **5** (2), 146 (1958).

[79] C. D. Child, *Discharge From Hot CaO*. Phys. Rev. (Series I) **32**, 492 (1911).

[80] I. Langmuir, *The Effect of Space Charge and Residual Gases on Thermionic Currents in High Vacuum*. Phys. Rev. **2**, 450 (1913).

[81] A. P. Banford, *The Transport of Charged Particle Beams* (E. & F. N. SPON LIMITED, London, 1966).

[82] P. Dahl, *Introduction to Electron and Ion Optics* (ACADEMIC PRESS INC. LTD., London, 1973).

[83] H. Wollnik, *Optics of Charged Particles* (ACADEMIC PRESS INC. LTD., New York and London, 1987).

[84] E. Harting, F. H. Read, *Electrostatic Lenses* (ELSEVIER SCIENTIFIC PUBLISHING COMPANY, Amsterdam - Oxford - New York, 1976).

[85] P. Franzen, *et al.*, *Performance of multi-aperture grid extraction systems for an ITER-relevant RF-driven negative hydrogen ion source*. Nucl. Fusion **51** (7), 073035 (2011).

[86] V. Antoni, *et al.*, *Physics design of the injector source for ITER neutral beam injector (invited)*. Rev. Sci. Inst. **85**(2), 02B128 (2014).

[87] J. Geddes, J. Hill, H. B. Gilbody, *Formation of excited hydrogen atoms in electron detachment collisions by* 3–25 *keV* H^- *ions*. J. Phys. B: At. Mol. Phys. **14** (24), 4837 (1981).

[88] C. F. Barnett, *Atomic Data for Fusion*, vol. 1 (Controlled Fusion Atomic Data Center, 1990).

[89] T. Tabata, T. Shirai, *ANALYTIC CROSS SECTIONS FOR COLLISIONS OF* H^+, H_2^+, H_3^+, *H*, H_2, *AND* H^- *WITH HYDROGEN MOLECULES*. At. Data Nucl. Data Tables **76** (1), 1 (2000).

[90] L. Schiesko, *et al.*, *A study on backstreaming positive ions on a high power negative ion source for fusion*. Nucl. Fusion **51** (11), 113021 (2011).

[91] G. Fubiani, H. P. L. de Esch, A. Simonin, R. S. Hemsworth, *Modeling of secondary emission processes in the negative ion based electrostatic accelerator of the International Thermonuclear Experimental Reactor*. Phys. Rev. ST Accel. Beams **11**, 014202 (2008).

[92] A. Lorenz, U. Fantz, P. Franzen, Ortsaufgelöste H_α-Dopplerspektroskopie an einem Wasserstoffstrahl aus einer negativen Ionenquelle, *IPP Report 4/285*, Max-Planck-Institut für Plasmaphysik (2005).

[93] P. Franzen, B.Ruf, Beam modeling, *F4E-GRT-313 development of the NB mechanical components - final report*, Max-Planck-Institut für Plasmaphysik (2011).

[94] I. Soloshenko, *XVIIIth International Symposium on Discharges and Electrical Insulation in Vacuum* (1998), vol. 2, pp. 675–678.

[95] A. J. T. Holmes, *The Physics and Technology of Ion Sources* (John Wiley & Sons, 1989), chap. Beam Transport, pp. 53–106.

[96] R. Nocentini, *et al.*, *Beam diagnostic tools for the negative hydrogen ion source test facility ELISE*. Fusion Eng. Des. **88** (6-8), 913 (2013).

[97] B. Zaniol, R. Pasqualotto, M. Barbisan, *Design of a beam emission spectroscopy diagnostic for negative ions radio frequency source SPIDER*. Rev. Sci. Inst. **83**(4), 043117 (2012).

[98] R. Pasqualotto, *et al.*, *Diagnostics of the ITER neutral beam test facility*. Rev. Sci. Inst. **83**(2), 02B103 (2012).

[99] C. F. Burrell, W. S. Cooper, R. R. Smith, W. F. Steele, *Doppler shift spectroscopy of powerful neutral beams*. Rev. Sci. Inst. **51** (11), 1451 (1980).

[100] J. Bonnal, *et al.*, *Optical diagnostics on high-power neutral beams*. Phys. Lett. A **69** (2), 116 (1978).

[101] W. Ott, F.-P. Penningsfeld, Spectroscopic determination of species and divergence of hydrogen beams in the W7AS neutral beam injectors, *IPP Report 4/258*, Max-Planck-Institut für Plasmaphysik (1993).

[102] D. Wünderlich, *Berechnung von Teilchendichten für die Diagnostik an Niedertemperaturplasmen*, Ph.D. thesis, University of Augsburg (2004).

[103] P. Franzen, U. Fantz, T. N. Team, *Beam Homogeneity Dependence on the Magnetic Filter Field at the IPP Test Facility MANITU*. AIP Conf. Proc. **1390** (1), 310 (2011).

[104] J. Pamela, *A model for negative ion extraction and comparison of negative ion optics calculations to experimental results*. Rev. Sci. Inst. **62** (5), 1163 (1991).

[105] R. Becker, *NIGUN: A two-dimensional simulation program for the extraction of* H^- *ions*. Rev. Sci. Inst. **75** (5), 1723 (2004).

[106] P. Spädtke, C. Mühle, *Simulation of ion extraction and beam transport*. Rev. Sci. Inst. **71** (2), 820 (2000).

[107] M. Cavenago, P. Veltri, F. Sattin, G. Serianni, V. Antoni, *Negative Ion Extraction With Finite Element Solvers and Ray Maps*. IEEE Trans. Plasma Sci. **36** (4), 1581 (2008).

[108] P. Veltri, *Physics of negative extraction and acceleration in neutral beam injectors*, Ph.D. thesis, Universita degli studi di Padova (2010).

[109] M. Cavenago, *et al.*, *Development of Small Multiaperture Negative Ion Beam Sources and Related Simulation Tools*. AIP Conf. Proc. **1097** (1), 149 (2009).

[110] B. Zaniol, *Error evaluation in the spectroscopic measurement of high power beam angular divergence*. J. Quant. Spectrosc. Radiat. Transfer **112** (3), 513 (2011).

[111] S. Mochalskyy, A. Lifschitz, T. Minea, *3D modelling of negative ion extraction from a negative ion source*. Nucl. Fusion **50** (10), 105011 (2010).

[112] C. Birdsall, *Particle-in-cell charged-particle simulations, plus Monte Carlo collisions with neutral atoms, PIC-MCC*. IEEE Trans. Plasma Sci. **19** (2), 65 (1991).

[113] S. Mochalskyy, *Modeling of the negative ion extraction from a hydrogen plasma soure. Application to ITER Neutral Beam Injector*, Ph.D. thesis, University Paris-Sud (2011).

[114] W. B. Gragg, *Repeated extrapolation to the limit in the numerical solution of ordinary differential equations*, Ph.D. thesis, University of California, Los Angeles (1964).

[115] J. P. Boyd, *Chebyshev and Fourier Spectral Methods* (Dover Publishers, 2001).

[116] D. Ciric, PerMag, developped by D. Ciric, JET Joint Undertaking, Abingdon.

[117] ANSYS Ltd., *ANSYS Manual* (2009).

[118] H. de Esch, *et al.*, *Results of the SINGAP neutral beam accelerator experiment at JAEA*. Fusion Eng. Des. **84** (2), 669 (2009). Proceeding of the 25th Symposium on Fusion Technology (SOFT-25).

[119] E. Sartori, P. Veltri, *AVOCADO: A numerical code to calculate gas pressure distribution*. Vacuum **90** (0), 80 (2013).

[120] P. Franzen, Private communication (2013).

[121] M. Wutz, H. Adam, W. Walcher, K. Jousten, *Handbuch Vakuumtechnik: Theorie und Praxis*, vol. 7 (Vieweg Verlagsgesellschaft, 2000).

List of Figures

List of Tables

Acknowledgements

Finally I would like to thank all the people who helped me to finish my PhD thesis. Without their encouragement and advisory I would not have succeeded this work. I want to thank:

- First of all **Prof. Dr.–Ing Ursel Fantz** for giving me the opportunity to work on a very interesting and challenging topic. She guided me through my whole dissertation and always gave me the best support on my scientific advancement and education.
- My examination committee, especially **Prof. Dr. Wolfgang Brütting**.
- **Dr. Peter Franzen** and **Dr. Dirk Wünderlich** for their everyday support, the fruitful discussions and their great helpfulness.
- **Dr. Loïc Schiesko**, **Dr. Christian Hopf**, **Dr. Riccardo Nocentini** and **Dipl. Phys. Christian Wimmer** for their help on every upcoming question relating the work on the negative ion sources at IPP Garching.
- **Dipl.–Ing. Bernd Heinemann**, **Dipl.–Ing. Rudolf Riedl**, **Dipl.–Ing. Markus Fröschle** and **Mr. Moritz Gruber** for their help concerning all the engineering tasks.
- **Mr. Rudolf Pulker**, **Mr. Peter Klein**, **Mr. Frank Fackert**, **Mr. Alexander Oswald**, **Mr. Josef Deimel**, **Mr. Martin Kammerloher** and **Mr. Jürgen Steinberger** for their help on every assembling issue.
- **M. Sc. Hans-Philipp Otto**, **B. A. Malte Tingelhoff** and **Mr. Johannes Rehm** for their great support.

Of course I also want to thank my parents **Dipl.–Betrw. Bernhard Ruf** and **Mrs. Ulrike Ruf** for their encouragement, advises and help. I also want to thank the whole **NNBI-Team** of IPP Garching and the **EPP-Team** from the university of Augsburg. All the people from these two teams are great persons and it was a honor and pleasure to be a part of these groups.

Curriculum Vitae

Name: Benjamin Ruf
Geboren : 06.04.1984 in Augsburg, Bayern
Familienstand: ledig

09/1990 - 07/1992	Grundschule Schondorf am Ammersee
09/1992 - 07/1994	Grundschule Westheim
09/1994 - 06/2004	Gymnasium Neusäß Erwerb der allgemeinen Hochschulreife
01/2005 - 09/2005	Grundwehrdienst in der Reinhardt-Kaserne Ellwangen und der Karwendel-Kaserne Mittenwald
10/2005 - 12/2010	Studium der Physik an der Universität Augsburg Erwerb des Diploms in Physik
02/2011 - 01/2014	Doktorand am Max-Planck-Institut für Plasmaphysik, Garching